3-Dimensional Modeling and Simulation of Surface and Sidewall Roughening During Plasma Etching

by

Hiroyo Kawai

B.S. Chemical Engineering
University of Minnesota Twin Cities, 2001

M.S. Chemical Engineering Practice
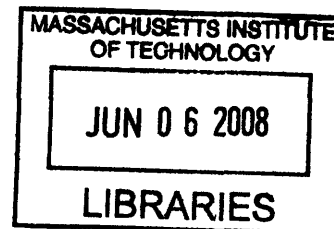Massachusetts Institute of Technology, 2005

Submitted to the Department of Chemical Engineering
in Partial Fulfillment of the Requirements for the Degree of

Doctor of Philosophy in Chemical Engineering

at the
Massachusetts Institute of Technology
May 2008
[June 2008]

Signature of
Author..............................
Department of Chemical Engineering
May 22, 2008

Certified
By...................................:
Herbert H. Sawin
Professor of Chemical Engineering and
Electrical Engineering and Computer Science
Thesis Advisor

Accepted
By......................................
William Deen
Professor of Chemical Engineering
Chairman, Committee for Graduate Students

3-Dimensional Modeling and Simulation of Surface and Sidewall Roughening During Plasma Etching

by

Hiroyo Kawai

Submitted to the Department of Chemical Engineering on May 22, 2008
in partial fulfillment of the requirements for the degree of
Doctor of Philosophy in Chemical Engineering

Abstract

Line edge roughness (LER) on the sidewalls of gate electrodes in metal oxide semiconductor transistors is one of the most important issues in the manufacturing of modern integrated circuits (IC). The significance of LER increases tremendously as desired features miniaturize because the dimensions of the edge roughness become comparable to those of the features. A fundamental understanding of the origins of the surface roughness and LER formation during plasma etching process is thus necessary to optimize the IC manufacturing process and prevent device failure. To meet this challenge, a 3-D Monte Carlo simulator was developed to model the roughening of a surface as well as follow the macroscopic evolution of its profile during plasma etching. The simulator employs a cellular representation of the surface with Monte Carlo modeling of the mass transport and reaction kinetics. The local geometric properties of surface features were computed by fitting to a polynomial surface, which allowed for a more accurate description of the surface normal and local curvature. This numerical algorithm for simulating etching and deposition was validated by comparing with the theoretical advancement of a surface for the case of isotropic and anisotropic etching.

The simulator was used to explore surface roughening during the physical sputtering of a blanket silicon surface by argon ion bombardment. The results showed that there is a significant change in its morphology with different off-normal angles of incidence. When the surface is etched at normal incidence, the surface becomes roughened with no preferred orientation. When etched with an off-normal ion incidence below 50°, the surface develops ripples that are oriented perpendicular to the ion beam direction. For off-normal angles between 50° and 60°, the surface remains smooth independent of the etch time. The surface is again roughened for angles of incidence above 60°, forming patterns that are aligned with the ion beam direction. These trends match qualitatively with those observed in experimental measurements. The simulation results further showed that these transitions of surface morphology with increasing off-normal angles of ion incidence are related to the angular dependence of the etching yield. The effects of other factors, including the angular distribution of scattered ions, the non-uniformity of the film density, the initial roughness of the surface and the re-deposition of sputtered materials were also investigated using our simulator.

The roughening of the sidewalls of patterned polysilicon etched with Cl_2 was also explored via simulation. The simulation results showed that the primary cause of

sidewall roughness is due to the transfer of roughness on the photoresist and anti-reflective coating (ARC) sidewall to the underlying polysilicon sidewall during etching. The root-mean-square (RMS) roughness of the sidewalls due to the features that result from the etching is highest at the photoresist layer and decreases with depth. This trend is consistent with experimental observations. The simulation also showed that the re-deposition of sputtered photoresist particles onto the sidewalls during etching enhances sidewall roughening.

Thesis Supervisor: Herbert H. Sawin
Professor of Chemical Engineering and Electrical Engineering & Computer Science

Acknowledgements

Table of Contents

Table of Figures

9

12

13

14

17

1. Introduction

1.1. Integrated circuit manufacturing

Since its inception in the 1960's, integrated circuits (IC) have since become ubiquitous in modern day society. Computers, cellular phones and other digital appliances all rely on IC, and most industrialized nations today believe that IC will in the near future be one of the strongest pillars of their economy. IC chips consist of a large number of components such as metal-oxide-semiconductor (MOS) transistors, resistors and capacitors, and they are wired together to perform a particular circuit function. Technological improvements over the past few decades have allowed for the size of these circuits to become much smaller, increasing the density of transistors integrated on each chip in order to achieve higher performance and more complex functionality while trying to maintain low power dissipation and manufacturing costs. The number of transistors on a chip has been doubling approximately every two years, and this phenomenon is well-known as Moore's Law[1]. The component size is often characterized by the smallest lateral feature size that is printed on a wafer surface during its fabrication. At the time this thesis is being written, 65 nm processors are already being manufactured, and 45 nm and 32 nm processors are currently under development. However, as the sizes of transistors in IC shrink, many steps in its manufacturing process become challenging. Of paramount importance is the necessity for good control over the feature profiles on the fabricated wafer while minimizing the surface roughness in order to maintain good device performance and process yields.
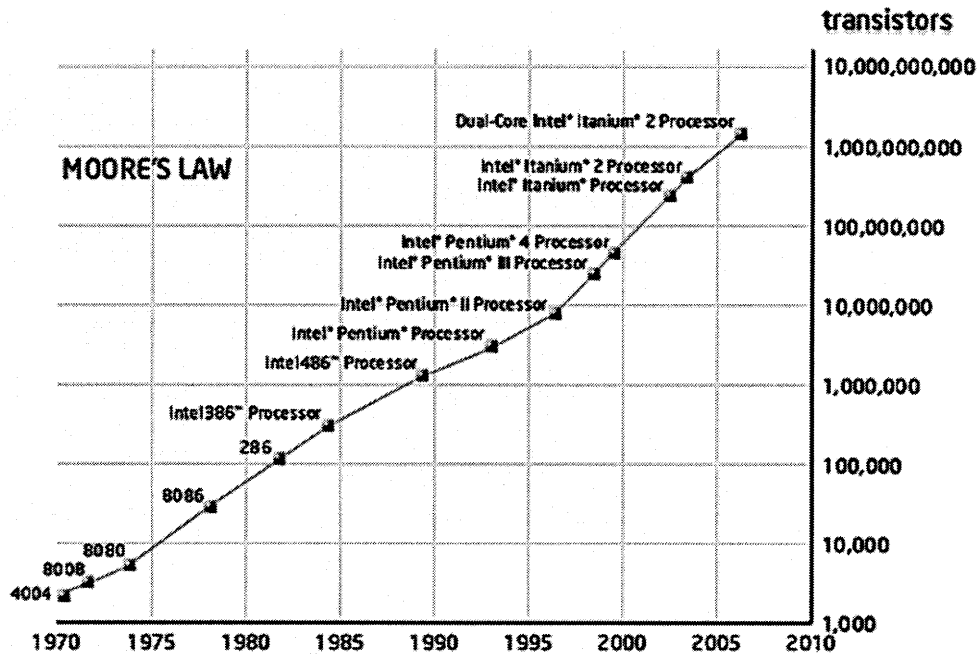
Figure 1.1: Moore's Law shows the exponential increase in the number of transistors placed on an integrated circuit (Ref. 1).

1.2. Microelectronics processing

The fabrication of integrated circuits involves many consecutive processes. Figure 1.2 gives a simple illustration of each step in a microfabrication process. The film to be patterned is deposited onto a silicon substrate (Figure 1.2a), and is coated with a light-sensitive material called a photoresist (Figure 1.2b). The photoresist is then exposed to light through a patterned photomask (Figure 1.2c), which makes the exposed part chemically less stable in the case of a positive photoresist and more resistant in the case of a negative photoresist. Figure 1.2 illustrates the process for a positive photoresist. The exposed part of the resist is removed by a developer, leaving the unexposed part of the photoresist with the desired pattern transferred from the photomask. This process of patterning a photoresist is called lithography. After patterning, the photoresist acts as a

21

protective mask, and areas of the underlying film that are not covered by the photoresist are etched away (Figure 1.2e). The most common etching technique used is plasma etching, where a feature is etched anisotropically, allowing the transfer of very small features defined in the lithography step. After etching, the photoresist is stripped, leaving the patterned film (Figure 1.2f). These steps are repeated many times to produce a final device with multiple layers bearing different patterns. This thesis focuses on one of the key components of this fabrication process, namely the etching step (Figure 1.2e). In the following section, plasma etching process will be discussed in greater detail.
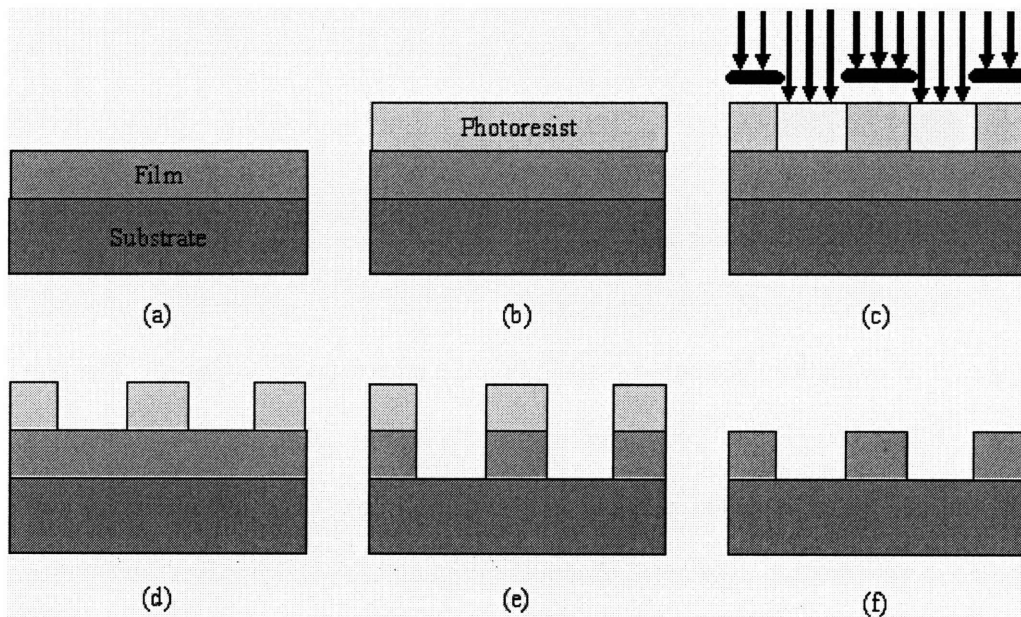
Figure 1.2: Subtractive processing in integrated circuit manufacturing. (a) Film to be patterned is deposited on the substrate. (b) Photoresist is spin-coated over the film. (c) The photoresist is exposed to radiation through the patterned mask. (d) The exposed part of the resist is removed (for positive photoresist). (e) The unprotected part of the underlying film is etched. (f) Photoresist is removed.

1.3. Plasma etching

Plasma is a low pressure, partially ionized gas consisting of neutral gases, excited neutral species, ions and free electrons. The ions and excited neutral species are produced by the collision of electrons (accelerated by the electric current applied to the plasma) with neutral gas molecules. Since electrons have relatively low mass and thus move faster than ions, a surface that is exposed to plasma quickly builds up a negative charge and develops a negative potential with respect to the plasma. The resulting electric field attracts and accelerates the ions and repels the electrons to maintain a net zero flux of charges to the surface. Ions strike the surface with high energy and directionality to allow for anisotropic etching. Figure 1.3 shows an example of etching a polysilicon film in Cl_2 plasma.
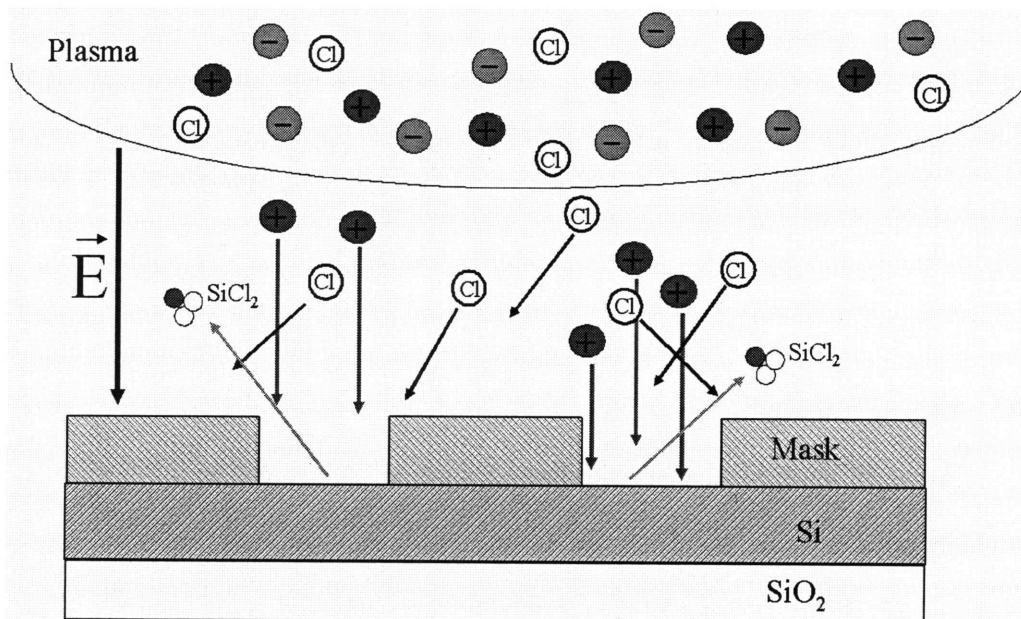
Figure 1.3: Plasma etching of polysilicon film in chlorine-based chemistry. Positive chlorine ions strike the surface with high energy and high directionality. The reactive neutrals (Cl, Cl_2) are transported with no preferred directionality. After the reaction occurs on the surface, product is removed, and the etching continues.

Both reactive neutral species and energetic ions act as etchants in the process, working together in a synergistic manner[2]. This process is known as ion-enhanced etching. If the surface is etched by a chemical reaction involving the reactive neutral species alone ("chemical etching"), the etching occurs isotropically due to the isotropic angular distribution and low sticking probability of the neutral species. Selectivity is relatively high in chemical etching. If the neutral species is absent and the surface is etched physically, or sputtered by energetic ions, the surface is etched anisotropically due to the directionality of ions impinging on the surface. Sputtering occurs by accelerated ions striking the atoms on the surface and physically dislodging them. The selectivity is relatively low for sputtering. In ion-enhanced etching, both the chemical and physical components are active, but the profiles are anisotropic as in physical etching, with a higher etch rate and better selectivity. One of the common explanations for this cooperative etching mechanism is that the ion bombardment causes some damage to the surface, which enhances the etching reaction at the damaged areas[3].

1.4. Etching Artifacts

Although ion-enhanced etching allows for the anisotropic etching of polysilicon with high specificity over the photoresist and the silicon dioxide layers, a perfect pattern transfer is very difficult. Some of the common artifacts observed in the etching process are shown in Figure 1.4. Sidewall bowing, or the curving of the sidewalls, is caused by factors such as sidewall deposition and angular dependence of the etching yield[4]. Microtrenching refers to the enhanced etching that occurs at the bottom of the etched

sidewall, and it is caused by ions reflecting from curved sidewalls, resulting in a high ion flux at the foot of the sidewall[5,6]. The formation of microtrenching also depends on the type of plasma chemistry involved. For example, while microtrenching is absent in HBr-based plasma, it is always observed in chlorine-based plasma etching[7]. Facets are formed due to the sputtering of the corners of the mask during the etching process, and these facets may affect the further etching of the surface by altering the trajectory of the ions scattered from the facet. Undercutting, or lateral etching into a layer, occurs at the interface of two materials where one material is resistant towards etching, and it is often caused by isotropic spontaneous etching or by ions scattering off a neighboring mask[8,9].
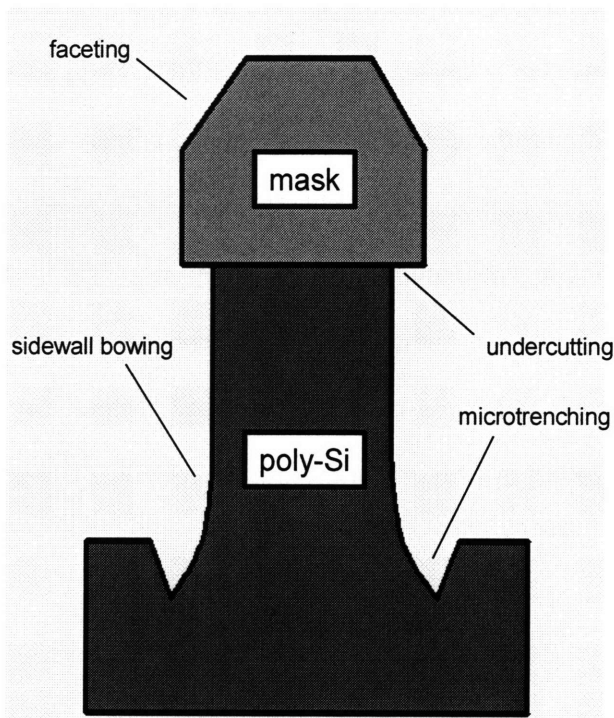
Figure 1.4: Common artifacts in plasma etching process. Common artifacts include sidewall bowing, microtrenching, faceting and undercutting.

1.5. Line-edge roughness (LER)

In addition to the etching artifacts mentioned in the previous section, the post-etch roughness on a sidewall also contributes to the imperfection of feature profiles. A sample atomic force microscopy (AFM) image of a roughened sidewall is shown in Figure 1.5. In between the development of the photoresist and the plasma treatment, the sidewall roughness on the photoresist is isotropic (Figure 1.5a), but the sidewall is slightly striated along the direction of ion beam and becomes anisotropic during the etching of the anti-reflective coating (ARC) layer (Figure 1.5b). The striations are further propagated down the sidewall after the subsequent etching of the SiO_2 layer. This roughening of the sidewall is often referred to as line-edge roughness (LER). There are many factors that contribute to LER during the etching process, but the primary cause of LER is the templating effect, in which striations formed in the mask prior to substrate etching act as templates that transfer roughness to lower layers as they are etched[10]. However, as it can be seen in Figure 1.5, the roughness of the mask continues to increase with etching. Therefore, the sidewall roughness of the final etched feature may result from the roughening of the sidewall in each step of the process, including lithography and etching processes.
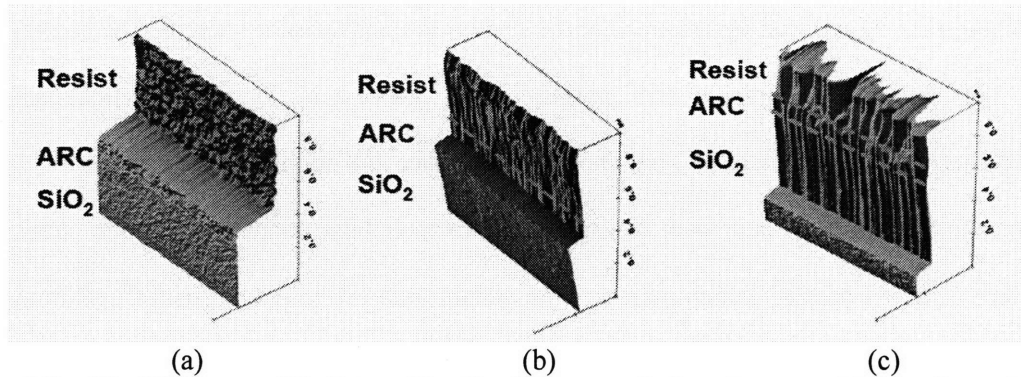
Figure 1.5: The AFM images of the feature sidewall at different step in the etch process. (a) After photoresist development, before plasma etching, (b) after N2-H2 organic ARC open, (c) after 90 seconds of oxide etching in fluorocarbon plasmas. (Ref. 10)

The sidewall roughness of the photoresist that develops during the lithographic process is often called top-LER, and numerous researchers have explored the sources of post-development top-LER. Some of the common sources of post-development roughness on photoresist include low aerial image contrast[11] or mask imperfection[12,13] during exposure, insufficient developing time[12], and a wide polymer molecular weight distribution in the photoresist[14,15].

The effects of post-development roughness on subsequent etching steps were also studied extensively. Yahata et al[14] found that the sidewall of the photoresist with a wider molecular weight distribution roughened significantly more than one with a narrow distribution after developing and subsequently showed that the sample etched using a roughened photoresist mask resulted in a rougher sidewall. Rasgon et al. found that the sidewall roughness of an etched feature can be minimized by maintaining a smooth sidewall during ARC opening through modification of the etch chemistry[10,16]. While it is obviously important to minimize the roughness of the photoresist mask before etching subsequent layers, it is also crucial to minimize further roughening of the photoresist in subsequent etching steps. It was found that the deformation of the photoresist during

27

etching may be reduced by pre-treating the photoresist with plasma such as HBr and H_2 in between the lithographic and plasma etching processes[17,18]. This pretreatment becomes more important as 193 nm photoresists replace 248 nm photoresists because 193 nm photoresists have poor etch resistance due to their high content of oxygen atoms (from carbonyl groups) which increases the etching rate of the photoresist[19,20]. Kim et al[21] investigated the roughening of the photoresist during dry etching of silicon nitride with $CF_4/CHF_3/O_2/Ar$ chemistries. They found that the two major morphology changes in the surface of the photoresist during etching are striation and wiggling. Striation results from the variation in erosion rate at the top part of the photoresist caused by ion bombardment and fluorocarbon polymer deposition. Wiggling or zigzagged collapse of the photoresist results from the slimming of the photoresist and deposition of the fluorocarbon polymer during etching, and it is enhanced by thermal heat. They found that the most critical parameters to minimize the deformation of the photoresist, and thus the sidewall roughening, are chamber pressure and ion energy.

In addition to patterned samples, the roughening of blank substrates such as Si, SiO_2 and various dielectric materials have also been studied[16,22-25]. More specifically, the etching kinetics and surface roughening profiles were characterized under varying conditions of plasma chemistry, ion energy, and ion angle of incidence. Yin et al[22-24] examined the angular dependence of etching yields of polysilicon and dielectric materials in Cl_2/Ar and fluorocarbon plasmas with various ion energies and plasma source pressures. They found that at low plasma source pressure (low neutral-to-ion ratio), the angular dependence of etching yields was more sputter-like, and the etching yield peaks at 60°~70° off-normal angle of ion incidence. By contrast, at high plasma source pressure

(high neutral-to-ion ratio) the angular dependence of etching yields resembled that of ion-enhanced etching, where the etching yield drops with increasing off-normal angles. They explained the roughness of the surface etched at different off-normal angles of incidence using an angular dependence yield curve. In addition to the roughening caused by ion bombardment, the effects of fluorocarbon polymer deposition on roughening were also discussed in their study.

It is apparent from the plethora of studies conducted on the plasma etching of different surfaces that the entire process is an extremely complex one, with parameters too numerous to fully explore systematically by experimentation. This has, as a result, prompted the development of simulators that can profile the etching of surfaces under various physical and chemical conditions.

1.6. Modeling and simulation of etching processes

The development of feature scale simulators is important in order to understand the contributions of each of the processing parameters in the etching process because it is difficult to distinguish between them in purely empirical studies. Furthermore, the ability to predict feature profile evolution and surface roughness for various process conditions can greatly reduce the time and cost of process development and optimization. Some of the previous simulation efforts on surface evolution in etching, deposition and lithography processes will be discussed later in greater detail. There are generally 4 broad categories of algorithms, though some simulators fall into more than one category because a combination of multiple algorithms is implemented into a single simulation.

1.6.1. String methods

In these methods, the surface is represented by a string of points or nodes connected by straight line segments. Each point moves with a fixed etching or deposition rate along the surface normal, which is approximated by the bisector of the angle defined by a vertex and its two adjacent vertices. The positions of the nodes are updated and the points are then reconnected. The advantages of this method are that the surface propagation is straightforward, and the representation of the interface can be very accurate for the case where the surface topology does not change drastically. However, the profiles may be unstable or inaccurate if the time integration step is large or when sharp discontinuities are present in the surface because of the possible formation of surface loops, in which the surface intersects with itself. Thus, an additional algorithm is required to remove these loops. Another disadvantage is that it is difficult to include all the physics and chemistry involved in the etching process, and the composition-dependent properties of the surface cannot be incorporated. In addition, the extension of this method to three dimensions is difficult because in-line segments are changed into triangles or polygons that are even more difficult to keep track of. Nonetheless, this method has been used extensively in 2-D simulations of etching and deposition processes[26,27]. Tuda et al[26] employed a 2-D string method to simulate the effects of ion temperature and energy on the etch anisotropy for different neutral-to-ion flux ratios in the etching of Si in Cl_2 plasma. Zier et al[27] developed a 2-D simulator using the string method to model the development of facets and ripples on ion bombarded surfaces. Hamaguchi dt al[28] improved on the string method by incorporating the entropy condition for a given etch rate to accurately calculate slope discontinuities. Scheckler et al[29]

extended the 2-D string based model to 3-D, where the motion of facets was successfully tracked, but it required an additional algorithm for eliminating surface loops.

1.6.2. Method of Characteristics

In this method, the evolution of the interface is defined by a system of ordinary differential equations that are solved numerically to obtain the final feature. Singh et al[30] used this method to explore the effects of re-emission of chemical reactants from the surface and their diffusion along the surface in the etching of Si with SF_6. Shaqfeh et al[31] showed the effects of line proximity and aspect ratios on etched profiles. Katardjiev et al[32] extended this method to 3-D and demonstrated topographical simulations of chemical vapor deposition and reactive ion etching. Shaqfeh et al[31] compared the method of characteristics with the string method and showed that the former is more accurate and efficient. As an example, the string method often causes errors when the surface slope varies drastically, but the method of characteristics avoids this problem since the trajectories are not limited to the direction of the surface normal. Based on this method, however, it is still difficult to incorporate surface composition dependent properties and accurate physical and chemical mechanisms to the simulation.

1.6.3. Level set methods

Level set methods are a robust and accurate technique for tracking complicated motions at the interface, which approximates the equations of motion using hyperbolic conservation laws[33]. In this method, sharp gradients and cusps can be tracked easily, and the effects of curvature can also be incorporated. Makabe et al[34] simulated feature

profiles of SiO_2 trenches and explored the effects of feature-formation under charged and neutral deposition in 2-D. Hsiau et al[35] incorporated the level-set method into Stanford's SPEEDIE code in order to simulate etching and deposition. They demonstrated the high efficiency and stability of the level set method and easy extension of the simulation to 3-D. However, the surface composition dependence cannot be considered while the surfaces advance, and it is difficult to include all the physics and chemistry involved in the etching processes. Therefore, its use is limited to the topographical simulation of surface evolution that involves little or no compositional dependences.

1.6.4. Cell-based methods

In these methods, the computational domain is divided into a set of cells which contain volume fractions of different materials. The cell boundaries are used to reconstruct the surface. The advantages of this technique are that they can easily handle topological changes and can be extended to 3D. In addition, the cell-based method can track the composition of the surface, which is an important factor in the characterization and understanding of surface processes.

The cell-based method has widely been used due to its robustness, as exemplified by the work of Hwang et al[36], who developed a two-dimensional cell-based profile simulator to explore surface evolution during the over-etching of polysilicon-on-insulator structures. Micro-trenching, which is commonly observed in the chlorine etching of silicon, was simulated successfully using the cell-based method in 2-D[37,38]. The cell-based method has also been employed in the simulation of photolithography processes in 3-D[39].

32

The disadvantages of the cell-based method include difficulties in determining geometric properties such as surface normals and curvature, and in practice also require more memory and CPU resources than the other methods mentioned. The large amounts of memory and computational power required are not considered as major problems due to recent advances in computer architecture, but a good method of calculating the geometric properties still remains as a major challenge. Mahorowala et al[37] fitted a line to neighboring cells on a 2-D surface using a linear least squares method in order to compute the surface normals, but this method limits the curvature that can be captured. Zhou et al[40] developed a string-cell hybrid method to simulate the Bosch process in which the surface advancement was kept track of with the string method and the materials of the surface were kept track of with a mesh of cells. Similarly, Fujinaga et al[41] combined the concepts of the cell-based and string-based algorithms to develop a 3-D topography simulator. They defined the surface as the region where the normalized number density of particles is between 0 and 1, and the equi-volume rate point (EVRP), where the density is 0.5, were defined for each surface cell. The surface was represented by polygons formed by connecting these EVRPs. They showed the accuracy of the algorithm by simulating isotropic etching, deposition as well as anisotropic etching processes. However, although the overall macroscopic structures were captured well by the simulation, capturing the microscopic roughness of the surface has so far been elusive.

We employed the cell-based technique to model the surface advancement in our own profile simulator because of the ease of incorporating the compositional dependence. Combining this technique with the local polynomial fitting of surface features for the

calculation of their geometric properties allowed for the modeling of surface roughness evolution, which was the primary objective and basis for the work presented in this thesis.

1.7. Thesis objective

The primary objective of our simulation efforts was to develop a generalized 3-D profile simulator that could effectively capture the microscopic surface roughening as well as the macroscopic surface profile evolution, and to gain a fundamental understanding of the surface roughening mechanisms through simulation. To this end, our developed simulator is robust and has the ability to incorporate realistic surface kinetics that can model both etching and deposition. This work focused on surface and sidewall roughening during the plasma etching of polysilicon, which is significant because although there exist many 2-D and 3-D simulators that can model the profile evolution of different processes, there is currently no simulator to the best of our knowledge that explores the roughening mechanisms in etching processes in detail.

In Chapter 1, the development of the 3-D profile simulator that employs cellular representation for the surface along with the Monte Carlo modeling of mass transport and kinetics will be described. The local geometric properties of surface features were calculated by fitting to a polynomial surface, which allowed for a more accurate description of the surface normal and local curvature. This novel approach for 3-D simulation was justified by comparing to the theoretical advancement of the surface in the case of isotropic and anisotropic etching.

The simulator was then used to explore the roughening of the surface during the physical sputtering of a blanket silicon surface by argon ion bombardment. Although this may seem irrelevant to studying the sidewall roughness of patterned films in plasma etch systems, it is important to first understand and establish the roughening mechanisms for a simple physical sputtering process, which is attributed only to ion bombardment and does not involve other complicated factors such as surface chemical reactions. In Chapter 2, the effects of various etching parameters such as the ion angle of incidence, the angular dependence of the etching yield, and the angular distribution of scattered ions on surface roughening were studied. The results were compared with surface roughening trends that are experimentally observed in physical sputtering processes described in the literature.

Finally, the simulator was used to model the sidewall roughness during the etching of patterned polysilicon films. The effects of photoresist mask roughness and the propagation of roughness along the sidewalls during the etching process were investigated and qualitatively compared with experimentally observed trends.

1.8. References

1. G. E. Moore, Electronics 38, (1965).
2. W. Coburn and H. F. Winters, Journal of Applied Physics **50**, 3189 (1979).
3. J. D. Plummer, M. Deal, and P. B. Griffin, *Silicon VLSI Technology*, Prentice Hall, 2000.
4. S. A. Vitale, H. Chae, and H. H. Sawin, Journal of Vacuum Science and Technology A **19**, 2197 (2001).
5. J. C. Arnold and H. H. Sawin, Journal of Applied Physics **70**, 5314 (1991).
6. A. P. Mahorowala and H. H. Sawin, Journal of Vacuum Science and Technology B **20**, 1084 (2002).
7. A. P. Mahorowala and H. H. Sawin, Journal of Vacuum Science and Technology B **20**, 1055 (2002).

8. W. Jin and H. H. Sawin, Journal of Vacuum Science and Technology A **21**, 911 (2003).
9. M. Oda and K. Hirata, Japanese Journal of Applied Physics **19**, L405 (1980).
10. D. L. Goldfarb *et al.*, Journal of Vacuum Science and Technology B **22**, 647 (2004).
11. M. I. Sanchez *et al.*, Proc. SPIE **3678**, 160 (1999).
12. G. W. Reynolds and U. W. Taylor, Journal of Vacuum Science and Technology B **17**, 334 (1999).
13. G. W. Reynolds, J. W. Taylor, and C. J. Brooks, Journal of Vacuum Science and Technology B **17**, 3420, (1999).
14. A. Yahata, S. Urano, and T. Inoue, Japanese Journal of Applied Physics **36**, 6722 (1997).
15. T. Yamaguchi, K. Yamazaki, and H. Namatsu, Journal of Vacuum Science and Technology B **22**, 2604 (2004).
16. S. A. Rasgon, Ph. D. Thesis, Massachusetts Institute of Technology, 2005.
17. A. P. Mahorowala *et al.*, Proc. SPIE **5753**, 380 (2005).
18. M. –C. Kim *et al.*, Journal of Vacuum Science and Technology B **24**, 2645 (2006).
19. H. Gokan, S. Esho, and Y. Ohnishi, Journal of the Electrochemical Society **130**, 143 (1983).
20. M. S. Kim *et al.*, Proc. SPIE **4345**, 737 (2001).
21. J. Kim *et al.*, Journal of Vacuum Science and Technology B **21**, 790 (2003).
22. A. M. Barklund and H. O. Blom, Journal of Vacuum Science and Technology A **11**, 1226 (1993).
23. Y. Yin and H. H. Sawin, Journal of Vacuum Science and Technology A **26**, 161 (2008).
24. Y. Yin and H. H. Sawin, Journal of Vacuum Science and Technology A **25**, 802 (2007).
25. Y. Yin, Ph.D. Thesis, Massachusetts Institute of Technology, 2007.
26. M. Tuda, K. Nishikawa, and K. Ono, Journal of Applied Physics **81**, 960 (1997).
27. M. Zier and W. Hauffe, Nuclear Instruments and Methods in Physics Research B **202**, 182 (2003).
28. S. Hamaguchi, M. Dalvie, R. T. Farouki, and S. Sethuraman, Journal of Applied Physics **74**, 5172 (1993).
29. E. W. Scheckler and A. R. Neureuther, IEEE Transactions on Computer-Aided Design of Integrated Circuit Systems **13**, 219 (1994).
30. V. K. Singh, E. S. G. Sheqfeh, and J. P. McVittie, Journal of Vacuum Science and Technology B **10**, 1091 (1992).
31. E. S. G. Shaqfeh and C. W. Jurgensen, Journal of Applied Physics **66**, 4664 (1989).
32. I. V. Katardjiev, G. Carter, M. J. Nobes, S. Berg, and H. –O. Blom, Journal of Vacuum Science and Technology A **12**, 61 (1994).
33. J. A. Sethian, Journal of Computational Physics **169**, 503 (2001).
34. T. Shimada, T. Yagisawa, and T. Makabe, Japanese Journal of Applied Physics **45**, L132 (2006).
35. Z. –K. Hsiau, E. C. Kan, J. P. McVittie, and R. W. Dutton, IEEE Transactions on Electron Devices **44**, 1375 (1997).
36. G. S. Hwang and K. P. Giapis, Journal of Vacuum Science and Technology B **15**, 70 (1997).

37. A. P. Mahorowala and H. H. Sawin, Journal of Vacuum Science and Technology B **20**, 1064 (2002).

38. R. J. Hoekstra, M. J. Kushner, V. Sukharev, and P. Schoenborn, Journal of Vacuum Science and Technology B **16**, 2102 (1998).

39. Y. Hirai *et al.*, IEEE Transactions on Computer-Aided Design **10**, 802 (1991).

40. R. Zhou, H. Zhang, Y. Hao, and Y. Wang, Journal of Micromechanics and Microengineering **14**, 851 (2004).

41. M. Fujinaga and N. Kotani, IEEE Transactions on Electron Devices, **44**, 226 (1997).

2. 3-D Monte Carlo Profile Simulation

2.1. Introduction

The development of profile simulators has been a great challenge due to the lack of a complete understanding of physical and chemical processes on surfaces, and yet there is great need for them due to the numerous compounded parameters involved in surface reactions that would make exploration by experimentation extremely laborious and expensive. It is well-known that the final feature profile and surface roughness are the results of competing effects such as etching, deposition, ion-bombardment-induced roughening and diffusion-induced smoothing, making the overall process a very complex one. It is, however, necessary to account for all dominant physical and chemical processes in order to study the effects of the competing processes and accurately model their underlying mechanisms.

There have been many efforts made in developing profile simulators in 2-dimensions, and some of the common techniques employed include string methods[1,2], level-set methods[1], and cellular-based methods[4,5]. Although many of the simulation techniques that were deemed successful in 2-dimensions have been extended to 3-dimensions[6-8], it is highly possible that the unresolved issues that were present in the 2-dimensional simulations were also carried over to the 3-dimensional simulations. Furthermore, it is conceivable that these extensions to 3-dimensions will face additional problems that were not encountered in 2-dimensional cases, as discussed in Chapter 1.

Amongst the different existing algorithms used to simulate surface profile evolution, the Monte Carlo technique, in conjunction with a cell-based method, was preferentially used in this work. The main advantage of using this method over others is

that it is relatively easier to incorporate physical and chemical processes during the etching process because of the lack of convergence issues faced by other methods. Stochastic variables were sampled from certain probability distributions to predict the behavior of a real system, and discretization of the simulation domain allowed us to keep track of surface composition at each position.   In addition, the cellular representation allowed for the modeling of the surface roughening process, which is difficult to model by deterministic techniques due to its stochastic nature.   Although the combination of cellular representation for the surface with Monte Carlo modeling of mass transport and kinetics expectedly requires greater computational power and memory, current computer architecture allows for this method to be feasible.

2.2.   3-dimensional cellular representation for tracking material compositions

The simulation domain was discretized into cellular cubes, each containing certain materials.   The length of each cell was 2.5 nm which is comparable to the dimensions associated with atomic mixing in ion induced processes[9].   Therefore, the composition in each cell was assumed to be uniform without a compositional gradient.

Particles were introduced randomly along the source plane above the surface, which represents the plasma sheath, one at a time, and they were tracked until they impinged on the surface cells.   The compositional information on each cell was stored and updated each time the incoming particle interacted with that cell in order to track the deposition and removal of materials.   If the particle was scattered from the surface, the particle was tracked again until it struck another part of the surface or left the top of the

simulation domain. The atomic density was assumed to be constant, i.e. the number of particles in each cell was kept constant by removing or adding cells as the cells become empty or overfilled to model the etching and deposition during the process. Each cell was labeled according to different material types, such as a gas or empty cell, a polysilicon cell, or a photoresist cell. This process was repeated for more than a million times, which provides a sufficiently large sample for simulating a real system.
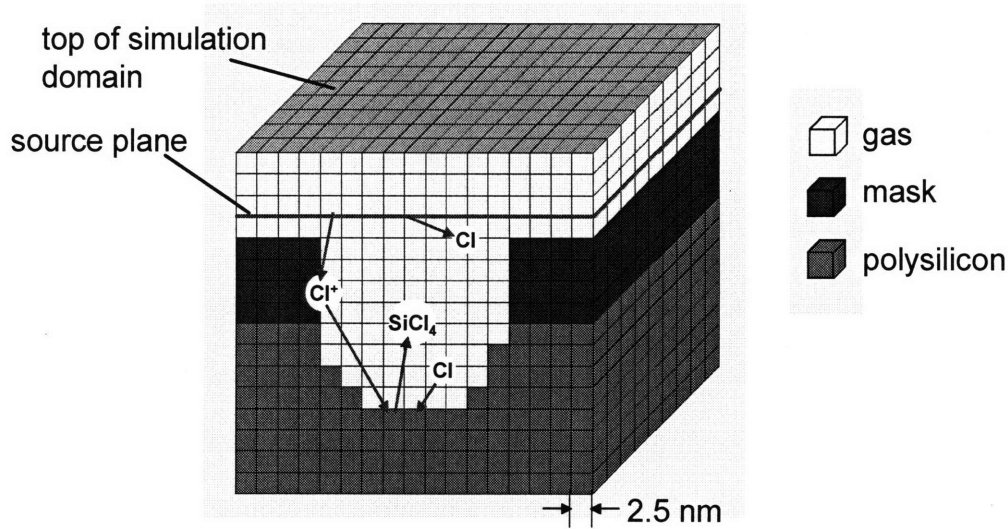
Figure 2.1: 3-D simulation domain. Simulation domain was discretized into cellular cubes with dimension of 2.5 nm. Particles were introduced from the source plane one at a time, and as they interact with the surface, the surface composition information was updated to track the etching and deposition of materials during the process.

A periodic boundary condition was applied to four sides of the domain so that a feature represents an infinite surface with line and space, and a particle that leaves the domain from one side appears on the opposite side. Particles in the sheath were assumed to be collisionless due to standard low pressure conditions, and therefore each particle was introduced serially, and the interactions between particles were neglected.

The cellular representation of the surface allows flexibility in surface conformations, including patterned films as well as blanket films, as shown in Figure 2.2. The angle of incidence of incoming ions can also be controlled, and this is very useful in analyzing the effect of angles of incidence on surface roughening processes.

(a)   (b)
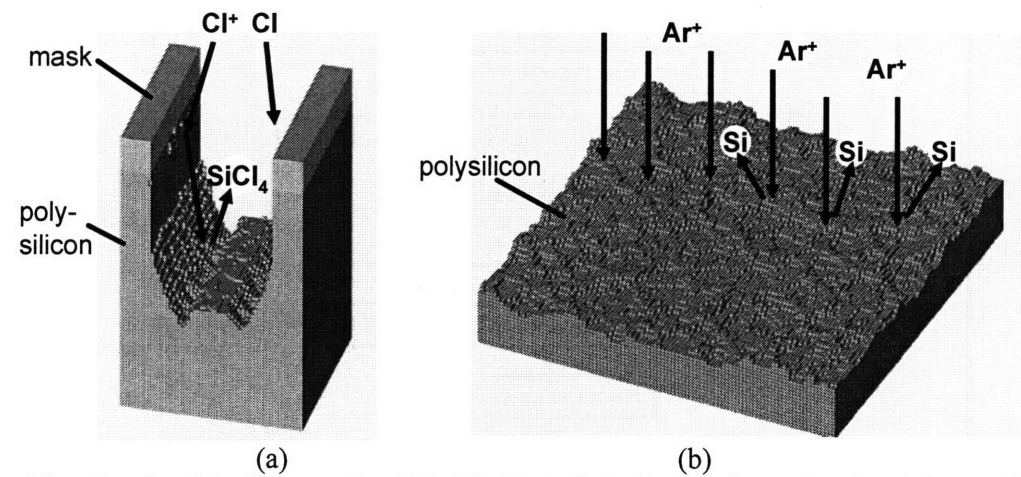
Figure 2.2:   Sample of simulation results. This 3-D Monte Carlo simulator is capable of modeling profile evolution (a) as well as the roughening of blanket film in sputtering process (b).

A flowchart of the simulation is shown in Figure 2.3. Each step in the flow chart will be discussed further in the following sections.
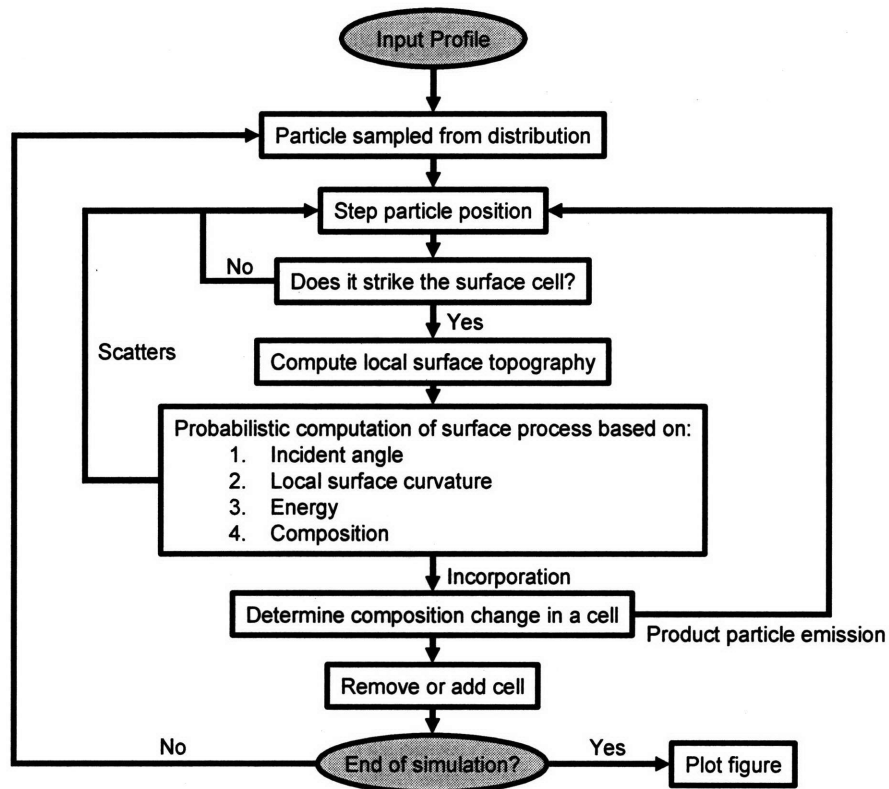
Figure 2.3: Algorithm of the simulation process. The initial position, composition and trajectory of a particle were sampled from their respective distributions, and the particle was tracked until it reached the surface cell. The incident angle and local surface curvature were determined by estimating the local surface topography. The surface process is determined based on this incident angle and surface curvature, the ion energy and the composition in the interacting cell. If the particle was incorporated, the compositional information of the cell was updated, and depending on the number of particles in the cell, a cell was added or removed. If the particle was not incorporated, it was scattered from the surface and was tracked until it hit another part of the surface. This process was repeated more than a million times.

2.3. Trajectories of ions and neutral particles

Ions and neutrals were introduced from the source plane above the top of the feature at a random lateral position. Ions were then transported directionally towards the surface due to the electric field generated, while neutrals were transported with no preferred direction. The trajectories of ions and neutrals were determined by random sampling from Gaussian distributions and cosine distributions, respectively[10]. The

particle was stepped one cell length at a time until it reached a surface cell. Surface

interactions were determined probabilistically based on a surface kinetics model, and if

the particle was reflected from the surface, its trajectory was tracked until it reached

another surface. This process was repeated until the particle was adsorbed onto a surface

cell or had escaped from the top of the simulation domain. Ions were assumed to reflect

specularly about the surface normal, with a small dispersion characterized by a Gaussian

distribution. Neutrals were assumed to scatter non-specularly, where the particles were

re-emitted from the surface after equilibrating thermally, and their trajectories were

characterized by a cosine distribution about the surface normal.
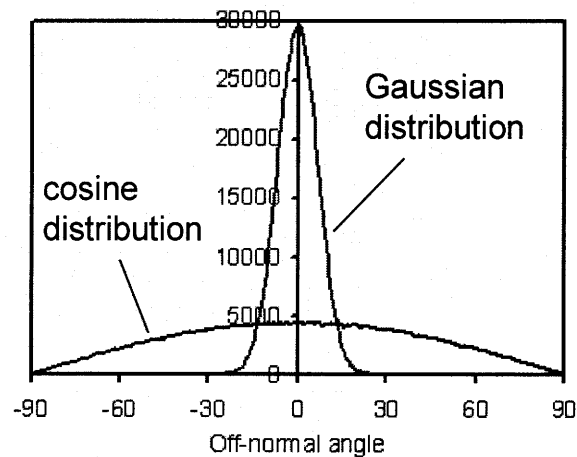
Figure 2.4: Particle distributions. Ion and neutral trajectories were sampled from Gaussian distribution and cosine distribution, respectively.

2.4. Computing a local surface topography

Interface or surface cells were defined as cells with at least one gas cell within its

six neighboring cells (top, bottom, left, right, front, back). Incoming particles were

allowed to interact with surface cells to simulate the etching and deposition of materials.

The etch profile and roughness are strongly affected by the variations in flux as well as

43

the scattering of particles from the surface, therefore it is crucial to determine accurately which cell a particle should interact with in order to prevent any artifacts. To compute the flux to a surface and the scattering of particles from a surface in the 3-D profile simulation, a smooth polynomial surface was fitted to the surface cells in the local area where the particle has struck (Figure 2.5). This method has a significant advantage over other methods, as explained below.

(a)   (b)
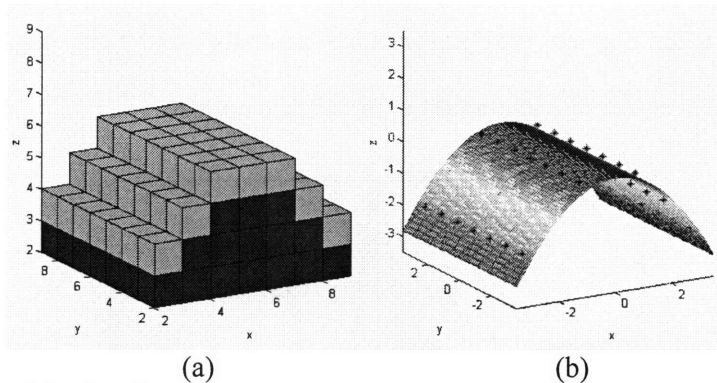
Figure 2.5:   Polynomial surface fitted to the neighboring surface cells. Local area of the surface in the range of ±3 cells (a) was fitted with the 2nd order polynomial surface (b). Center points of surface cells, shown in black, were used in least squares fitting.

If the surface were represented by the outer edges of the surface cells, exaggerated shadowing would occur and the flux to the protruded cells would be increased, which would lead to unrealistic surface profiles. To prevent these artifacts, Mahorowala developed a 2-D profile simulator which uses the lines connecting the centers of adjacent cells to compute the flux to the surface[5]. However, this method is not appropriate for the 3-D profile simulation. It is possible to connect the centers of adjacent cells to form triangular planes (Figure 2.5a, b), but there are some cases where planes cannot be formed. For example, when two cells are stacked, the surface is represented by a line instead of a plane, and this prevents any flux to these cells (Figure 2.5c, d). Therefore, a more complex algorithm would be required in order to apply a similar method in 3-D.

44

There are some simulators implementing the mesh of points connected by line segments to form triangular facets, but they often result in topological instabilities such as surface loops that are formed when the etching front intersects with itself[11]. These surface loops must be detected and removed as they are formed to prevent any unphysical surface, and this requires additional computation time.

(a)   (b)   (c)   (d)
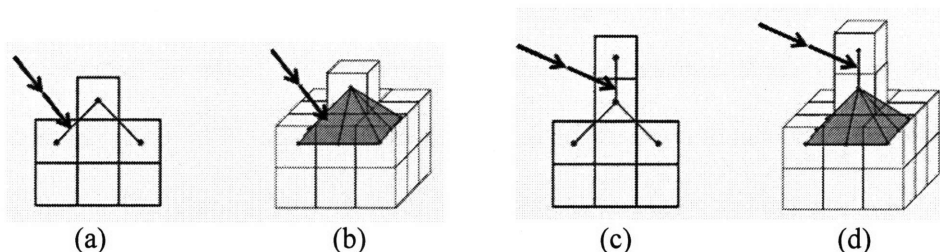
Figure 2.6:   Comparing 2-D and 3-D surface representations. In 2-D simulation, surface may be represented by simply connecting the center points of neighboring cells as shown in (a) and (c). This may be extended to 3-D simulation by forming a series of triangular planes as shown in (b) and (d). However, in (d), part of the surface is represented by a line instead of a plane. This is unphysical because line cannot receive any flux, preventing any flux to these cells. Therefore, a fitted polynomial surface was used instead.

By allowing the incoming particles to interact with the polynomial surface instead of a cubic cell surface, exaggerated shadowing and increased flux to the protruding cells can be prevented. In addition, least squares fitting would be a straight forward method with minimum convergence problems such as surface loops that are often created in string-and-node and triangular-mesh algorithms. By fitting a second or higher order polynomial, curvature of the surface can also be approximated, which plays an important role in simulating surface roughening mechanisms.

2.4.1. Least squares polynomial fitting

The least squares fitting of a polynomial is a simple, yet computationally intensive method. Fortunately, today's computational power allows this method to be viable. The general equation for least squares fitting is

$$S = \sum_{i=1}^{n}(z_i - f(x_i, y_i))^2 \qquad\qquad\qquad \text{(Eq. 1)}$$

where z_i is the ith data point, S is the sum of the squares of the vertical deviations of a set of n data points from a function f. In the model, a 2nd order polynomial surface was fitted to the surface cells in the range of ±3 cells (Figure 2.5). This range was chosen so that the model could capture the surface curvature in the scale of interest, while minimizing the amount of computation that increases with range. A 2nd order polynomial, instead of a higher order polynomial, was chosen to minimize the numerical singularities as well as the amount of computation. Thus, in this model, function f is given by

$$f(x_i, y_i) = b_1 x_i^2 + b_2 y_i^2 + b_3 x_i y_i + b_4 x_i + b_5 y_i + b_6 \qquad\qquad \text{(Eq. 2)}$$

where $b_1 \sim b_6$ are unknown parameters to be determined. To solve for parameters b_n, the equations are written in matrix form,

$$\begin{bmatrix} x_1^2 & y_1^2 & x_1 y_1 & x_1 & y_1 & 1 \\ x_2^2 & y_2^2 & x_2 y_2 & x_2 & y_2 & 1 \\ x_3^2 & y_3^2 & x_3 y_3 & x_3 & y_3 & 1 \\ \vdots & \vdots & \vdots & \vdots & \vdots & \vdots \\ x_n^2 & y_n^2 & x_n y_n & x_n & y_n & 1 \end{bmatrix} \bullet \begin{bmatrix} b_1 \\ b_2 \\ b_3 \\ b_4 \\ b_5 \\ b_6 \end{bmatrix} \approx \begin{bmatrix} z_1 \\ z_2 \\ z_3 \\ \vdots \\ z_n \end{bmatrix} \qquad \text{(Eq. 3)}$$

or in matrix notation,

$$\mathbf{A} \cdot \vec{b} \approx \vec{z} \qquad\qquad\qquad\qquad \text{(Eq. 4)}$$

where $\mathbf{A}$ is an n-by-6 matrix where n is the number of cell center points, $\vec{b}$ is an unknown parameter vector with 6 components, and $\vec{z}$ is the z component for each cell center points. The goal is to find a solution $\vec{b}$ for the equation, which gives the minimum deviation of a fitted polynomial surface to the cell center points. This was

solved by premultiplying by the matrix transpose $\mathbf{A}^T$ and inverting to yield the solution vector

$$\vec{b} = \left(\mathbf{A}^T\mathbf{A}\right)^{-1}\mathbf{A}^T \cdot \vec{z}. \qquad\qquad\qquad (\text{Eq. 5})$$

This can be solved by LU decomposition or any other common methods for solving matrix equations.

2.4.2. Rotation of a coordinate system

The matrix described above may be ill-conditioned or solutions cannot be found depending on the surface conformation. For example, when the polynomial surface was fitted to neighboring cells on the sidewall (Fig. 2.7a), the fitted surface is a horizontal plane (Fig. 2.7b) instead of a vertical plane (Fig. 2.7c) which represents the surface more accurately.

(a)   (b)   (c)
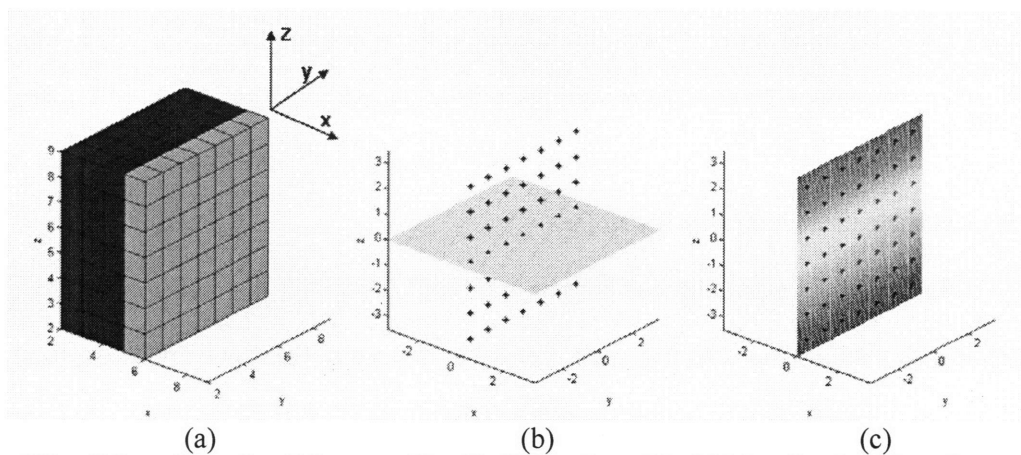
Figure 2.7: Polynomial surface fitting on a sidewall. If the polynomial which is a function of x and y were fitted to the sidewall (a), the least squares fitting does not give an accurate representation of the surface (b). The fitted surface is a horizontal plane (b) where as the more correct surface representation should be a vertical plane (c).

These problems can be avoided by rotating the coordinate system based on the surface structure. More precisely, z-direction vector was rotated according to the location

of a center of mass with respect to the center of the cell under consideration. This calculation is shown in Figure 2.8 in 2-D, for simplicity. The red point is the location of a center of mass within this range (±3 cells), and the z-coordinate in the new coordinate system points from the center of mass towards the center cell. See Appendix for more details. This rotation of coordinates allows for an accurate representation of the surface for any surface conformation.

| (a) | (b) | (c) |
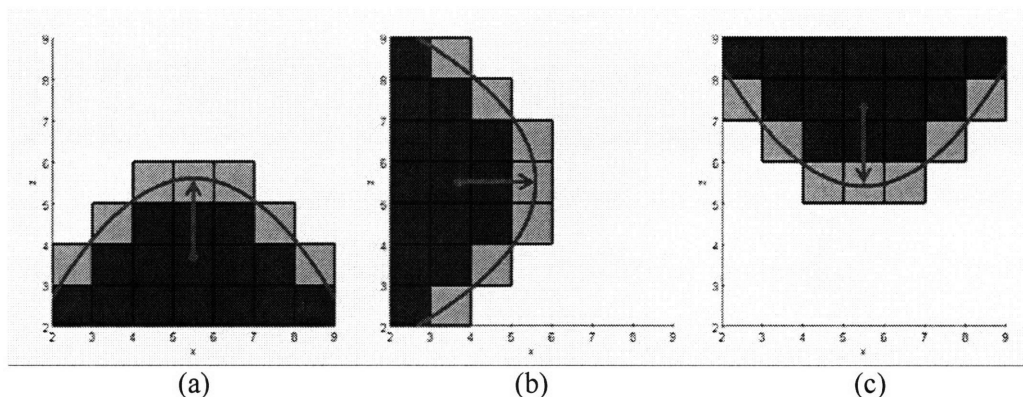
Figure 2.8: Calculation of the center of mass. The direction of z-coordinate was determined by the vector pointing from the center of mass (red point) to the center point of the cell under consideration. Based on the surface conformation, the new z-coordinate could point up (a), to the side (b), down (c) or any other directions.

2.5.   Particle interaction with the surface

Each particle was advanced step by step until it reached the surface cell. The particle was then advanced further until it crossed the locally fitted polynomial surface. The intersection of a trajectory and the polynomial surface was determined by a simple bisection method. The particle interacted with the cell where the intersection point was located. If the intersection point were located in an empty (gas) cell or in a non-surface cell, the closest surface cell along the surface normal was selected.
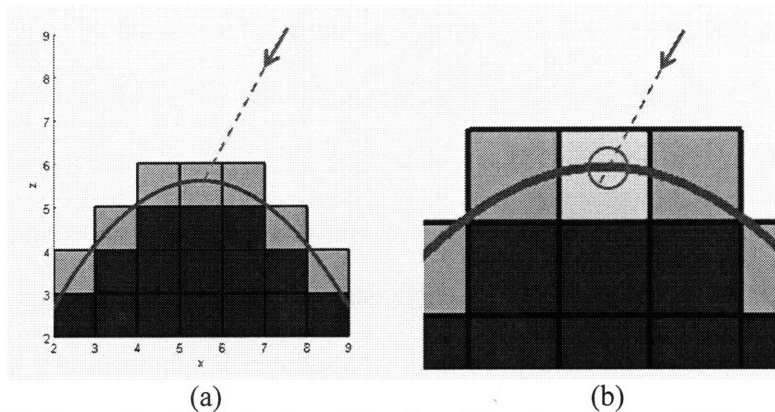
Figure 2.9: Particle intersecting the fitted polynomial surface. When the particle reached the surface cell, the intersection of the particle trajectory and the fitted surface was calculated by a bisection method.

2.5.1. Surface processes

The Monte Carlo algorithm allowed for the incorporation of the physics and chemistry of the dominant processes in plasma etching by considering the probability of occurrence of each kinetic process on the surface. Surface interactions considered were: sticking or incorporation of particles into surface cells, scattering of ions and neutrals, ion-enhanced etching or physical sputtering of surface materials, and re-deposition of etching products. These interactions are highly dependent on many different factors such as the ion angle of incidence, surface curvature, surface composition, and ion energy[12,14]. Based on the surface processes that occurred, particles were either added or removed from a surface cell.

2.5.1.1. Angular dependence of etching yield and ion scattering

There are many studies showing the dependence of the ion's angle of incidence on surface etching rates[13,14]. The angular dependence varies greatly depending on the process conditions such as gas composition and surface materials, which can be characterized as either physical sputtering or ion-enhanced etching. Physical sputtering

involves energetic gaseous ions in a plasma to knock off, or sputter, the atoms from a target surface. Typically, the etching yield peaks at 60° to 75° off-normal to the surface (Figure 2.10), at which the incoming atoms can most efficiently transfer momentum to the surface atoms for sputtering. The theory of sputtering will be discussed in more detail in the next chapter. In ion-enhanced etching, such as in chlorine-based plasma, there is no yield peak as seen in sputtering. Instead, the yield remains constant up to certain off-normal angles and decreases monotonically as the angle of incidence becomes more grazing[14]. In both cases, the etching yield drops at high off-normal incidence due to the increase in ion scattering. The examples of normalized etching yield curves are shown in Figure 2.10.

Etching yield vs. angle of ion incidence

- ion-enhanced etching
- physical sputtering
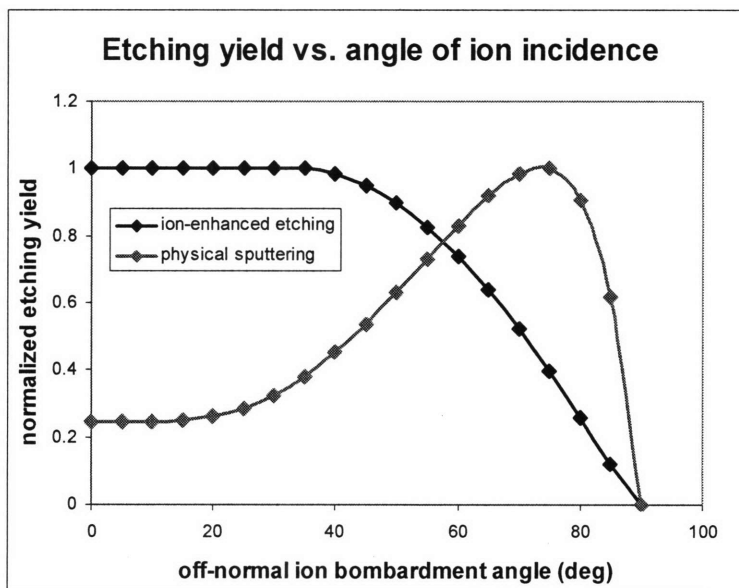
Figure 2.10: Angular dependences of ion-enhanced etching and physical sputtering on etching yield. The ion-enhanced etching (Cl2 plasma) yield remains constant up to a certain off-normal angle and decreases monotonically at high off-normal incidence, whereas the physical sputtering yield increases with off-normal angles of incidence and peaks at around 60° to 75°.

Calculation of the angular dependence of the etching yield proceeded next by combining the concept of probability with the angular dependence of etching yield data

50

obtained from beam experiments[5,14]. The probability of each incoming ion to be incorporated into a surface cell and cause etching was determined from the etching yield curve. If the ion was not incorporated into the surface cell, it would scatter from the surface without causing etching, and would be tracked until it reached another part of the surface. In other words, the etching yield curve represents the reaction probability, and the scattering probability is given by one minus the reaction probability, as shown in Figure 2.11. As noted previously, in both ion-enhanced etching and physical sputtering processes, the decrease in etching yield at high off-normal ion angles of incidence is due to the increase in scattering probability. In physical sputtering, however, the yield is also decreased at low off-normal ion bombardment angles because the momentum of incoming ions cannot be transferred effectively to the surface to cause bond breakage, and not because of the particles scattering from the surface. Although some ions may still be reflected from the surface after bombarding the surface at near normal incidence, most of the incident energy will be transferred to the surface (>90 %), and the resultant reflected ions are less likely to cause any etching[15]. It was therefore assumed that scattering occurs only at very grazing ion angles of incidence, as shown in Figure 2.12.
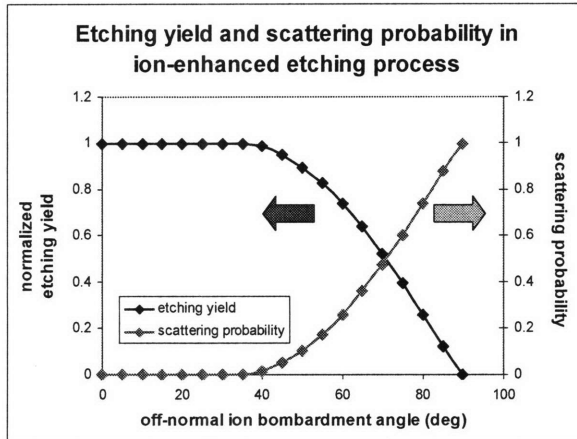
Figure 2.11: Ion scattering probability in ion-enhanced etching process. The etching yield decreases monotonically with the off-normal ion bombardment angle, and the scattering probability increases with the off-normal ion bombardment angle.
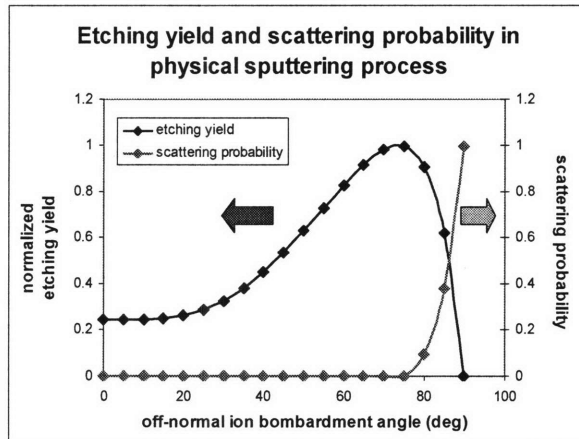
Figure 2.12: Ion scattering probability in physical sputtering process. The etching yield increases with the off-normal ion bombardment angle, peaks at around 75°, then decreases at a grazing ion angle of incidence due to high scattering probability. The low etching yield at near normal angles is due to the inefficiency of momentum transfer by ions to the surface to knock atoms off the surface.

2.5.1.2.   Curvature dependence on etching yield

According to sputter theory, the etch rate also depends on the local surface curvature[12], which is generally difficult to determine when cell-based methods are used. However, the use of polynomial surface fits allows for an approximation of the local surface curvature to be more straightforward, thus allowing the etch rates to be modeled

52

more effectively. More details on sputter theory and curvature dependence will be discussed in the next chapter.

2.5.1.3. Surface kinetics modeling

The Monte Carlo algorithm, combined with cellular surface representation allows for the incorporation of detailed surface kinetics, which in turn determines the etch yield based on ion energies, surface composition, incoming flux, and angles of incidence. Mixing-layer kinetics modeling, proposed by Kwon and Sawin[16] and expanded by Guo et al[17], is suitable for incorporation into this type of profile simulator due to its robustness. The model postulates that there exists a well-mixed layer between the plasma and the substrate where all atoms are randomly bonded to each other. This "mixing-layer" is formed by the continuous bombardment of ions, and all surface processes are assumed to occur in this region. The surface processes include ion incorporation, absorption of neutrals, physical sputtering, vacancy generation, ion-induced etching, and the recombination of atoms on the surface. More details on the model can be found elsewhere[17].

2.5.2. Surface normal calculation

Since a particle's interaction with a surface is a strong function of its incident angle, the calculation of the surface normal is crucial in developing an accurate profile simulator. Calculation of the surface normal is particularly challenging in a cell-based method because the surface angles and curvatures cannot be well represented using an array of cells. In the 2-D profile simulator developed by Mahorowala, a straight line was

fitted to the neighboring cells using a least-squares approximation[5], and the surface normal was calculated using this line. While this approximation was shown to be sufficient for a 2-D profile simulation, in a 3-D simulation where the primary goal is to investigate surface roughening mechanisms, the approximation of a surface with a plane is not sufficient since it cannot capture the surface curvature and tends to make the surface unnaturally smooth. Again, these problems can be avoided by using a fitted polynomial surface. The surface normal was calculated at the intersection point of a trajectory vector and the fitted polynomial surface. This method allows for an accurate determination of the surface normal because as shown in Figure 2.13, the surface normal is different depending on the location of the intersection of the particle trajectory with the fitted polynomial surface, even within the length of one cell. The polynomial surface was always fitted to the local area where the particle impinged on the surface, as shown in Figure 2.14a and 2.14b, and therefore depending on the location of the ion impingement, the polynomial was fitted to a different set of surface cells. It is not necessary, however, to fit a different polynomial to a surface every time a particle impinges onto it. The surface was re-fitted only when the local surface conformation changed, in other words, when the cells were removed or added within this fitting range. By retaining the information of the polynomial surface and updating it only when the surface conformation changed, the amount of computation time can be reduced significantly.

(a)   (b)
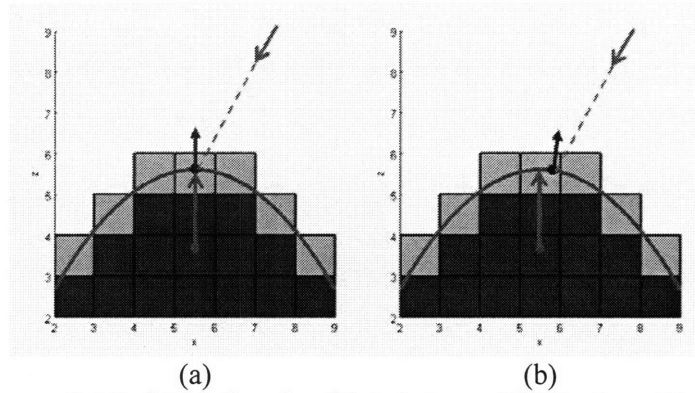
Figure 2.13: Surface normal at the intersection of particle trajectory and fitted polynomial surface. Although the particle interacts with the same cell in both (a) and (b), slight difference in the location of intersection results in a different angle of incidence.

(a)   (b)
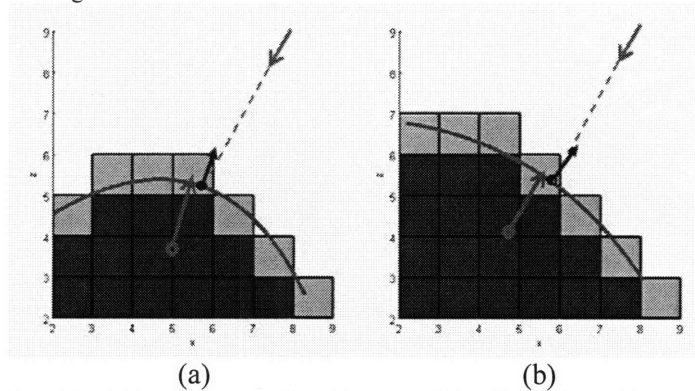
Figure 2.14: Intersection of particle trajectory and fitted polynomial surface. Depending on where the particle impinges on the surface, the polynomial surface is fitted to the different set of surface cells.

The main disadvantage in using a higher order polynomial surface instead of a planar surface is that the trajectory and the polynomial surface may have multiple intersection points, and it is at times not obvious which the correct intersection point is where the particle has struck. A second order polynomial was thus used instead of higher order polynomials because it minimizes the problem of multiple intersections while effectively modeling the curvature of a real surface.

When ion scattering had occurred, the particle was reflected from the fitted polynomial surface where it had initially struck, at a specular angle about the surface normal with a small dispersion (Figure 2.15a). Similarly, when a neutral particle was

scattered, it was re-emitted from the surface with a cosine distribution about the surface normal (Figure 2.15b). The particle was tracked until it reached another part of the surface or escaped from the top of simulation domain. Similarly, etched materials may leave the polynomial surface with a certain angular distribution and reach another part of the surface to be re-deposited.

(a)   (b)
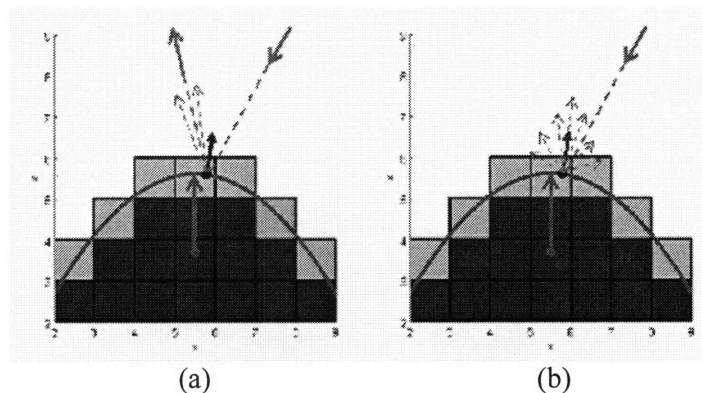
Figure 2.15:   Scattering of a particle from the fitted polynomial surface. Ion scatters at specular angle about the surface normal, with small dispersion (a), where as neutral particle is adsorbed and re-emitted from the surface, resulting in a wider (cosine) distribution (b).

2.6.   Surface advancement algorithm

Etching and deposition of materials were tracked by combining a moving boundary layer model of an ion-bombarded surface with cellular representation of the surface. It is known that ion bombardment and surface diffusion create a well-mixed boundary layer on a surface exposed to plasma[15,16]. In the moving boundary layer model, this layer is assumed to move with the interface as etching or deposition proceeds[5]. The boundary layer receives fluxes of particles from both gas and solid phases, as shown in Figure 2.16, and the composition of the surface layer is determined by balancing the two fluxes. For example, if particles were removed from a surface, the interface would

recede and the removed particles would be added to the mixed boundary layer. Similarly, if particles were deposited onto the surface, the interface would grow and some of the materials in the boundary layer would be depleted in order to keep the overall particle density constant. The thickness of this moving boundary layer, or well-mixed layer, was determined to be about 2.5 nm from angle-resolved x-ray photoelectron spectroscopy (XPS) measurements on a silicon surface etched by Cl_2 plasma[18], as well as from molecular dynamics simulations of ion-induced etching of a silicon surface by fluorocarbon plasma[19].
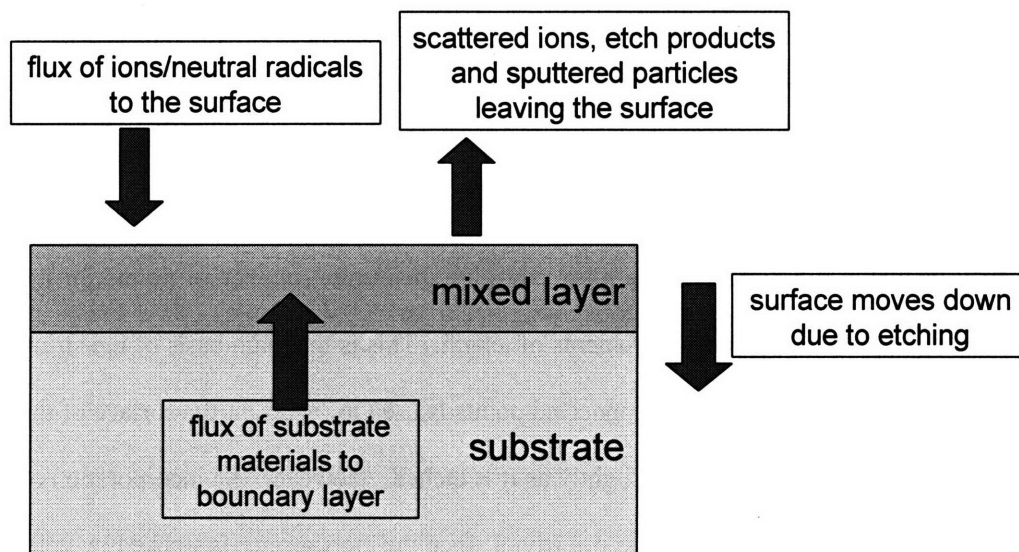
Figure 2.16: Moving boundary layer model in etching. The well-mixed boundary layer moves as the surface moves due to etching, and the composition in the layer is determined by balancing the fluxes from gas phase and solid phase during etching.

The moving boundary layer model was incorporated into the simulation by setting the cell dimension to be 2.5 nm, which is equivalent to the thickness of the boundary layer, and assuming uniform composition within each cell. Etching and deposition of materials were tracked by performing an elemental balance for a surface cell each time a reactant particle interacted with it, and the number of particles of each species in the cell

57

was subsequently updated. When a cell became overfilled with particles, a new cell was added, and the particles were divided equally among the two cells. When a cell became empty, it was removed to maintain a constant atomic density in the surface layer.

The moving boundary layer model is sufficient to describe the surface advancement if the surface remains flat during etching or deposition processes. In reality, however, there will be deviations from the flat surface due to both microscopic roughening and macroscopic surface conformations. An accurate surface advancement is necessary to avoid numerical artifacts such as voids and roughness on the order of one cell length, which would lead to an unphysical surface conformation. Theoretically, surface advancement proceeds at a rate equal to the etching or deposition rate along the local normal at each point on the surface, as shown in Figure 2.17. To compute the surface advancement perfectly, one must consider an infinite number of points on the surface moving at infinitesimal increments of length. This is the main basis of the string model[1], in which a dense mesh of connected points is used to represent the surface of the material, and each point is shifted slightly as it is etched. However, the incorporation of this theory into a cell-based model is not trivial since the etch surface is tracked by cells instead of points, and cells cannot be added or removed in an exact manner along the local normal to the surface. Surface advancement is further complicated by surface smoothing mechanisms such as thermal diffusion[12] and diffusion and surface relaxation induced by ion bombardment[20,21]. To model both "surface advancement along the surface normal" and "smoothing due to surface diffusion" in our 3-D cell-based simulation, cell addition and removal were effected based on two criteria: how close the

58

direction of surface growth is to the surface normal, and how much the surface growth can keep the surface smooth. This algorithm will be described using examples.

(a)   (b)
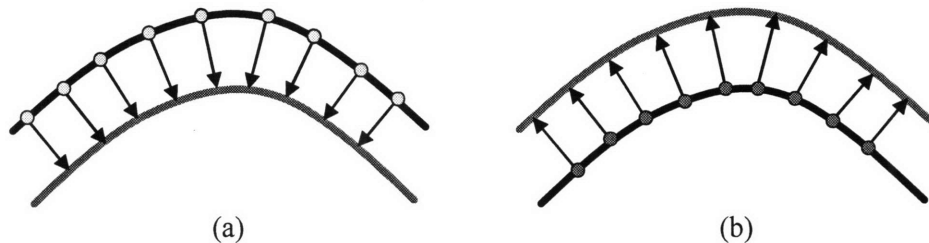
Figure 2.17: Surface advancement along the local normal. In theory, surface advances along the local normal at each point on the surface proceeds at a rate equal to the etching (a) or deposition (b) rate.

For deposition, a new cell must be deposited when a cell is overfilled, and the excess particles will be passed from the overfilled cell to a new cell to maintain a constant atomic density on the surface layer. The position of a new cell is selected from the neighboring ± 1 cell, where in 3-D, there will be a maximum of 26 positions to select from. For simplicity, all the examples will be shown in 2-D. In Figure 2.18a, the yellow cell at the center is overfilled with particles, and the two possible positions for a new cell are labeled with numbers. The position above cell 2 is not considered because it will create a hanging cell which is unphysical, and other neighboring cell positions are not considered since a new cell can be added only to a location that is empty. To advance a surface approximately along its surface normal, the cell should be added to the position closest to the surface normal direction.
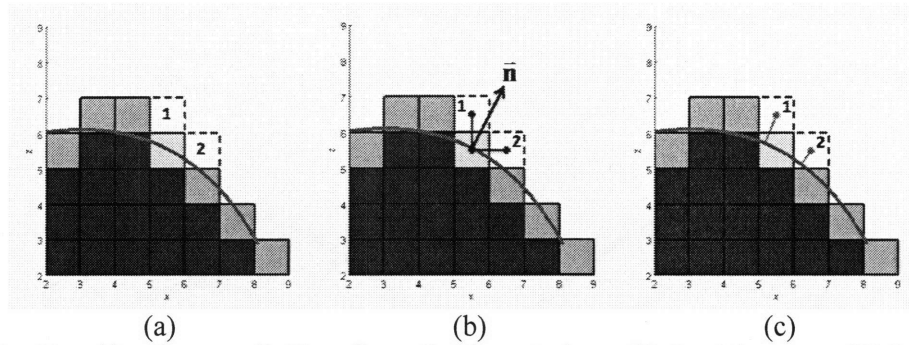
Figure 2.18: Deposition of a new cell. The yellow cell at the center is overfilled, and the two possible locations for a new cell are labeled with numbers (a). To advance a surface approximately along the surface normal, the location of a new cell must be closest to the surface normal direction, $\bar{n}$ (b). At the same time, the addition of a new cell should keep the surface smooth due to the diffusion-caused smoothing. This is done by calculating the distance from the fitted surface to each possible location and adding a cell at the location closest to the fitted surface, as illustrated in (c).

To determine how close the new cell is to the direction of the surface normal, the angle between the surface normal and the line connecting the centers of the overfilled cell and each new cell location is calculated. In this example, cell 1 has a smaller angle of deviation from surface normal than cell 2 (Figure 2.18b), and therefore a new cell should be added to cell 1 if the surface must advance along the surface normal, $\bar{n}$, as much as possible. To consider how the addition of a new cell affects the surface smoothness, the distance from the fitted surface to each possible location is calculated. More specifically, the normal distance from the fitted polynomial surface to the center of each cell location was computed. The surface can be kept smooth by adding a cell closest to the fitted surface because the deviation of the re-fitted polynomial (following the addition of a new cell) from the original polynomial surface is minimized, and a drastic change in surface conformation can be avoided. As shown in Figure 2.18c, cell 2 is closer to the fitted surface, and therefore the surface is kept smooth if a new cell is added to this location.

The two factors must be balanced so that the surface advances along the local surface normal while keeping the surface smooth. This is done by formulating a simple optimization function,

$$f(\theta_i, d_i) = a\theta_i + bd_i \qquad\qquad\qquad (Eq.\ 6)$$

where θ_i and d_i are the angle of deviation from the direction of the surface normal and the distance from the fitted polynomial surface to the ith cell , respectively. Figure 2.19 shows the angles of deviation and the distances from the fitted polynomial cell for the example shown in Figure 2.18. Pre-factors a and b are weighting factors for the "normal" and "smoothing" components of the surface advancement process respectively, and their values will be determined and discussed later.

(a)   (b)
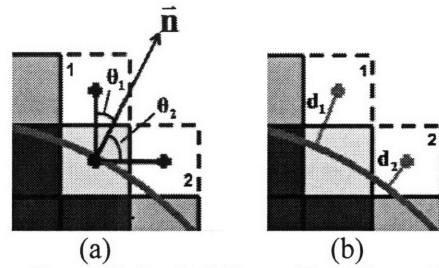
Figure 2.19: Deposition of a new cell, considering both "normal" and "smoothing" components of the surface advancement. In (a), angle of deviation from surface normal direction is shown for the two cells. In (b), the distance from the fitted polynomial surface to each cell considered is shown.

In view of the complexities mentioned above, one may think that modeling etching should be easier than deposition because a cell is simply removed whenever it becomes empty. However, this will invariably lead to various unphysical artifacts such as hanging and floating cells. In order to prevent these artifacts, a surface advancement algorithm similar to that used in the deposition process was employed. Within our algorithm, a solid cell to be removed was selected from a group of solid cells within a range of ±1 cell from an empty cell. In the etching process, the empty cell, as well as

61

neighboring surface cells, are considered as possible cells to be removed. If a non-empty cell is to be removed, the particles in this cell will be passed on to an empty cell. In Figure 2.20, the center cell (cell 2) is empty. The cell to be removed was chosen among three possible cells, which included the two other neighboring surface cells (1, 3). The angle of deviation, θ_i, from the surface normal, $\bar{n}$, was determined for each cell as shown in Figure 2.20b. The angle of deviation from the surface normal of the empty cell (cell 2) is assumed to be zero (not shown in the figure) because it is closest to the normal vector. Thus, the removal of cell 2 will allow the surface to advance closest along the surface normal. The distance from the fitted surface to each cell, d_i, was also calculated in a similar fashion as in the case for deposition (Figure 2.20c). To keep the surface smooth, the cell that has the largest distance above the fitted surface must be removed. The removal of a cell furthest from the fitted polynomial surface allows the re-fitted polynomial (which is performed after the removal of a cell) to be least deviated from the original polynomial, whereas the removal of a cell closest to the fitted surface will enhance roughening by drastically changing the surface conformation. Thus, in this context, removal of cell 1 will keep the surface smooth compared to the removal of other cells.

(a)   (b)   (c)
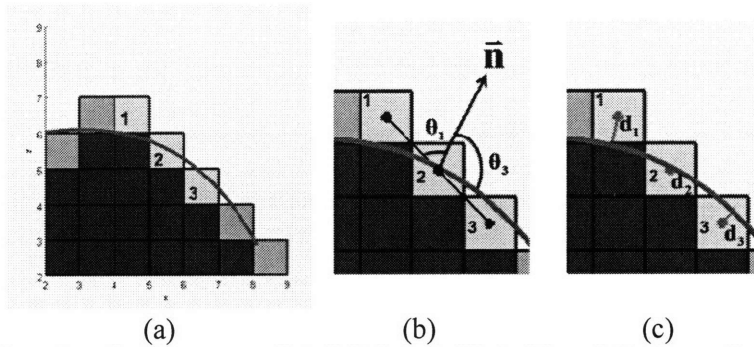
Figure 2.20: Etching of a cell. The center cell (cell 2) is underfilled. The neighboring surface cells and the underfilled cell are considered as possible cell to be removed (a). The algorithm is similar to the deposition case. The angle of deviation from the surface normal (b) and the distance from the fitted surface (c) were calculated for each cell.

The weighting factors a and b, which correspond to the extents of "the growth of the surface along the direction of its surface normal" and "the smoothing of the surface due to diffusion," respectively, were fixed by matching the surface advancement to a theoretical scenario for the etching and deposition of various macroscopic surface features. Theoretically, if the surface is etched by normal ion bombardment with uniform flux, the initial macroscopic surface features are retained during etching, as shown in the example in Figure 2.21a. Similarly, when the particles are deposited onto a surface with macroscopic features, the initial surface conformation is retained (Figure 2.21b).

(a)   (b)
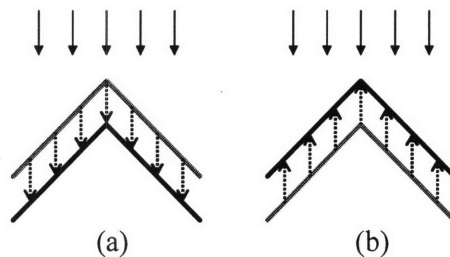
Figure 2.21: Theoretical surface advancement: Direct etching (a) and deposition (b). Macroscopic surface features are retained when the surface is etched by normal ion bombardment (a) or when the particles are deposited onto the surface with normal incidence.

Various macroscopic features were explored. For simplicity, all features are shown in 2-D, where the heights along the axis into the page were averaged. The

simulations were done in a 100x100x100-cell domain, and the initial features were constant in the direction that points into the page. The progression of the surface profile, averaged across the coordinates of the axis that points into the page, was plotted in 2-D.

(a) a/b = 0.0 (b) a/b = 0.3 (c) a/b = 0.5

(d) a/b = 0.0 (e) a/b = 0.3 (f) a/b = 0.5

(g) a/b = 0.0 (h) a/b = 0.3 (i) a/b = 0.5
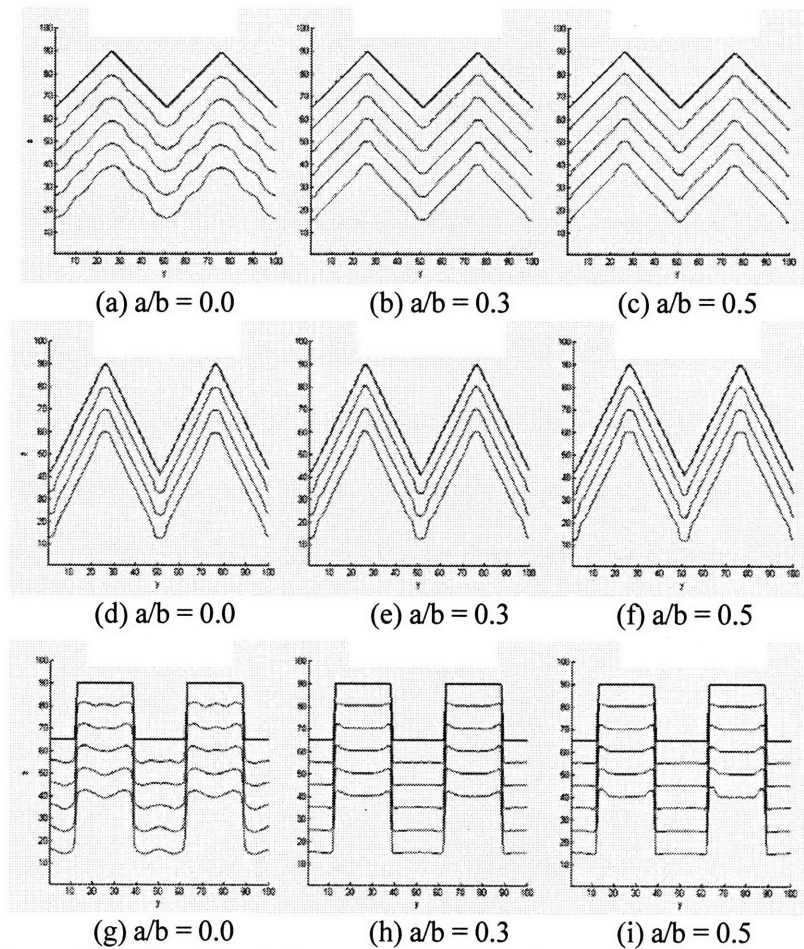
Figure 2.22: Direct etching of macroscopic features. Plots of the surface profile showing its evolution as the value of the ratio of a to b (i.e. the ratio of "normal" to "surface smoothing" weight factors) was varied from 0 to 0.5 for peaks with a 45° slope (a – c), a 63° slope (d – f), and a surface with two rectangular blocks (g – i).

In Figures 2.22a, b, and c, the two peaks (45° slopes), shown in red, were etched at normal incidence, with a ratio of a to b at 0, 0.3 and 0.5, respectively. In Figure 2.22a, where the smoothing of the surface was maximized, the surface had some

curvature which was enhanced as the surface was etched. The rounding of the peaks and valleys was caused by the fact that the surface conformation was kept as close as possible to the fitted polynomial surface, and this rounding resulted in instability at the surface, leading to excessive curvatures on other parts of the surface as well. As the ratio was increased from 0.0 to 0.3, in other words, as the weight on the "growth of the surface along its surface normal" was increased, these artificial curvatures decreased. When the ratio of a to b was 0.3 the surface retained its initial conformation, which matches the theoretical scenario for surface advancement that was mentioned earlier. Small rounding of the peaks and valleys due to the polynomial surface fitting was still observed, but it was not as significant as the case where the ratio of a to b was 0. The slope of the feature was also retained, without any artificial curvatures. When the ratio of a to b was increased to 0.5, the result was comparable to that of 0.3. Similar tests with other macroscopic features are shown in Figure 2.22d-i. In the case of the surface with very pronounced peaks (63° slopes) (Figure 2.22d, e, f), the results for 3 different ratios of a to b were comparable to each other. For the surface with two blocks (Figure 2.22g, h, i), an a to b ratio of 0 (Figure 2.22g) resulted in a surface with many curvatures, as seen in Figure 2.22a. When the ratio of a to b was 0.3, the surface mostly retained its initial conformation, though upon increasing the ratio to 0.5 (Figure 2.22i), the top corners of the blocks were sharpened, causing an artifact. This may be attributed to the decreased weight of the "smoothing" component in the surface advancement algorithm. Sharpening of surface features also occurred for a to b ratios above 0.5, especially for peaks which have sharp vertices as illustrated in Figure 2.23. As the features became even more pronounced, more artifacts such as hanging cells were formed, leading to inaccurate

results. While ratios between 0.3 and 0.5 may be employed, there is no point choosing a value above 0.3 since it minimizes the excessive sharpening of surface features while avoiding the occurrences of artificial curvatures on the surface. Within the validity of our theoretical mechanism for surface advancement, these results suggest that an a to b ratio of about 0.3 is optimal.
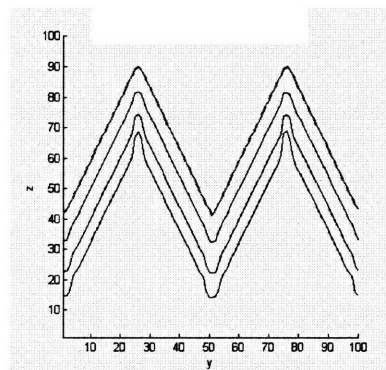
Figure 2.23: Sharpening of the peak at a/b = 0.7. When the peaks with 63° slopes were etched with a to b ratio of 0.7, undesirable sharpening of the peaks occurred.

Similar tests were done for deposition (Figure 2.24). Some rounding of the peaks, valleys and corners were observed in all cases due to the nature of the deposition process. For the peaks with 45° and 63° slopes (Figure 2.24a-f), variation in the ratio of a to b did not make any significant difference. However, for the surface with two rectangular blocks, an a to b ratio of 0 resulted in a surface with small curvatures that were not present in cases with higher ratios. This is similar to the curvatures observed in cases where etching was considered. For a ratio of a to b above 0.5 (not shown), the peaks sometimes became sharp, and instability of the surface resulted in artificial roughness. Figure 2.25 shows peaks with a 63° slope etched using an a to b ratio of 0.7. Although the sharpening of the peaks was not as significant as in the case of etching, the surface appeared to have a preferred direction for growth at the peak. In addition, some

instability of the surface was observed, resulting in an undesirable roughening of the surface. Therefore, an *a* to *b* ratio of about 0.3 in the case of deposition yields reasonable results, similar to the etching test cases.

(a) a/b = 0.0	(b) a/b = 0.3	(c) a/b = 0.5
d) a/b = 0.0	(e) a/b = 0.3	(f) a/b = 0.5
(g) a/b = 0.0	(h) a/b = 0.3	(i) a/b = 0.5
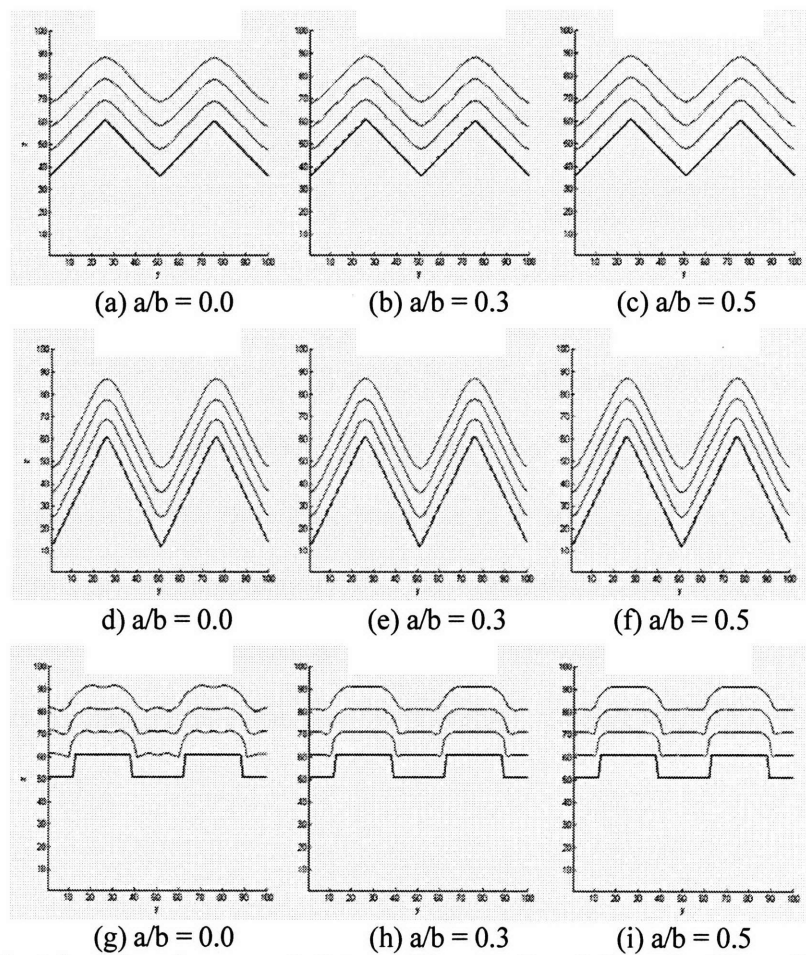
Figure 2.24: Direct deposition of macroscopic features. The ratio of a to b (i.e. ratio of "normal" to "surface smoothing" components) was varied from 0 to 0.5 for peaks with a 45° slope (a – c), a 63° slope (d – f), and a surface with two rectangular blocks (g – i).
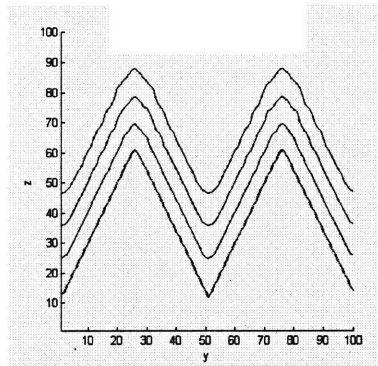
Figure 2.25: Sharpening and instability of the surface at a/b = 0.7. Increasing the a to b ratio to 0.7 resulted in an undesirable sharpening and instability of the peaks.

Direct etching and deposition were also tested on half-cylindrical features. The radius of the cylinder was varied from 5 cells (12.5 nm) to 40 cells (100 nm). When the cylinder was etched using an a to b ratio of 0, its surface features became distorted, regardless of its size (Figure 2.26a, d, g), and some instabilities were also observed on the horizontal surfaces as well. All features were well retained for a ratio equal to 0.3 or 0.5 (Figure 2.26b, c, e, f, h, i), but when the ratio was increased to 0.7, some sharpening of the features occurred (not shown). Therefore, the best choice for the ratio of a to b was still 0.3.
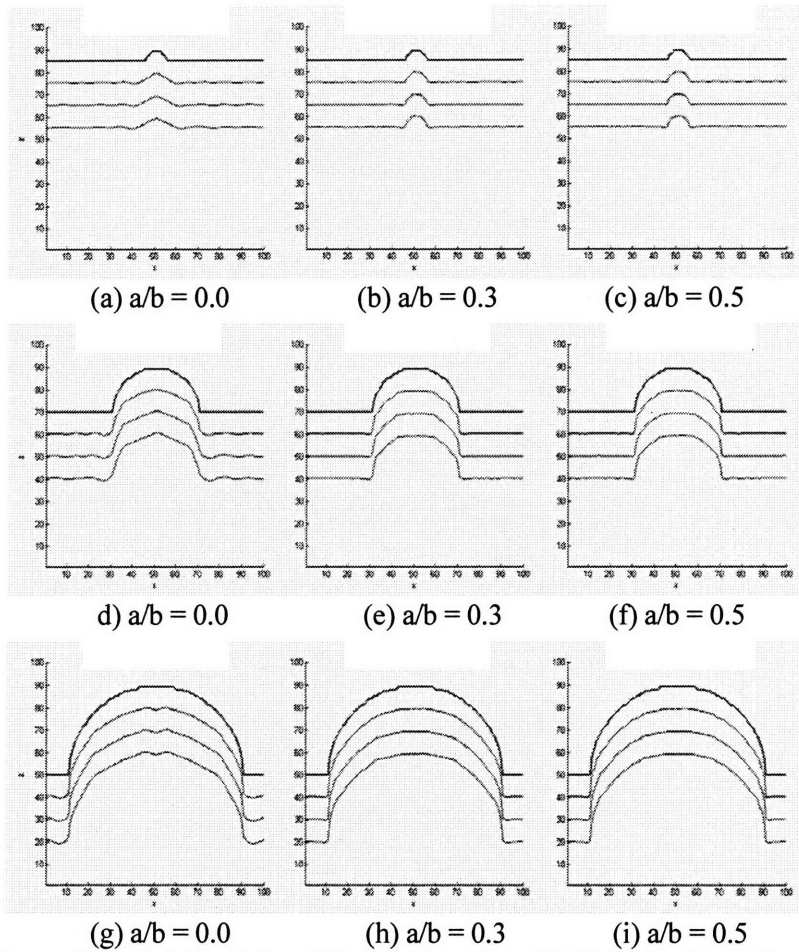
Figure 2.26: Direct etching of a half cylinder. Cylinder with a radius of 5, 20 and 40 cells (12.5 nm, 50 nm and 100 nm) were each etched using an a to b ratio of 0, 0.3 and 0.5. The features were distorted when the ratio was 0, but they were well retained for a to b ratios of 0.3 and 0.5.

Similarly, when particles were deposited onto a cylindrical surface using an a to b ratio of 0, its features became distorted regardless of its radius (Figure 2.27a, d, g). Some instability was also observed on the horizontal part of the feature. Even when a ratio of 0.3 or above was used, the features were not as well retained as in etching (Figure 2.27b, c, e, f, h, i) due to the smoothing caused by deposition, but the instability on the horizontal surfaces was not observed. Therefore, the best value for the ratio of a to b was still 0.3.
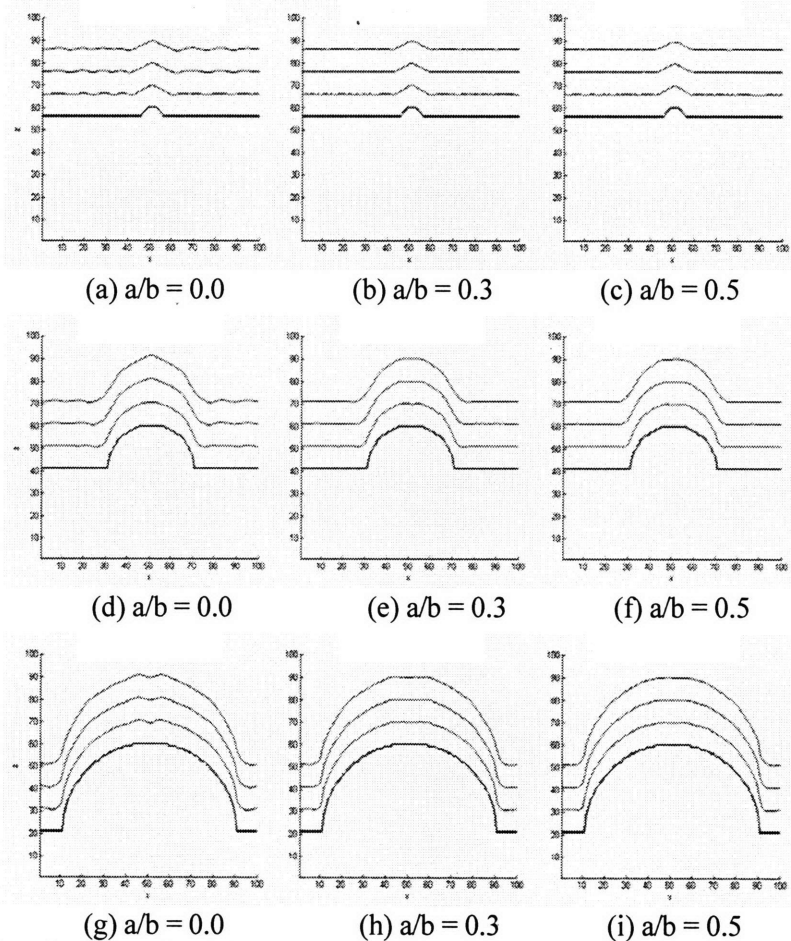
Figure 2.27: Direct deposition of particles on a half cylinder. Particles were deposited onto a half-cylinder with a radius of 5, 20 and 40 cells (12.5 nm, 50 nm and 100 nm) using a to b ratios of 0, 0.3 and 0.5. The features were distorted when the ratio was 0, but they were well retained for the ratios 0.3 and 0.5.

In addition to direct etching or deposition, the surface advancement algorithm was also tested for the case of isotropic etching or deposition, where each point on the surface advances equally in all directions. As shown in Figure 2.28, since the surface grows equally in all directions, the surface conformation may be predicted by drawing a series of circles with constant radii along the surface and connecting the edges. For the isotropic etching of the surface given in Figure 2.28a, the peaks remain sharp but the valleys or the bottom corners are rounded during the process. For isotropic deposition,

70

the valleys remain sharp, but the peaks are rounded as depicted in Figure 2.28b. This feature was used in the simulation, with an a to b ratio of 0.3 which was the optimal value obtained from considering the cases of direct etching and deposition. To model isotropic flux, particles were introduced from the top of the simulation domain with a cosine distribution, and the sticking probability of the particles was set to 1%. When the particles did not stick to the surface, they left the surface with a cosine distribution as well. The simulation results for isotropic etching and deposition are shown in Figure 2.29 (open circles). The theoretical surface advancement was also calculated and plotted alongside the simulated surface for comparison (Figure 2.29, blue lines). As shown in Figure 2.29, the simulated surface matches the theoretical surface well. In Figure 2.29b, particles are deposited slightly faster at the peak in the simulation compared to the theoretical surface. This difference may be due to the finite value for the sticking probability used in the simulation. To simulate a truly isotropic deposition, the sticking probability must be infinitely small so that each point on the surface receives equal flux. The higher the sticking probability is, the higher the chance for particles to stick to the top of the peak before reaching the lower part of the slope. Thus, the differences observed in the simulation may be caused by the stipulated sticking probability of 1%, which may not be small enough to enable exact matching to the theoretical surface.
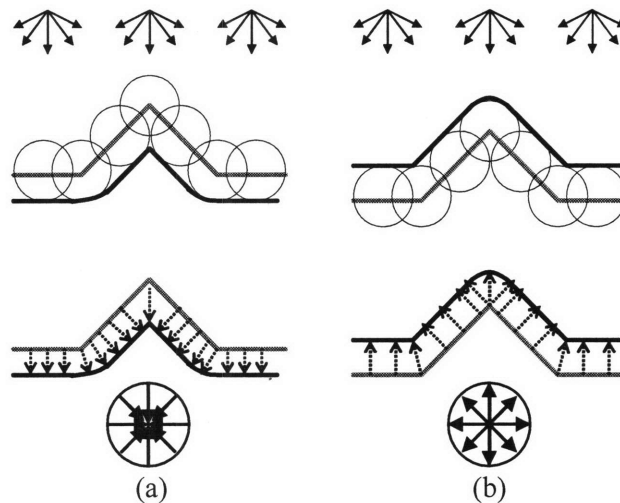
Figure 2.28: Theoretical surface advancement: Etching (a) and deposition (b) in an isotropic flux. The initial feature is shown in red. In theory, each point on the surface advances equally in every direction. Isotropic etching of the surface keeps the peaks sharp and makes the valleys rounded, whereas isotropic deposition makes the peaks round and keeps the valleys sharp.
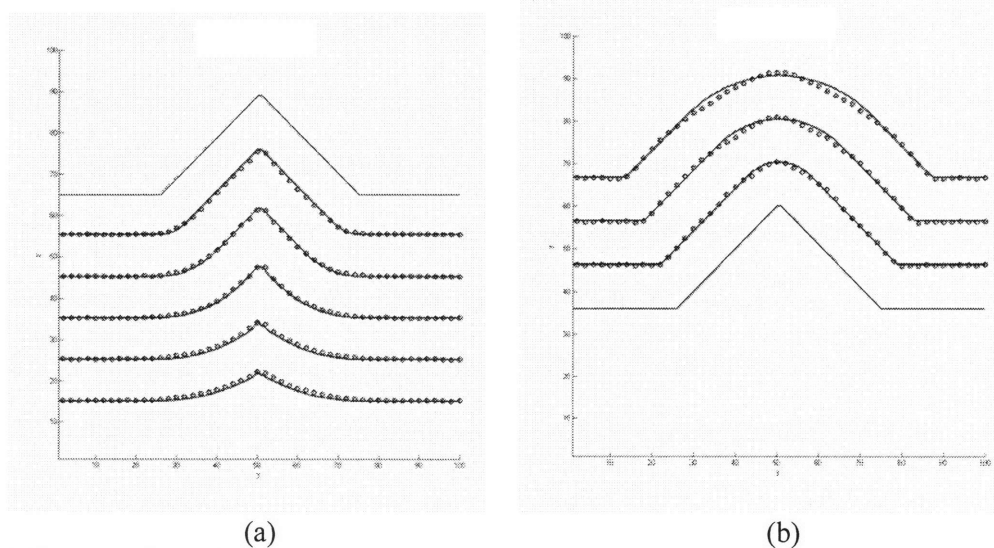
Figure 2.29: Isotropic etching (a) and deposition (b). Simulated surfaces are plotted with open circles, and theoretical surfaces are plotted with blue lines. Simulation matches the theory well in both etching and deposition. A value of 0.3 for the ratio of a to b was used in both cases.

The range of the polynomial fitting was chosen to be ±3 cells (7 7 7 cells), which allows the simulation to capture a minimum radius of curvature of about 3 cells, or 7.5 nm if each cell was assumed to be 2.5 nm in dimension. This assumption is sufficient

since the surface roughness of interest is greater than or of comparable dimensions, and the smoothing caused by surface diffusion is also at a similar length scale. While it is possible to use a smaller cell size and fit the surface over a larger range to capture a more detailed surface structure, the computational requirements would drastically increase and the efficiency of the simulation would consequently be greatly reduced. In order to check the effects of different cell sizes, a surface with a sinusoidal wave-like profile was etched with normal particle bombardment using two cell sizes: 2.5 nm and 1.25 nm (Figure 2.30). A second order polynomial was fitted to a 7 7 7 (±3 cells) and 13 13 13 (±6 cells) cell range for cell-sizes of 2.5 nm and 1.25 nm, respectively.
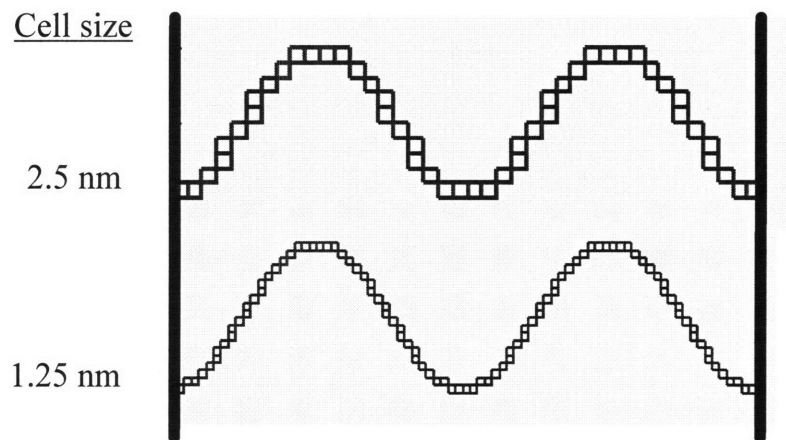
Figure 2.30: Cellular representation of sine wave with different cell size. The second order polynomial was fitted to 7 7 7 and 13 13 13 cell range for the case with cell size of 2.5 nm and 1.25 nm, respectively.

The simulation results for the direct etching of a sinusoidal wave surface using a 2.5 nm cell size are shown in Figure 2.31. The amplitude and wavelength of the initial sinusoidal surface were varied from 3 to 5 cells (7.5 to 12.5 nm) and 20 to 40 cells (25.0 nm to 50.0 nm), respectively. The results showed that although the peaks and valleys of the sinusoidal surfaces were slightly rounded due to polynomial fitting, their

corresponding amplitudes and wavelengths remained constant after continued etching with directional ion bombardment. The same surface profile represented by cells of smaller dimensions was also allowed to undergo the same etching conditions (Figure 2.32), and the results were not significantly different from the case using a larger cell size. We therefore conclude that a cell size of 2.5 nm is sufficient for surface representation.

(a)   (b)   (c)   (d)
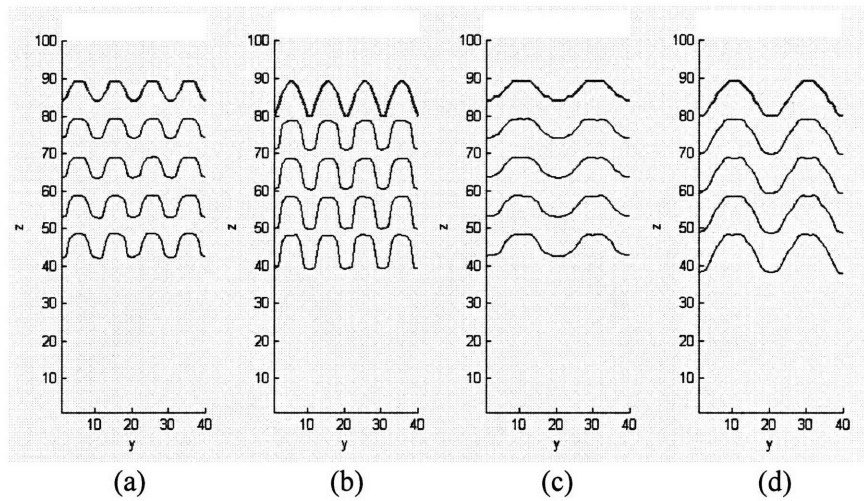
Figure 2.31: Direct etching of sinusoidal wave-like surface using 2.5 nm cell size. The polynomial was fitted to a ±3-cell range in the surface advancement algorithm. The amplitude (h) and wavelength (λ) of the initial sinusoidal wave structure was varied. (a) h = 3 cells (7.5 nm), λ = 10 cells (25.0 nm); (b) h = 5 cells (12.5 nm), λ = 10 cells (25.0 nm); (c) h = 3 cells (7.5 nm), λ = 20 cells (50.0 nm); (d) h = 5 cells (12.5 nm), λ = 20 cells (50.0 nm).
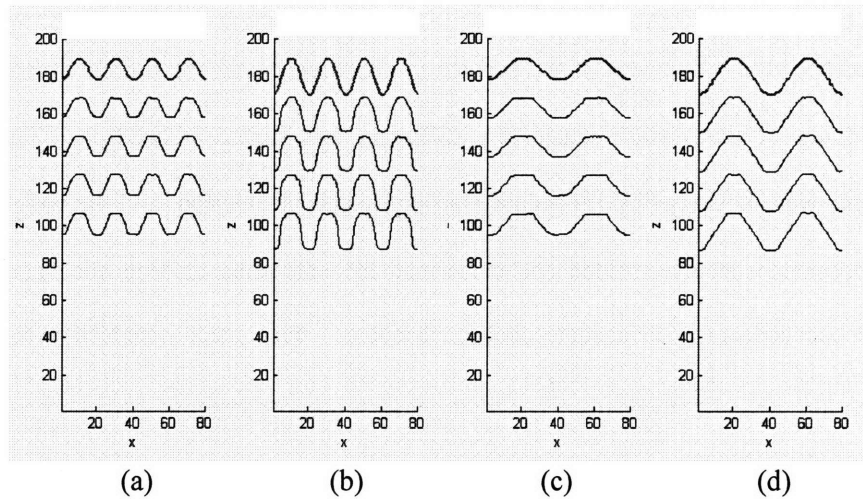
Figure 2.32: Direct etching of sinusoidal wave surface using 1.25 nm cell size. The polynomial was fitted to ±6-cell range in the surface advancement algorithm. The amplitude (h) and wavelength (λ) of the initial sinusoidal wave structure was varied. (a) h = 6 cells (7.5 nm), λ = 20 cells (25.0 nm); (b) h = 10 cells (12.5 nm), λ = 20 cells (25.0 nm); (c) h = 6 cells (7.5 nm), λ = 40 cells (50.0 nm); (d) h = 10 cells (12.5 nm), λ = 40 cells (50.0 nm).

2.7. Conclusion

A 3-D Monte Carlo simulator was developed to model the surface advancement in etching and deposition processes. The simulator employed a Monte Carlo algorithm to model mass transport and surface reaction kinetics and a cell-based representation for tracking surface compositions, allowing for the incorporation of both physical and chemical processes that occur in plasma etching. The local surface topography was simulated by fitting to a polynomial surface, from which the surface normal was computed. This departure from the more conventional cubic representation of the exposed surface avoids exaggerated shadowing that causes excessive flux to protruded cells, resulting in unrealistic surface profiles. In addition, the local surface curvatures can be determined accurately. The surface advancement algorithm in the simulator

75

considered both the movement of the surface in the direction of the surface normal and the smoothing of the surface caused by diffusion and surface relaxation. The two components were balanced by formulating an optimization function, and the weights on each component were determined and confirmed by simulating etching and deposition processes on various macroscopic surface features. The good match between our simulation and the corresponding theoretical surface conformation in each case verified that our surface advancement algorithm has a sufficient basis for incorporating further complex factors in the plasma etching process.

2.8. References

1. W. G. Oldham, S. N. Nandgaonkar, A. R. Neureuther and M. O'Toole, IEEE Transactions on Electron Devices 26, 717 (1979).
2. M. Tuda, K. Ono and K. Nishikawa, Journal of Vacuum Science and Technology B 14, 3291 (1996)
3. D. Adalsteinsson and J. A. Sethian, Journal of Computational Physics 120, 128 (1995).
4. E. Strasser and S. Selberherr, IEEE Transactions on Computer-Aided Design of Integrated Circuits and Systems 14, 1104 (1995).
5. A. Mahorowala and H. H. Sawin, Journal of Vacuum Science and Technology B 20, 1064 (2002).
6. E. W. Scheckler, N. N. Tam, A. K. Pfau and A. R. Neureuther, IEEE Transactions on Computer-Aided Design of Integrated Circuits and Systems 12, 1345 (1993).
7. M. Fujinaga, N. Kotani, T. Kunikiyo, H. Oda, M. Shirahata and Y. Akasaka, IEEE Transactions on Electron Devices 37, 2183 (1990).
8. D. Adalsteinsson and J. A. Sethian, Journal of Computational Physics 122, 348 (1995).
9. M. E. Barone and D. B. Graves, Journal of Applied Physics 78, 6604 (1996).
10. F. J. I. Ulacia, C. J. Petti and J. P. McVittie, Journal of Electrochemical Society 135, 1521 (1998).
11. E. W. Scheckler and A. R. Neureuther, IEEE Transactions on Computer-Aided Design 13, 219 (1994).
12. R. M. Bradley and J. M. E. Harper, Journal of Vacuum Science and Technology A 6, 2390 (1988).

13. S. A. Vitale, H. Chae and H. H. Sawin, Journal of Vacuum Science and Technology A **19**, 2197 (2001).
14. J. P. Chang and H. H. Sawin, Journal of Vacuum Science and Technology A **15**, 610 (1997).
15. H. A. Helmer and D. B. Graves, Journal of Vacuum Science and Technology A **16**, 3502 (1998).
16. O. Kwon and H. H. Sawin, Journal of Vacuum Science and Technology A **24**, 1914 (2006).
17. W. Guo, B. Bai and H. H. Sawin, unpublished.
18. N. Layadi, V. M. Donnelly and J. T. C. Lee, Journal of Applied Physics **81**, 6738 (1997).
19. D. Humbird and D. B. Graves, Journal of Applied Physics **96**, 65 (2004).
20. R. Ditchfield and E. G. Seebauer, Physical Review Letters **82**, 1185 (1999).
21. M. A. Makeev and A.-L. Barabasi, Applied Physics Letters **71**, 2800 (1997)

3. Surface Roughening in Physical Sputtering Process

3.1. Introduction

Ion sputtering has commonly been employed in surface analysis techniques such as secondary ion mass spectroscopy (SIMS), Auger electron microscopy (AES) and X-ray photoelectron spectroscopy (XPS)[1]. Other applications include ion polishing or milling, surface cleaning, micromachining and sputter deposition. It is known that sputtering of a surface greatly affects its morphology, and the effects of ion sputtering on surface morphology have been studied extensively during the last several decades in hopes of having a better control over the topology during the process. One of the commonly observed phenomena is the formation of periodic height modulations or ripples on the surface which are produced when ions bombard the surface at off-normal incidences[2,3]. This is unacceptable in many applications where the desired structures are in the nanometer scale and the imperfections are of comparable dimensions.

The formation of ripples in physical sputtering is generally not taken into account when studying the commonly observed surface roughness profiles in plasma etching processes. One reason is that in physical sputtering studies, the effects of gaseous chemical reactions and its corresponding surface kinetics are not considered, whereas in plasma etching they are regarded as important factors in the etch characterization. Moreover, most of the work done on physical sputtering were on metals with high ion energies (>1keV), which is not directly relevant to plasma etching. However, it is likely that a significant correlation exists between the roughening of a surface caused by physical sputtering and plasma etching, and it is useful to first study the former where the roughening is caused mainly by ion bombardment and does not involve other

complicated factors such as gas-phase chemical reactions that are present in plasma etch systems.

In this work, the 3-D Monte Carlo simulator whose development was detailed in Chapter 2 was used to simulate the sputtering of single-crystal silicon by argon ions, and the effects of various process parameters on surface roughening were explored. A fundamental theory of sputtering will first be discussed, followed by the description of the modeling of sputtering in the simulation. The roughening explored via simulation will be compared with some of the common trends in surface roughening experimentally observed in physical sputtering processes as described in the literature. This will form a good basis for understanding the effects of several process parameters on roughening that were explored via simulation.

3.2. Sigmund's theory of ion sputtering

The theory of sputtering was developed in the early 1970's by Sigmund, who proposed that the sputtering yield of ion-bombarded surfaces is proportional to the amount of energy deposited onto the surface[4]. According to the theory, kinetic energy is transferred during the cascades of collisions to the surface causing the random slowing-down of ions, and the energy is spread out according to the Gaussian distribution,

$$E(\mathbf{r}) = \frac{\varepsilon}{(2\pi)^{3/2}\sigma\mu^2} \exp\left\{-\frac{Z'^2}{2\sigma^2} - \frac{X'^2 + Y'^2}{2\mu^2}\right\} \qquad \text{(Eqn. 3.1)}$$

where E is the average energy deposited at point $\mathbf{r}$, ε is the ion energy, and σ and μ are the widths of the distribution parallel and perpendicular to the beam direction, respectively. See Figure 3.1[5]. X', Y' and Z' are the distances from the point on the surface where its atoms are sputtered (point O), relative to the point where the

79

bombarding ion comes to a stop in the bulk material after penetrating its surface (point P). More specifically, Z' is the distance from point P to point O measured along the beam direction, and X' and Y' are the distances measured in the axis perpendicular to it. The energy transferred decreases with distance from point P according to a Gaussian distribution, and some of this energy contributes to the erosion of the surface at point O. Therefore, the erosion of the surface at point O can be computed by integrating the amount of energy transferred by incident ions over the neighboring surface.
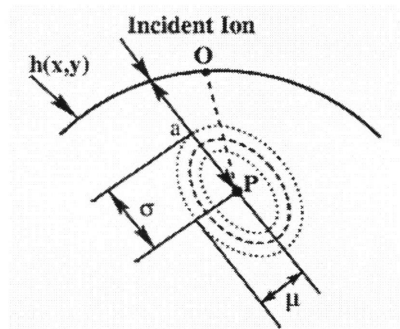
Figure 3.1: Distribution of the energy transferred by an incident ion. The incident ion penetrates the surface and stops at point P, where its energy is distributed according to a Gaussian distribution. This can be represented by contours which depict the relative intensities of energies distributed from the point of impact. Some of the energy transferred by this ion contributes to the erosion of the surface at point O (Ref. 5).

According to this theory, when a surface is bombarded by ions at off-normal incidences, the sputtering yield is highest not at the point of impact (point A) but at a distance slightly down the slope from it (point B), as shown in Figure 3.2. This is because the center of the deposited energy distribution is located at a certain distance from the point of impact along the direction of ion bombardment, and depending on the angle of ion incidence with respect to the surface, there may exist a point on the surface which is closer to the center of the energy distribution (i.e. on a higher contour) than the point of impact.
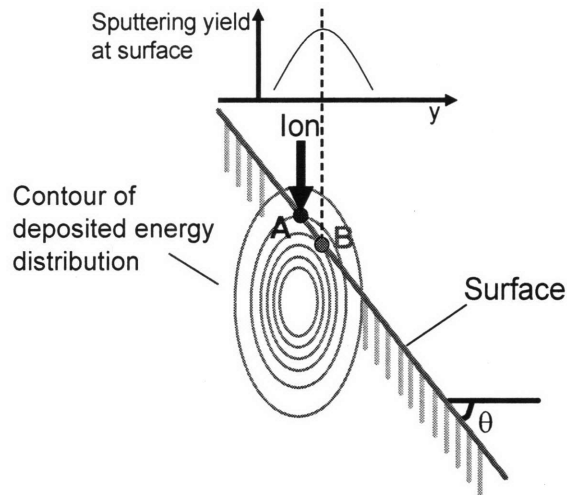
Figure 3.2: Distribution of energy transferred by an ion at off-normal incidence. The ion strikes the surface at point A with an off-normal incidence of θ. More effective sputtering occurs at point B instead of point A because point B is on a higher contour, and thus possesses more energy that is contributed towards surface erosion.

The theory also partially explains why the sputtering yield increases with off-normal ion incidence, which is a well-known observation in sputtering experiments. If it is assumed that the ions penetrate the same distance from the point of impact into the bulk material for all off-normal incidences, the centers of the deposited energy distribution are much closer to the interface when a surface is bombarded at higher off-normal incidence than at normal incidence and the sputtering of the surface is thus more effective at larger off-normal angles of bombardment (Figure 3.3).
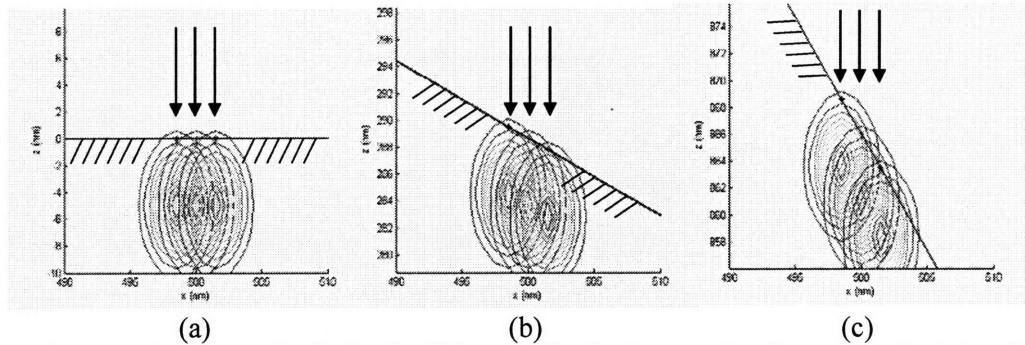
Figure 3.3: Deposited energy distribution for different ion bombardment angles. Ions are bombarded on the surface at 0° (a), 30° (b) and 60° (c) off-normal. The center of the energy distribution, where most energy is deposited, is closer to the interface for a higher off-normal angle of incidence than at normal incidence, and therefore the sputtering is more effective at higher off-normal angles of incidence.

This theory, however, ignores the fact that the collision cascades and energy distribution are significantly perturbed by the presence of an interface boundary. As shown in Figure 3.3c, when the surface is bombarded by ions at grazing incidence, a good number of contours lie partially outside of the target surface, which is unphysical because energy cannot be deposited where the surface is not present. As a result, the energy distribution near the surface may not have strict adherence to the initial assumption of a Gaussian profile. Thus, this theory is not valid for a very grazing ion angle of incidence (>75°) where a large portion of the contours (> $\frac{2}{3}$ of the maximum level) do not lie within a physical target. Despite the simplification made for approximating the spatial distribution of the deposited energy, Sigmund's theory has been widely used as a basis for the development of other models to explain many surface morphological effects in sputtering processes.

3.3. Bradley and Harper (BH) model of ripple formation

In the late 1980's, Bradley and Harper (BH) applied Sigmund's theory of sputtering to explain the dependence of the surface curvature on the local sputter yield[6]. He proposed that more energy is deposited onto a surface with a positive curvature than on a surface with a negative curvature, and this results in a high sputtering yield at the bottom of valleys than at the top of the hills on a given surface. The relative amounts of energy deposited at each point on the surface can be crudely compared by considering the distance from the center of the distribution of contours to the relevant point on the surface, as shown in Figure 3.4. When the surface is bombarded by ions at normal incidence, the center of the dissipated energy contour is closer to the point on the surface with positive curvature (point B) than on the surface with negative curvature (point A), and therefore the surface with the positive curvature is etched faster.
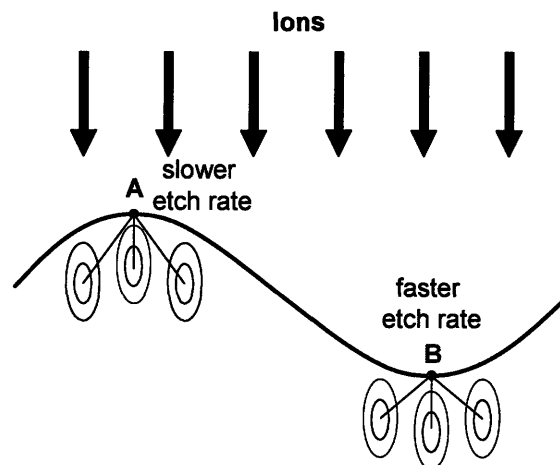
Figure 3.4: BH model of curvature-dependent etching. A surface with positive curvature (point B) is etched faster than a surface with negative curvature (point A) due to higher energy deposition at point B. The amount of energy deposited at each point (A and B) can be compared by considering the distance from the center of the energy distribution to the point on the surface.

This effect is enhanced when a surface is bombarded at off-normal ion incidence. As illustrated in Figure 3.5, when the ions strike the surface at off-normal angles of

incidence, most of the energy deposited on the surface is derived from the ions reaching the surface at upstream positions. By comparing the distances from the centers of energy distribution contours to their corresponding points on the surface, one can deduce that more energy is deposited at point B, where the surface has a positive curvature. The difference in the distances is more apparent for the case where the surface is bombarded at off-normal ion angles of incidence than for normal ion incidence, which results in an enhancement of the curvature dependence on sputtering yield. This will be discussed more quantitatively in the next section.
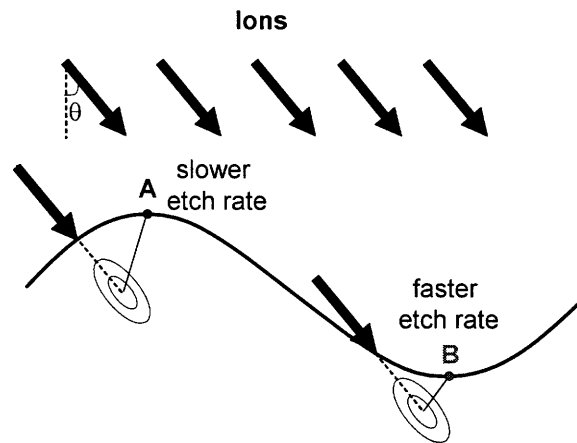
Figure 3.5: BH model of curvature-dependent etching at off-normal ion incidence. When the ions bombard the surface at off-normal incidence, most of the energy deposited at point A or B is contributed by the ions striking the surface at upstream positions. The amount of energy deposited at B is larger than at A because the distance from the center of energy distribution contour to the point on the surface is clearly smaller for point B than for point A.

Using the curvature dependence as a basis, BH modeled the instability of the surface morphology during off-normal ion bombardment which leads to ripple formation observed experimentally in many studies. He incorporated the effect of thermally-activated surface self-diffusion in order to explain the formation of these ripples. The common experimentally observed surface profile scenarios in the physical sputtering of metallic and amorphous surfaces are shown schematically in Figure 3.6. When the

surface is bombarded at normal ion incidence, the surface remains relatively smooth, bearing some roughness with no preferred orientations (Figure 3.6a). When the surface is bombarded at off-normal incidence, the surface is roughened, forming ripples that are perpendicular (transverse) to the direction of the beam source (Figure 3.6b). When the surface is bombarded at grazing incidence, however, the waves formed are parallel to the direction of the ion beam (Figure 3.6c). These transition angles vary with the process conditions and material composition of the surface. The BH model is not applicable when the ion beam is directed at very grazing angles to the surface because it ignores the scattering of ions which becomes very significant at large deviations from normal incidence. Other physical effects ignored in the model are the re-deposition of materials and shadowing of certain areas by other features on the surface. These effects may become more important as the surface is further roughened. Furthermore, the only smoothing mechanism incorporated into the model is thermal diffusion, which is more applicable at high temperature conditions. Although the thermal spike caused by energetic ion bombardment may also induce thermal diffusion at low temperature conditions, the diffusivity is lower and it is therefore not as applicable at low temperature conditions where surface smoothing is mostly induced by ion bombardment. Nonetheless, the BH model is one of the first major efforts in explaining the mechanisms of the instability of the surface due to ion bombardment, and its methodology has since been extended by numerous researchers[7,8].
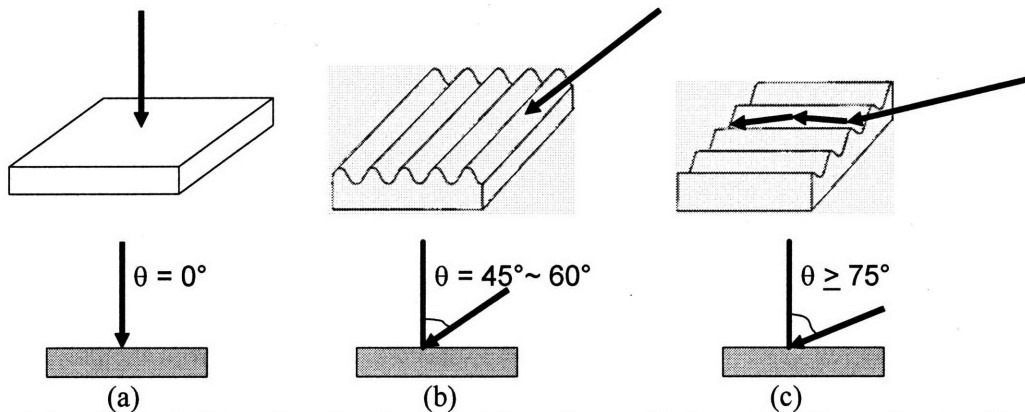
Figure 3.6: Schematic illustration of surface morphology change with increasing off-normal angle of ion incidence. When the surface is bombarded by ions at normal incidence (a), the surface remains relatively smooth, bearing some roughness without any preferred orientation. When the surface is bombarded at off-normal angles of incidence of less than 60° (b), ripples perpendicular to the source beam direction are formed. When the surface is bombarded by ions at grazing angles of incidence, wave-like structures that are aligned with the direction of the source beam are formed.

3.4. Incorporation of curvature-dependent sputtering yield into 3-D MC simulator

Since the local surface conformation was approximated by fitting a polynomial surface in our 3-D Monte Carlo simulator, it was relatively straightforward to determine the local surface curvature and account for the curvature dependence of sputtering yield. In this section, the computation of local surface curvature is discussed and its effects on sputtering yield are explored within the BH model. While the BH model specifies how the sputtering yield varies with the local surface curvature, its limitations, as mentioned in the previous section, likely make it inexact in many cases. Thus, the model was used only to extract qualitative trends in the sputtering yield as a function of local surface curvature. To further simplify the model, shadowing effect was not considered in the determination of the dependence of the sputtering yield on surface curvature.

86

3.4.1. Local surface curvature

By definition, curvature is a measure of how much the geometric object deviates from being flat. Mathematically, the magnitude of curvature for a 2-dimensional curve given by $z = f(x)$ can be determined from the second derivative of z, $\dfrac{d^2z}{dx^2}$. It is relatively easy to determine a curvature in 2-D, where there is only one value for the curvature. In 3-D, however, both the direction as well as the magnitude of the bend must be considered. In our model, the surface is represented by a locally fitted second-order polynomial surface,

$$z = f(x, y) = b_1 x^2 + b_2 y^2 + b_3 xy + b_4 x + b_5 y + b_6 \qquad \text{(Eq. 3.2)}$$

where surface height z is a function of both x and y. For example, for the surface given in cellular representation in Figure 3.7a, its fitted polynomial has a negative surface curvature, as shown in Figure 3.7b. The curve resulting from the intersection of a given plane and the fitted surface determines the curvature along the plane. The intersection of the fitted surface and the xz-plane (y = 0) and yz-plane (x = 0) are shown in red in Figure 3.7c and d, respectively.
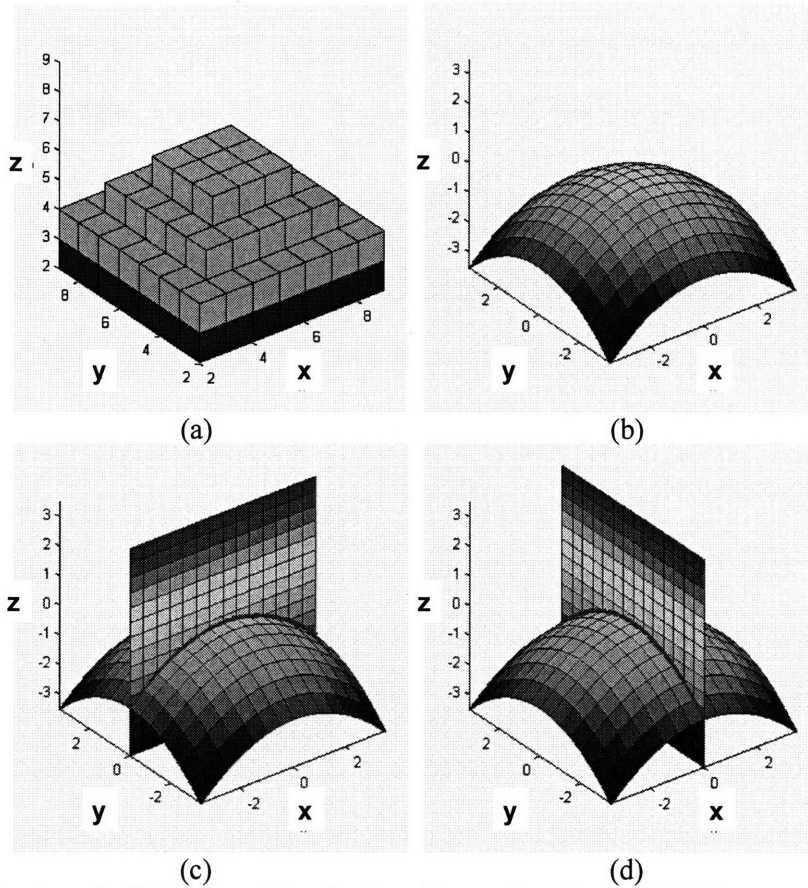
Figure 3.7: Curvature of a fitted polynomial surface in xz-plane and yz-plane. (a) Cellular representation of a surface. Surface cells and non-surface cells are shown in cyan and blue, respectively. (b) 2nd order polynomial surface fitted to the surface cells in (a). (c) Intersection of the fitted surface and the xz-plane at y = 0. (d) Intersection of the fitted surface and the yz-plane at x = 0. These intersections determine the curvature along each plane.

These intersection curves determine the curvature along the xz-plane and yz-plane at the center of the surface. Their corresponding equations are given by

$$z_x = f(x,0) = b_1 x^2 + b_4 x + b_6$$
$$z_y = f(0,y) = b_2 y^2 + b_5 y + b_6$$

(Eq. 3.3)

The magnitude of the surface curvature in the xz-plane and yz-plane (i.e. second derivative) can therefore be determined from the second-order coefficients b_1 and b_2. In

88

the following section, it will be discussed how the curvature in only one direction is important to the overall curvature dependence of the sputtering yield.

3.4.2. The effect of surface curvature in different directions on energy deposition

It is known from Sigmund's theory and the BH model that the sputtering yield is proportional to the energy transferred to the surface bombarded by ions. As mentioned earlier, the purpose of this section is to determine the qualitative trends in the curvature dependence on sputtering yield rather than quantify its exact dependence, and the amount of energy deposited on the surface, instead of the sputtering yield, was used to determine those trends. In Figure 3.5, it was shown schematically in 2-D that the amount of energy deposited by an off-normal incidence of ions varies depending on the local surface curvature along the beam direction (i.e. the surface normals are in the same plane with the ion trajectory). To verify this dependence in 3-D, the energy deposition to parabolic surfaces with different radii of curvature were computed. Figure 3.8 shows the parabolic surfaces varied from negative to positive curvature with ion trajectories perpendicular to the axis of curvature.

| (a) | (b) | (c) | (d) | (e) |
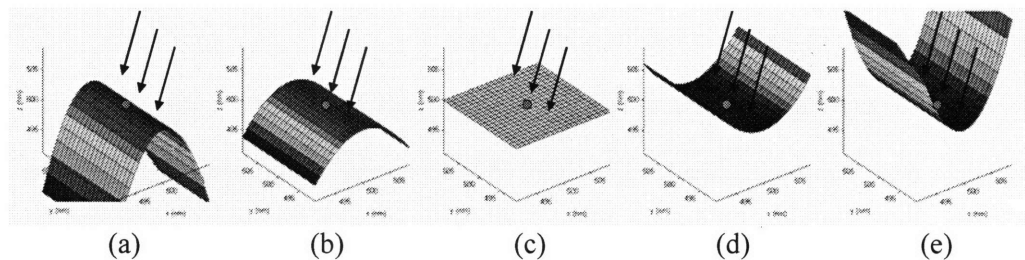
Figure 3.8: Parabolic surfaces with curvature along the beam direction. Curvature (κ) along the beam direction is varied: (a) κ = -0.40 nm-1, R = 2.50 nm; (b) κ = -0.16 nm-1, R = 6.25 nm; (c) κ = 0 nm-1; (d) κ = 0.16 nm-1, R = 6.25 nm; (e) κ = 0.40 nm-1, R = 2.50 nm.

89

The sputtering which occurs at the center point (illustrated by the red point in Figure 3.8) is caused by the energy transferred by ions striking the surface near this point. The amount of energy contributed to the sputtering that occurs at this point was approximated by a Gaussian distribution for the energy transferred by each ion. It was assumed that the penetration depth of the transferred energy was equivalent to the penetration depth of the ion (~2.5 nm, which is equivalent to the mixing length for ~500eV ions), and a surface of 18 nm by 18 nm was allowed to be bombarded by ions with a fluence of about 8×10^{14} ions/cm^2 (i.e. one ion per 0.12 nm^2). The widths of the Gaussian distribution parallel and perpendicular to the beam direction (σ and μ in Equation 3.1) were assumed to be a/2 and a/4, respectively, where a is the penetration depth of energy (2.5 nm) as shown in Figure 3.1[9]. The energy contributed to the sputtering of the center point by ions striking at each point on the 18 x 18nm^2 surface is plotted in Figure 3.9. While the increase in deposited energy with increasing curvature is not very noticeable for 0° and 30° off-normal angles of incidence, the amount of deposited energy increases significantly with increasing curvature for 45° and 60° off-normal angles of incidence, especially in cases where the curvature is positive. Note that the peak of the deposited energy shifts slightly upstream, implying that a large fraction of the energy is contributed by ions striking the upstream part of the surface, which is consistent with Sigmund's theory. The cases with off-normal angles of incidence greater than 60° were not considered because effects due to the scattering of ions and shadowing of surfaces become significant at grazing angles, and these were not included in the calculation of the energy deposition.

The total energy contributed to the center point as a function of surface curvature

is plotted in Figure 3.10. Since the sputtering yield is proportional to the amount of

energy deposited, the increase in deposited energy with increasing curvature suggests that

the sputtering yield also increases with increasing curvature. It should be reiterated that

the exact sputtering yield as a function of surface curvature was not computed due to

limitations in the BH model and the consequent purpose of this section was to determine

qualitatively how the energy deposition (and thus the sputtering yield) varies with surface

curvature.
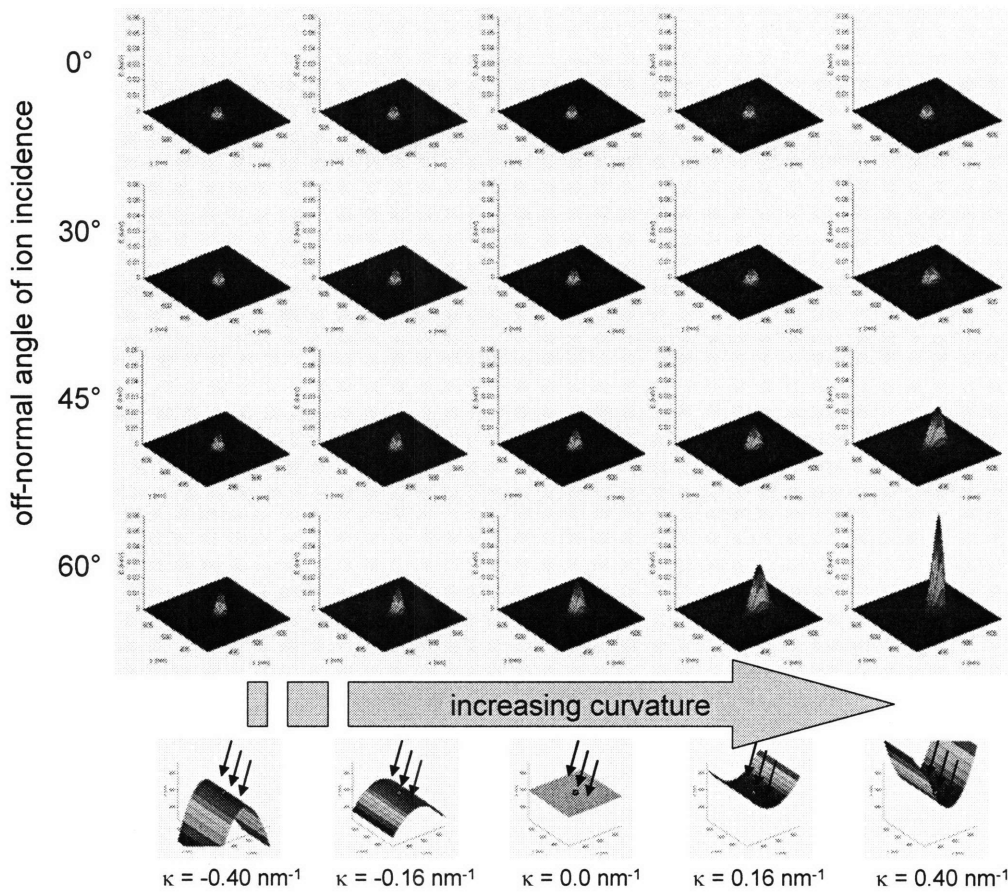
Figure 3.9: Energy transferred by ions bombarding the surface over 18x18nm2. The off-normal angle of incidence was varied from 0° to 60°, and the curvature κ was varied from -0.40 nm-1 to 0.40 nm-1. For 0° and 30° off-normal angles of incidence, the amount of deposited energy does not change drastically, but for 45° and 60° off-normal angles of incidence, the amount of deposited energy increases significantly with increasing curvature. The peak of the deposited energy shifts towards the upstream position of the surface, implying that most of the energy is contributed by ions striking the surface at upstream positions.
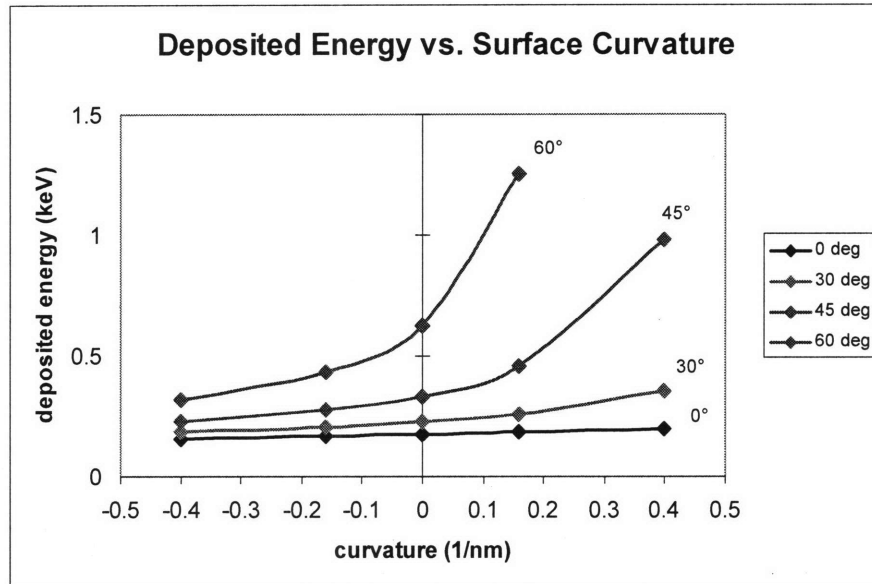
Figure 3.10: Deposited energy as a function of surface curvature along the ion beam direction. For all off-normal angles of incidence, the amount of deposited energy increases with increasing curvature. The magnitude of the increase is larger for higher off-normal angles. The deposited energy for a 60° off-normal angle of incidence onto a surface with high curvature (0.40 nm-1) is not considered because the value would be exaggerated as a result of ignoring the effects from shadowing.

How do curvatures in other directions affect the energy deposition? In order to answer this question, deposited energy was computed for a surface with curvature parallel to the direction of the ion beam (i.e. the surface normals are in the plane perpendicular to the ion trajectory), as shown in Figure 3.11. The energy transferred by ions bombarding the surface over an area of 18x18 nm^2 is plotted in Figure 3.12, and the total energy deposited as a function of surface curvature is plotted in Figure 3.13. As shown in Figures 3.12 and 3.13, the amount of deposited energy does not increase significantly with increasing curvature. Therefore, the curvature perpendicular to the beam direction does not have a significant effect on sputtering yield.
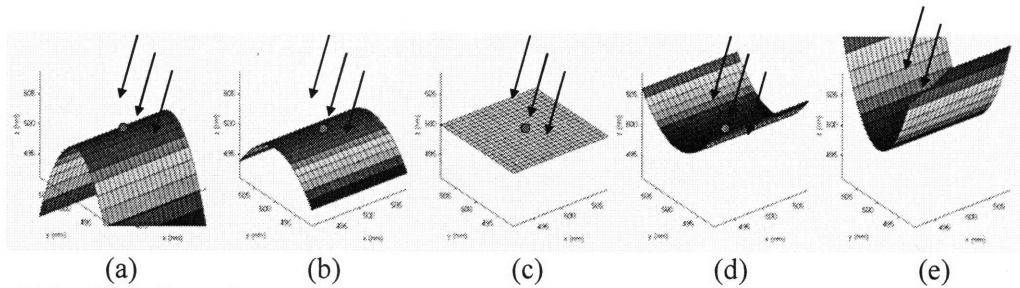
Figure 3.11: Parabolic surfaces with curvature perpendicular to the beam direction. Curvature (κ) perpendicular to the beam direction is varied: (a) κ = -0.40 nm-1, R = 2.50 nm; (b) κ = -0.16 nm-1, R = 6.25 nm; (c) κ = 0 nm-1; (d) κ = 0.16 nm-1, R = 6.25 nm; (e) κ = 0.40 nm-1, R = 2.50 nm
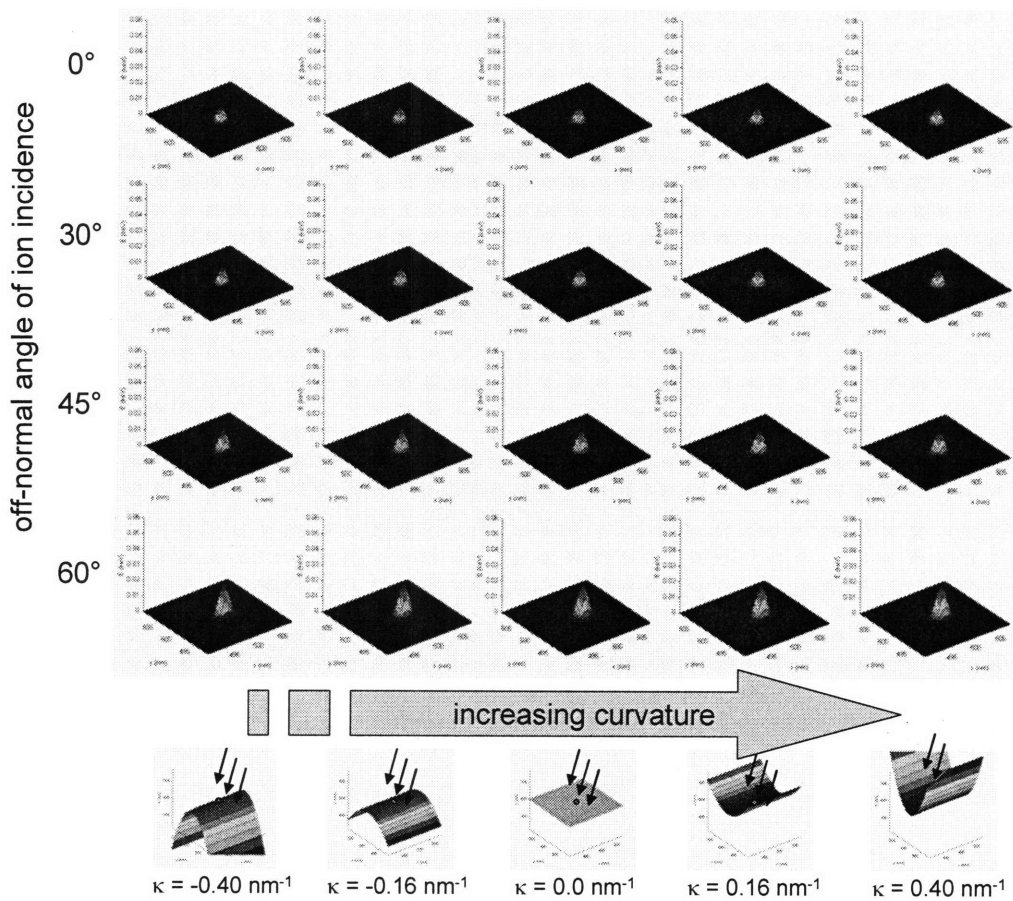
Figure 3.12: Energy transferred by ions bombarding the surface over 18x18nm2. The off-normal angle of incidence was varied from 0° to 60°, and the curvature κ was varied from -0.40 nm-1 to 0.40 nm-1. For all off-normal angles, there was no significant increase in energy deposition with increasing curvature. It is therefore concluded that the curvature perpendicular to the beam direction does not have any significant effect on sputtering yield at the center point (red circle).
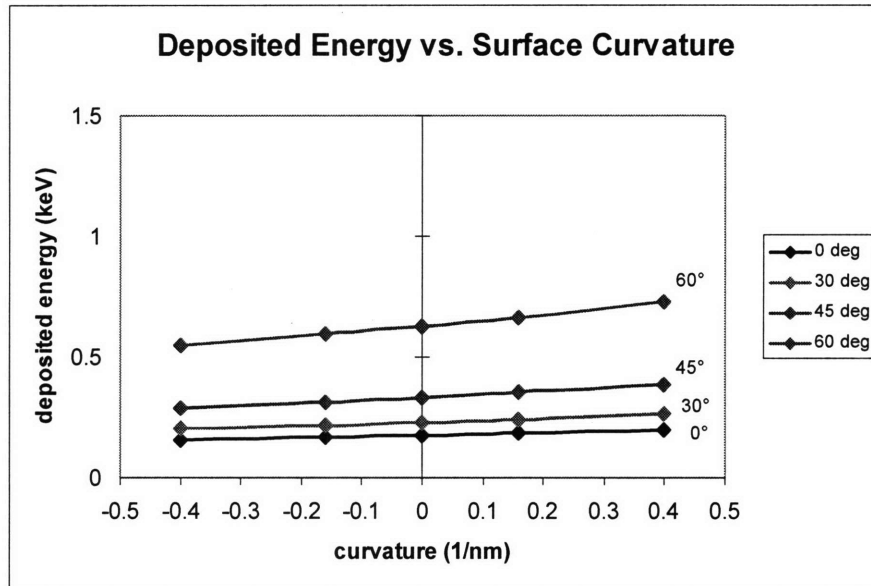
Figure 3.13: Energy deposited as a function of surface curvature perpendicular to the direction of the ion beam. For all off-normal angles of incidence, the energy deposited increases by a small amount with increasing curvature, but the increase is not as significant compared to the increase observed in the case with surface curvature along the ion beam direction (Figure 3.10).

To further verify the significance of surface curvature along the direction of the ion beam over curvature in other directions, the amount of energy deposited was determined for a surface with curvature that was both parallel (along) and perpendicular to the direction of the beam (Figure 3.14). As before, the energy transferred by ions bombarding a surface over an area of 18x18 nm^2 was computed for different off-normal angles of incidence and plotted in Figure 3.15. The trend observed was very similar to the case with surface curvature parallel to the beam direction (Figure 3.9), where the amount of energy deposited increases with increasing curvature at 45° and 60° off-normal incidence. The total deposited energy as a function of the surface whose curvature was both parallel and orthogonal to the direction of the beam is plotted in Figure 3.16 (dashed lines). The results for the previous cases (curvature parallel to the beam direction) are also plotted (solid lines) for comparison. There is no significant

95

deviation between the two plots, implying that the presence of curvature perpendicular to the beam direction has a very weak effect on energy deposition. Therefore, only the curvature along the beam direction was considered when incorporating the curvature dependence of the sputtering yield in our simulation.

(a)	(b)	(c)	(d)	(e)
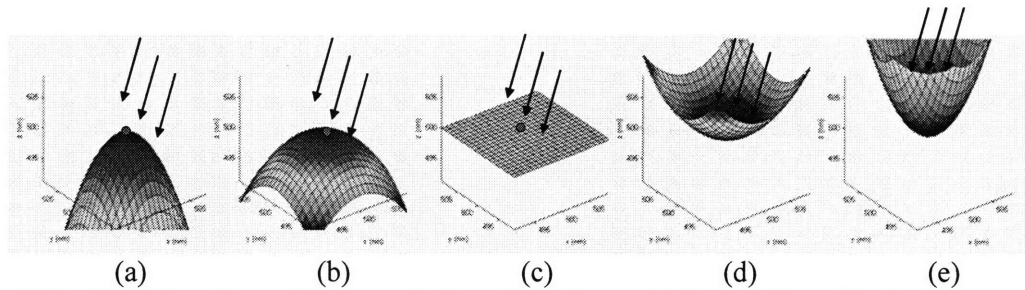
Figure 3.14: Parabolic surfaces with curvature both parallel and perpendicular to the beam direction. Curvature (κ) along the beam direction is varied: (a) $\kappa 1 = \kappa 2 = -0.40$ nm-1, R1 = R2 = 2.50 nm; (b) $\kappa 1 = \kappa 2 = -0.16$ nm-1, R1 = R2 = 6.25 nm; (c) $\kappa 1 = \kappa 2 = 0$ nm-1; (d) $\kappa 1 = \kappa 2 = 0.16$ nm-1, R1 = R2 = 6.25 nm; (e) $\kappa 1 = \kappa 2 = 0.40$ nm-1, R1 = R2 = 2.50 nm.
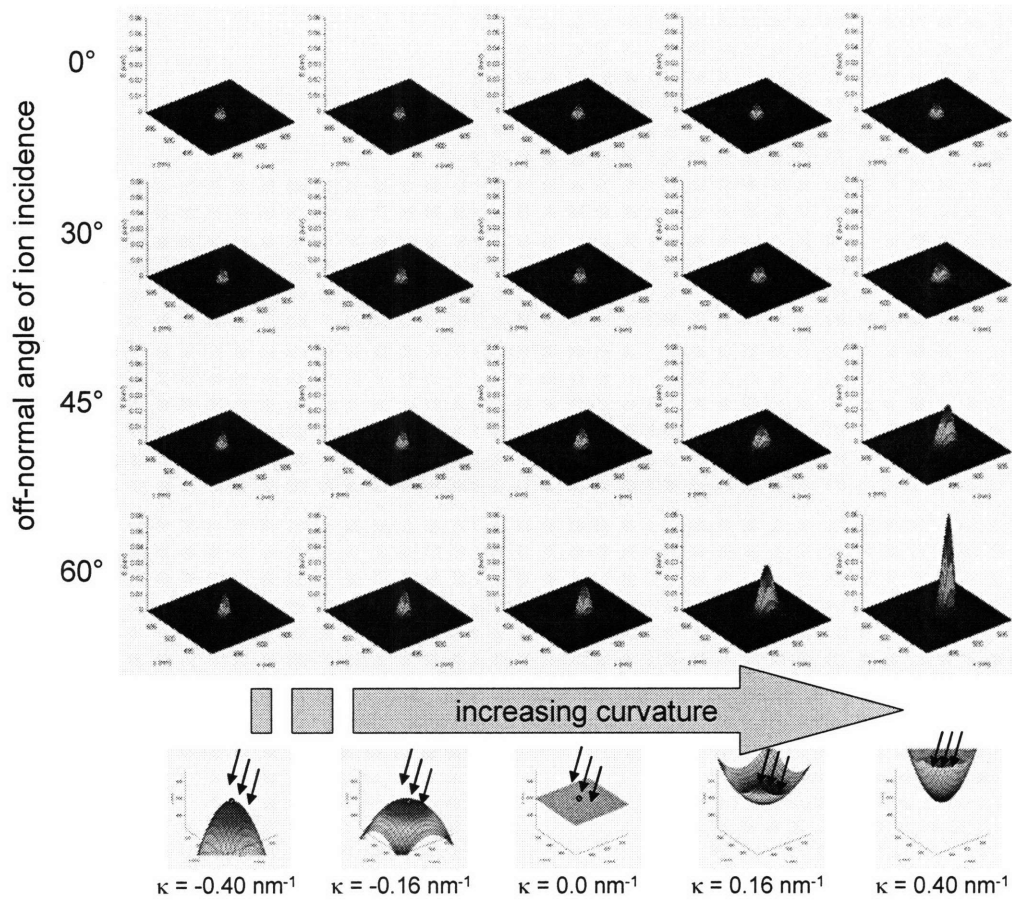
Figure 3.15: Energy transferred by ions bombarding the surface over 18x18nm2. The off-normal angle of incidence was varied from 0° to 60°, and the curvature κ was varied from -0.40 nm-1 to 0.40 nm-1 for curvatures both parallel and perpendicular to the beam direction. For all off-normal angles of incidence, there is no significant increase in energy deposition with increasing curvature. The trend observed is similar to the case with surface curvature only along the beam direction, in which the deposited energy was found to increase with increasing curvature.
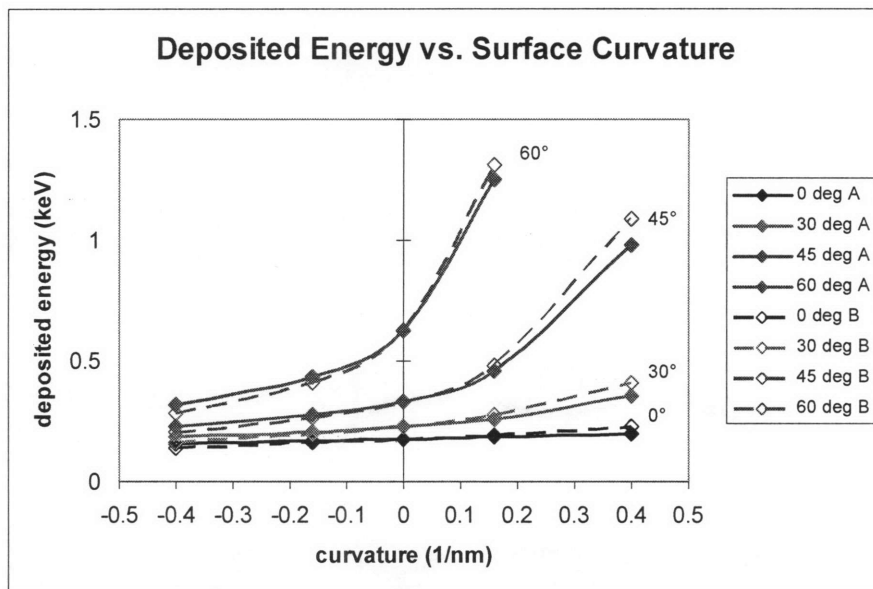
Figure 3.16: Deposited energy as a function of surface curvature. A: surface curvature is parallel to the ion beam direction (solid lines). B: surface curvature is both parallel and perpendicular to the ion beam direction (dashed lines). For each off-normal angle of incidence, there is no significant deviation, which implies that the surface curvature perpendicular to the beam direction has a very weak contribution to the overall energy deposition.

3.4.3. Combining the angular and curvature dependences of the sputtering yield

From the previous section, we know that the sputtering yield is a function of local surface curvature. However, at grazing angles of ion incidence, it is known that the ions have a high probability of scattering, which is not taken into account in the BH model. The high ion scattering probability at grazing angles of incidence is apparent from the drop in sputtering yield at high off-normal ion incidence. The sputtering yield as a function of off-normal ion incidence has been measured experimentally in a number of studies[10,11], and a typical angular dependence of the sputtering yield is illustrated in Figure 3.17. The increase in sputtering yield with the angle of off-normal ion bombardment is consistent with Sigmund's theory of sputtering which was shown schematically in Figure 3.3, but the sharp drop in etching yield at high off-normal angles of incidence cannot be explained using the same theory.
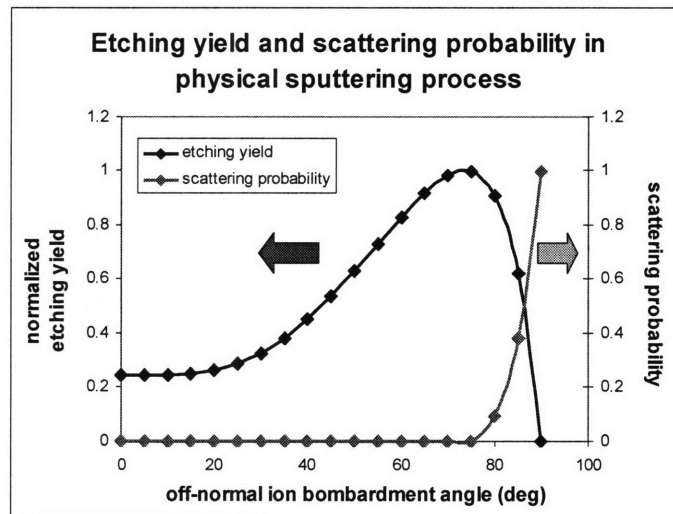
Figure 3.17: Angular dependences of etching yield and scattering probability in a physical sputtering process. The etching yield peaks at about a 75° off-normal incidence, and the scattering probability increases for off-normal angles above 75°.

In order to incorporate this drop in etching yield at high off-normal angles of ion bombardment, the angular and curvature dependence must simultaneously be accounted for in order to determine the final sputtering yield. However, we cannot combine the curvature dependence obtained from the BH model with an experimentally derived expression for angular dependence because the BH model intrinsically includes angular dependence. We thus proposed a set of predictive curves for etching yield versus curvature that comprises of multiplying the etching yield as a function of curvature as derived from the standard BH model with its corresponding experimentally observed values of etching yield as a function of ion angle of incidence (Figure 3.18). The qualitative trends in the final sputtering yield as a function of surface curvature are consistent with those determined from the BH model, as shown in Figure 3.19. Note that at very grazing angles (85° off-normal), the etch yield is lower than the yield for smaller angles of incidence for the entire range of curvatures, which is consistent with the fact that the ions at such angles have a higher scattering probability and result in less etching. Thus, the model is now qualitatively valid for the entire range of incidence angles at any local curvature. This model was subsequently used in the simulation of the sputtering of a silicon surface with argon ions, which will be discussed in the next section.
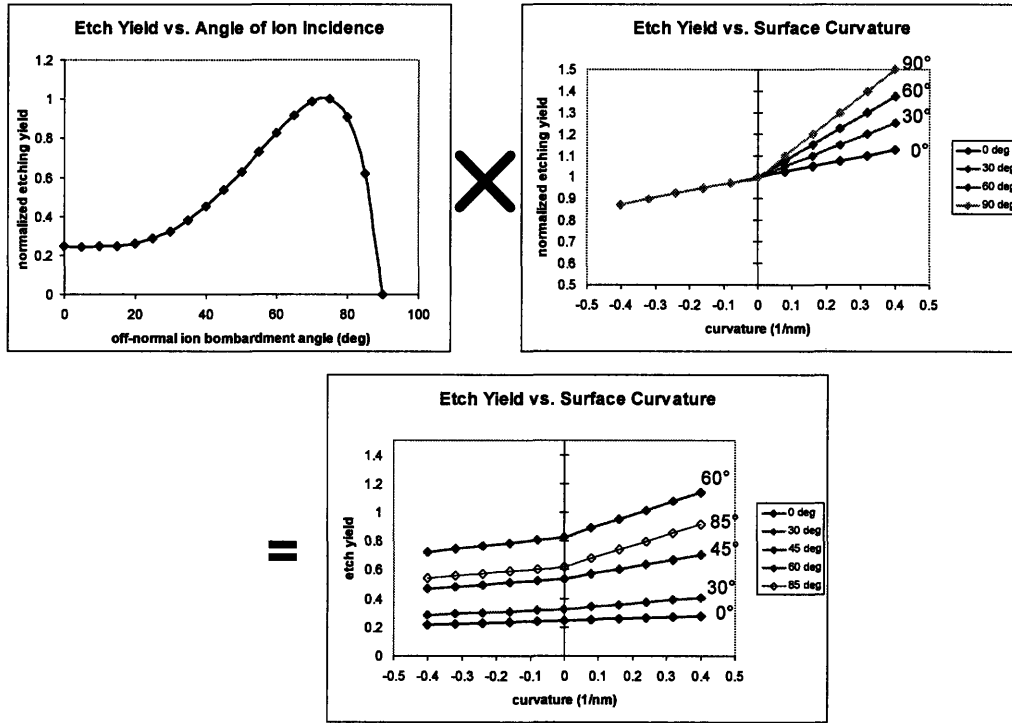
Figure 3.18: Angular dependence combined with curvature dependence determines the final sputtering yield. Both dependences must be considered to accurately model the sputtering process.

(a)   (b)
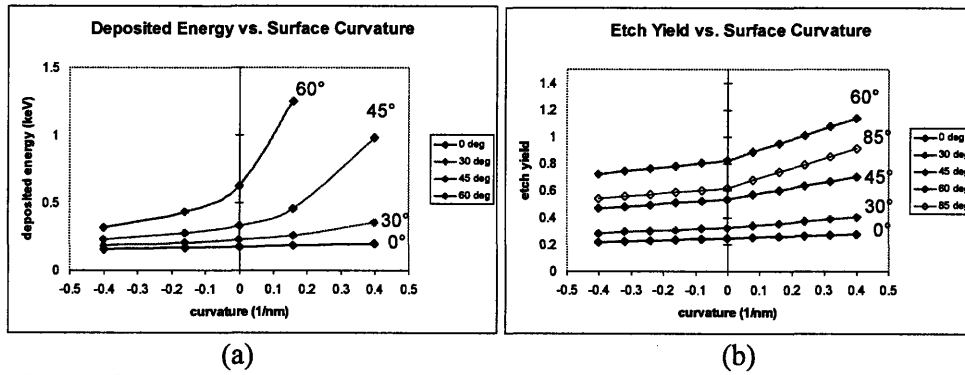
Figure 3.19: The final sputtering yield is consistent with the trends observed from the BH model. The amount of increase in etch yield with curvature is larger for high off-normal angles of incidence.

101

3.5. Simulation of sputtering of Si surface by Ar^{+} ion bombardment

The simulator was used to explore roughening in the physical sputtering of a silicon surface by argon ions. The yields for the sputtering of a silicon surface with argon ions were assumed to follow those determined from the angular and local curvature dependences as shown in Figure 3.19, and the energy of the argon (Ar^{+}) ions was kept constant at about 250 eV. The surface was bombarded at different off-normal angles of incidence to examine its effects on the surface morphology. The general trends obtained from studying surface morphological changes as a function of the angle of ion incidence will be discussed, followed by a comparison of the simulation results with some of the experimentally observed trends in physical sputtering processes. Subsequently, the effects of different factors on surface roughening will be explored, in particular the angular dependence of the etching yield curve for the material, the angular distribution of ions upon scattering off the surface, the non-uniformity of the film density, the initial roughness of the surface, and the re-deposition of sputtered materials.

3.5.1. Surface morphology after sputtering at different off-normal ion angles of incidence

A silicon surface was allowed to undergo sputtering by Ar^{+} ions at various off-normal ion angles of bombardment in the simulation. In this case the angular distribution of scattered ions was not considered, in other words the ions scattered at perfectly specular angles. The contour of the surface was plotted after etching to a depth of 100 nm, 200 nm, 400 nm, 600 nm and 800 nm, for an area domain of 250 x 250 nm^2 (Figure 3.20). The vertical scale is ±35 nm. The projected ion beam direction is shown by the

arrows to the right of the figure. The root mean square (RMS) roughness is also plotted against the depth of the surface etched for each off-normal angle of incidence as a means of monitoring the progression of surface roughening (Figure 3.21).

The contour surface plots show a very different morphology for each off-normal angle of ion incidence. From Figure 3.20, it is seen that at normal incidence (0° off-normal), the surface is smooth at the beginning, but is roughened after etching more than 200 nm with no preferred orientation. The RMS roughness remains constant at 8 nm, and further etching does not change this value significantly. At 45° off-normal incidence, wave-like patterns that are transverse to the ion beam direction (i.e. their effective wave vector is parallel to that of the ion beam) appear at an early stage of etching. The average wavelength of these wave-like patterns after etching to a depth of 200 nm is about 50 nm, with an amplitude of about 4 nm. As the surface is etched longer, both the wavelength and amplitude of the transverse waves are increased. The average wavelengths after etching to a depth of 400 nm, 600 nm and 800 nm are 50 nm, 80 nm, and 100 nm, respectively. Their corresponding approximated amplitudes (peak to valley) are 15 nm, 30 nm and 50 nm. The increase in roughness with etch progression is also evident from the RMS plot. At 60° off-normal incidence, the surface remains smooth and independent of the amount etched. The surface is isotropic with no preferred orientation and its RMS roughness remains constant at about 2 nm. At 75° off-normal incidence, the surface is again preferentially roughened, but the roughening pattern is different from the case of 45° off-normal incidence. After etching about 100 nm, short, disconnected waves that are transverse to the ion beam direction are evident, but as the surface is etched longer, the structures become gradually extended in the direction parallel to the ion beam. The

103

wavelength (peak to peak distance perpendicular to the beam direction) and the amplitude of each structure increases slowly with the amount etched. The average wavelengths after etching 200 nm and 800 nm are 50 nm and 80 nm, respectively. The amplitude also increases from 8 nm to 30 nm. The increase in amplitude is also evident from the increase in the RMS roughness shown in Figure 3.21. At 85° off-normal incidence, streaks parallel to the ion beam direction appear at an early stage of etching, and the streaks are elongated rapidly as the etching progresses. New streaks continually appear on the surface during etching, resulting in rows of streaks aligned with the direction of the ion beam. The average wavelength (peak to peak distance perpendicular to the beam direction) and amplitude after etching 800 nm are 80 nm and 20 nm, respectively. The RMS roughness increases rapidly at the beginning, but remains constant thereafter at about 13 nm after reaching an etch depth of 300 nm, implying that the amplitude does not change significantly with etching. It is also interesting to note that for the surface structures that result from the etching process, the edge of protrusion facing the direction of the incident ion beam is steep while the other side of the structure is a downhill slope with a gentle gradient that is close to the angle of ion incidence.
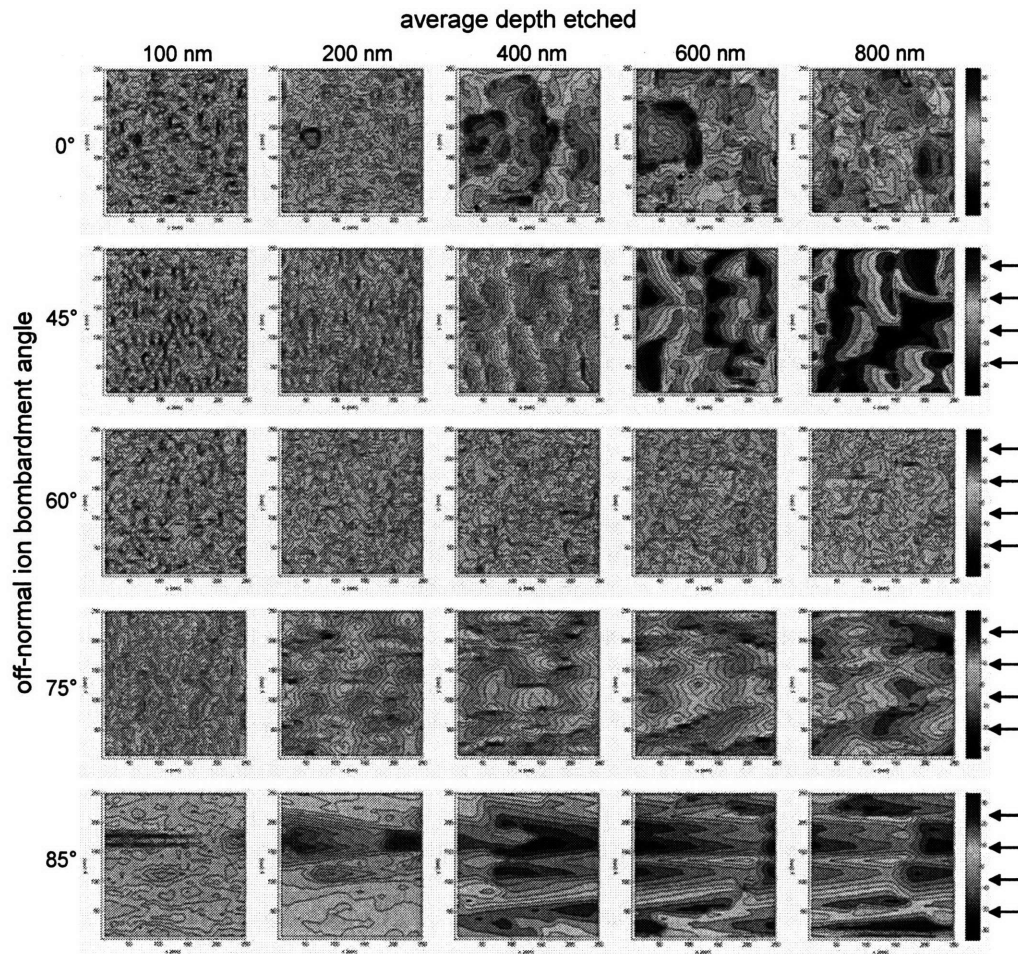
Figure 3.20: The progression of surface etched at different off-normal ion incidence angles. The vertical scale is ±35 nm, and the arrows give the ion beam direction. (1) 0° (normal) incidence: Surface is roughened randomly, with no preferential orientation. (2) 45° off-normal incidence: The ripples formed on the surface are perpendicular to the beam direction. (3) 60° off-normal incidence: Surface remained smooth independent of the amount etched. (4) 75° off-normal incidence: The small hills on the surface became more aligned with the beam direction as the etching proceeded. (5) 85° off-normal incidence: Shallow streaks developed into long, deep streaks aligned with the beam direction.
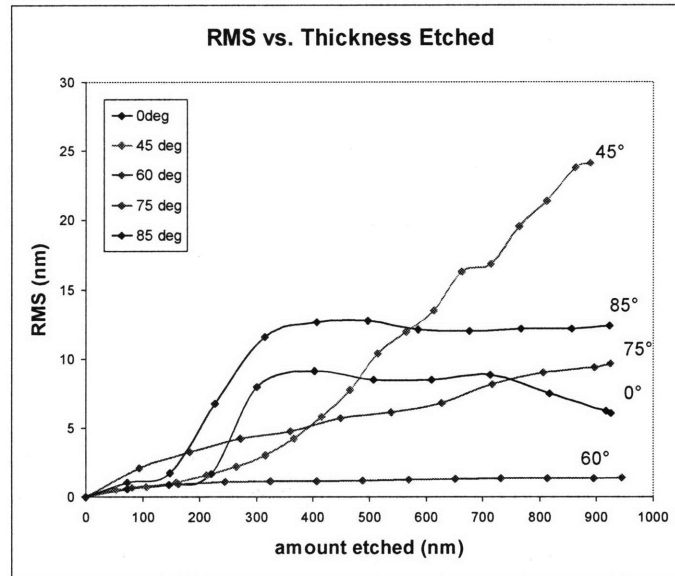
Figure 3.21: Evolution of RMS roughness. RMS roughness increases as the etching proceeds, but for the surface bombarded at 0° and 85° off-normal angle, the RMS does not change significantly after reaching a certain RMS value. Surface etched using a 60° off-normal ion incidence remained smooth compared to other angles. For both 45° and 75° off-normal ion incidence, the RMS continued to increase with etching, implying that the amplitude of the ripples kept growing.

Further analysis of the surface plots generated from the sputtering simulation in Figure 3.20 proceeded via fast Fourier transform (FFT) techniques. The FFT spectra corresponding to the surface plots are shown in Figure 3.22, with an image range of ± 0.067 nm⁻¹. The FFT spectra support the qualitative trends described previously. For all off-normal angles of incidence, the peaks at high frequency range (i.e. furthest from the center) disappeared and strong peaks appeared at low frequency range (i.e. close to the center) as the etching proceeded, implying that the wavelength of the ripples or the lateral size of valleys and hills on the surface increased with etching. For 0° off-normal incidence, the peaks are dispersed in all directions. This is consistent with the observation made on the surface plot, where the roughened surface showed no preferred orientation. For 45° off-normal incidence, most peaks are concentrated along the horizontal line passing through the center, suggesting that the ripples on the surface are

106

perpendicular to the ion beam direction (i.e. wave vector is parallel to the beam direction). For 60° off-normal incidence, the distribution of peaks does not change significantly after etching 200 nm. Surface patterns are not readily apparent from the corresponding surface plots in Figure 3.20 since the amplitude is generally very small, but from the FFT plots, it is seen that the small ripples on the surface are somewhat aligned with the beam direction. There is also a random roughness, as indicated by the broad distribution of the peaks.

average depth etched
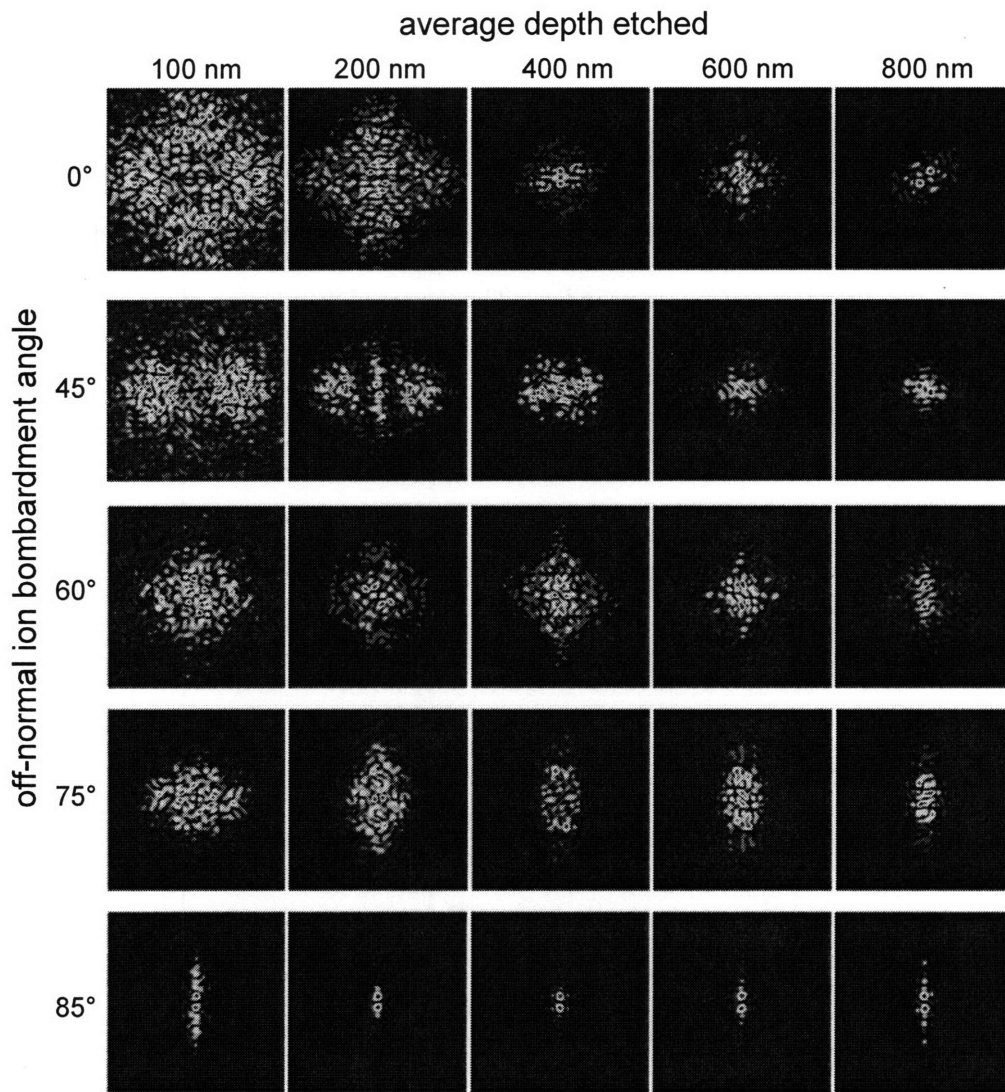
Figure 3.22: FFT spectra of the surfaces in Figure 3.20. For all off-normal angles of incidence, the peaks at high frequency range (furthest from the center) disappears as the etching proceeded, indicating the increase in the wavelength of ripples or the widths of hills and valleys on the surface. Note that for 75° and 85° off-normal incidence, the peaks are spread further in vertical direction rather than in horizontal direction. This shows that the rows of streaks formed on the surface are aligned with the beam direction.

For 75° off-normal incidence, more peaks are initially concentrated along the horizontal line through the center (i.e. there are less peaks at high frequency regions along the vertical line through the center), but as the etching proceeds, peaks are concentrated along the vertical line. This shows that the ripples formed at an early stage

108

of etching are perpendicular to the direction of the ion beam, but transform into ripples that are more aligned with the ion beam direction upon further etching, again consistent with the surface plot data. For 85° off-normal incidence, it was seen in the surface plots that the streaks aligned with the beam direction were formed at an early stage of etching, and they propagate quickly as the etching proceeds. In the corresponding FFT spectra, the peaks are concentrated along the vertical line, confirming that the streaks are aligned with the direction of the beam.

A general observable trend from the simulation is that an increase in the off-normal angle of ion incidence results in changes in the surface morphology, and there are 4 regions that can be distinguished: (1) the surface is roughened with no preferred orientation (normal incidence), (2) development of ripples that are transverse to the ion beam direction ($0°<\theta \leq 45°$ off-normal), (3) surface remains smooth independent of the etching time (~60° off-normal), and (4) formation of streaks aligned with the ion beam direction ($\geq 75°$ off-normal). In order to determine the angle at which the transition from a transverse to a smooth surface occurs, the etching of the surface was simulated with off-normal ion angles of incidence between 45° and 60° (Figure 3.23). The evolution of RMS roughness as a function of the etch amount for each off-normal angle of incidence is plotted in Figure 3.24. When the surface was etched at 50° off-normal incidence, the formation of transverse waves at an intermediate stage (after etching to a depth of 400 nm) is not as apparent as that of the 45° off-normal case. The RMS roughness is comparable to the 45° off-normal case at an early stage of etching, but upon further etching, it is seen that the RMS values remain slightly lower than those of the 45° off-normal case. The surface roughening pattern changes drastically at 55°: both the surface

109

contour and RMS roughness plot show that the surface remains smooth throughout the etching process. The surface plot shows no development of transverse waves either. For 60° off-normal incidence, the surface again remains smooth, with even lower RMS roughness values. The transition from the occurrence of transverse ripples to a smooth surface thus occurs at off-normal angles of incidence between 50° and 55°.
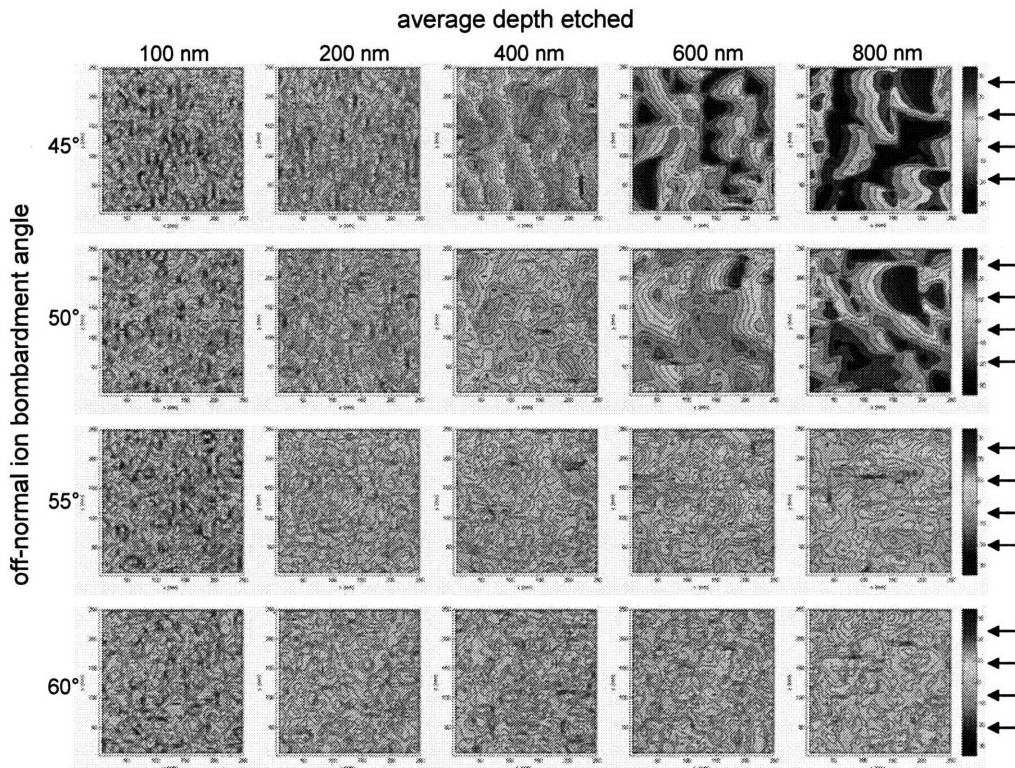
Figure 3.23: Surface etched with off-normal angles of incidence between 45° and 60°. For 45° off-normal incidence, ripples are formed on the surface, and their amplitude increases with etching. For 50° off-normal incidence, the ripple formation is not as pronounced as in the 45° case. The surface remains smooth for 55° and 60° off-normal angles of incidence, with no sign of ripple formation. Therefore, the transition from rippled surface to smooth surface occurs at an off-normal incidence between 50° and 55°.
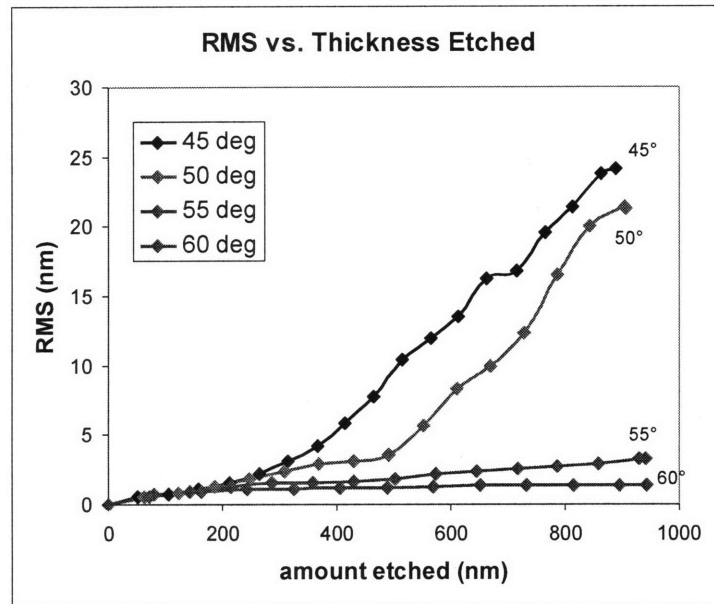
Figure 3.24: RMS evolution for the off-normal ion incidence angles from 45° and 60°. The RMS roughness is significantly lower for the surface bombarded at 55° off-normal incidence or above, suggesting that the transition occurs between 50° and 55° off-normal incidence.

Similarly, the angle at which the transition from smooth to parallel roughness surface occurs was determined by simulating the etching of a surface with off-normal ion angles of incidence between 60° and 75° (Figure 3.25). The evolution of their corresponding RMS roughness values is shown in Figure 3.26. The roughening pattern is significantly different for incident angles between 60° and 65°. The surface remains smooth for an angle of 60° off-normal, but for the case of 65° the surface is roughened significantly, forming structures that are aligned with the ion beam direction. Some regions on the surface are relatively flat which is not observed for higher off-normal incidence angles, but the overall roughening trend is similar for the considered 65°, 70°, and 75° off-normal angles of incidence, along with similar values of RMS roughness. Therefore, the transition from smooth to parallel roughness occurs between a 60° and 65° off-normal angle of incidence.

111

average depth etched
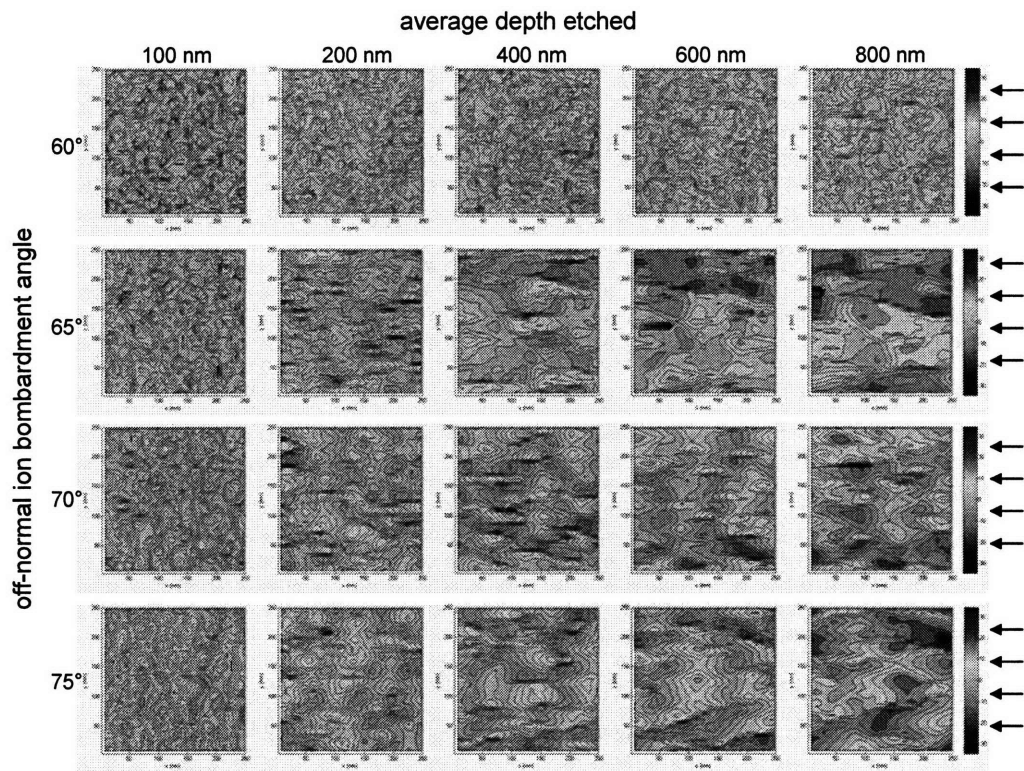
Figure 3.25: Surface etched with off-normal angles of ion incidence between 60° and 75°. The surface remains smooth for the surface bombarded at 60°, where as the surface is roughened for angles of incidence at or above 65°. Thus, the transition from a smooth to rough surface occurs between 60° and 65° off-normal incidence.
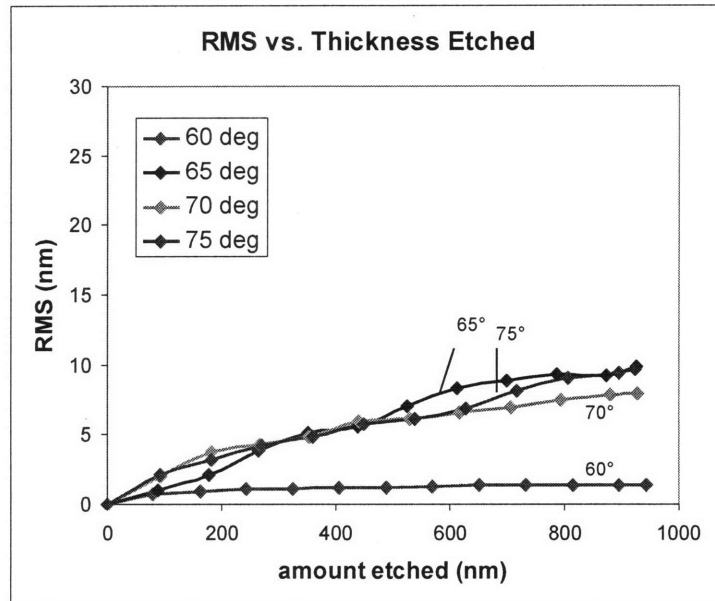
Figure 3.26: RMS evolution for the off-normal ion incidence angles from 60° and 75°. The RMS values for off-normal angles of 65° and above are significantly higher than the RMS values for 60° off-normal, suggesting that the transition occurs between 60° and 65° off-normal incidence.

3.5.2. Experimental measurements of ion-sputtered surface morphology

The simulation captured many of the trends observed in the experiments. The transition of ripple orientation from being perpendicular to parallel to the beam direction with increasing off-normal angle of ion incidence has been observed for the sputtering of both Si[12,13] and metal surfaces[14,15]. The range of off-normal angles of incidence where the surface smoothens was also previously observed[11,12]. Figure 3.27 shows the AFM images of Si surfaces sputtered by a Xe+ beam at different angles of incidence, as measured by Ziberi et al. The ripple orientation changes from being perpendicular (Figure 3.27a) to parallel (Figure 3.27b) to the beam as the angle of ion incidence was increased from 5° to 85°, and there is a range of angles in between where the surface remains smooth with no characteristic features. The author noted that similar patterns were observed when Ar+ and Kr+ ions were used. The evolution of RMS roughness

shown in Figure 3.28 supports the presence of three regions where different roughness patterns develop on the surface. The transition from a smooth to a striated surface (aligned with ion beam direction) occurred around 60°, which is consistent with our simulation result. The transition from a rippled surface (perpendicular to the beam direction) to a smooth surface occurred at about 30°, which is lower than the 55° transition angle in our simulation. The wavelength of the ripples shown in Figure 3.27a is about 50 nm, and the lateral size of the patterns in 85° off-normal incidence case shown in Figure 3.27c is about 100 nm. These values are comparable to those obtained in our simulation. Although there are differences between our results and the experimentally observed transition angles and amplitude of the ripples, the general trends in the evolution of the surface roughness are effectively reproduced in our simulation.
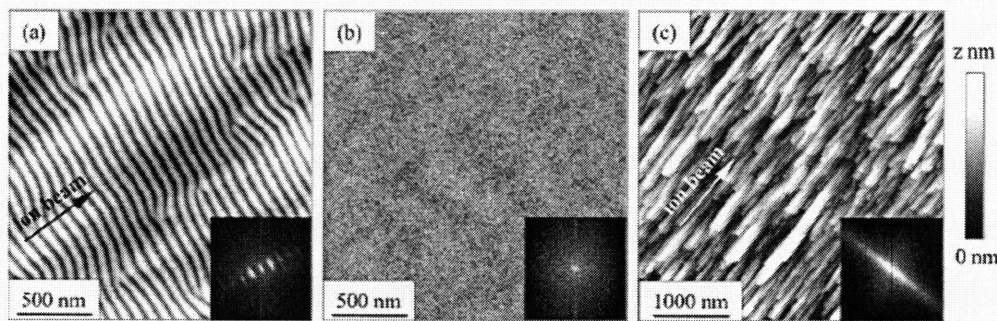
Figure 3.27: AFM images of Si surfaces sputtered by Xe+ ion beam at (a) 5°, (b) 45°, and (c) 85°. z=2 nm for (a) and (b), and z= 70nm for (c). The insets show the corresponding Fourier image of each surface (±63.5 μm^{-1}). The ripple orientation changes from perpendicular (a) to parallel (c) to the beam direction with increasing off-normal angle of incidence, and there is a range of angles in between where the surface remains smooth with no observable characteristic features (Ref. 10).

114
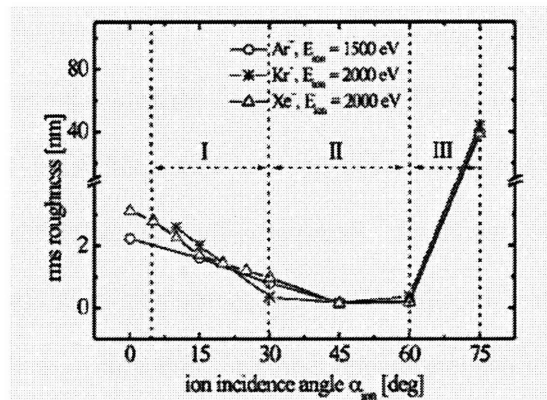
Figure 3.28: Evolution of RMS roughness with angle of ion incidence. There are three regions where different surface patterns are observed: (I) Formation of ripples oriented perpendicular to the beam direction, (II) Surface remains smooth, (III) Formation of ripples aligned with the beam direction (Ref. 11).

How does the surface morphology evolve with etch time required to generate a rippled surface or a surface with structures aligned with the direction of the ion beam? The evolution of surface patterns with etch time was measured experimentally by our group. Figure 3.29 shows the AFM images of a Si surface sputtered by Ar^+ ions at 60° off-normal incidence with different ion fluences, which in turn corresponds to the etching time. The RMS roughness does not change significantly with etch time, but the surface morphology changes from small bumps to patterns aligned with the beam direction. Another characteristic is the development of narrow ripples oriented perpendicular to the beam direction. In our simulation, the surface etched with 60° off-normal ion incidence has comparable RMS roughness values, but no apparent changes in morphology was observed. One possible reason is that since the 60° off-normal incidence is relatively close to the angle of transition from a smooth to a rough surface (see Figures 3.25 and 3.28), the surface may, within the error of the experimentally measured transition angle, result in either of them. The complex roughness pattern on the surface shown in AFM may be due to the instability of the surface at the transition angle. Similarly, in the case

115

where the Si surface was sputtered by Ar$^+$ ions at 75° off-normal incidence with different ion fluences (Figure 3.30), small ripples oriented perpendicular to the beam direction initially developed on the surface, and as the etching proceeded, the wavelength and amplitude of the ripples increased. Eventually, the ripples transformed to the pattern aligned with the ion beam direction. These trends resemble those observed in the surface etched with 75° off-normal ion incidence in our simulation (see Figure 3.25). These results suggest that at these off-normal angles, the ripples perpendicular to the beam direction are formed at an early stage of the etching process, but later change orientation and become aligned with the beam direction as the surface is etched further.

(a) 1.5x10^{17} cm^{-2} (b) 3.0x10^{17} cm^{-2} (c) 6.0x10^{17} cm^{-2} (d) 15.0x10^{17} cm^{-2}
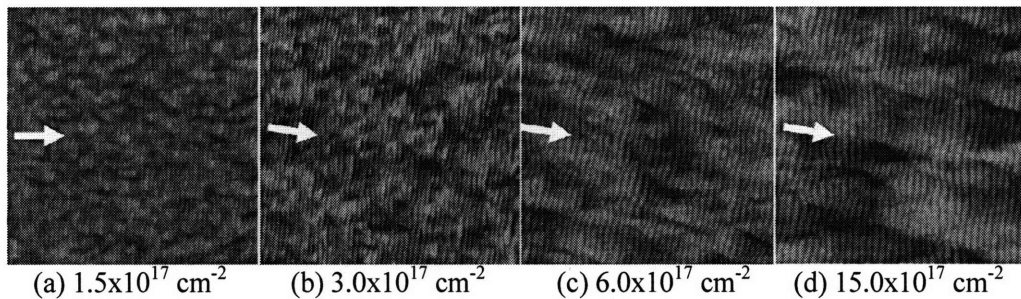
Figure 3.29: AFM images of Si surfaces sputtered by Ar+ ion beam at 60° off-normal incidence with different ion fluences. The image size is 1x1 μm2 with a vertical scale of 15 nm. The projected ion beam direction is shown by the white arrow. (a) RMS=0.63 nm, (b) RMS = 1.11 nm, (c) RMS = 0.87 nm, (d) RMS = 1.02 nm.

(a) 0.75x10^{17} cm^{-2} (b) 1.5x10^{17} cm^{-2} (c) 3.0x10^{17} cm^{-2} (d) 7.5x10^{17} cm^{-2}
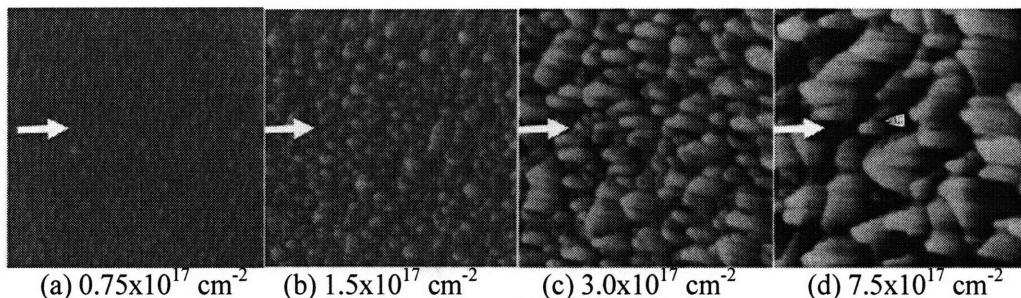
Figure 3.30: AFM images of Si surfaces sputtered by Ar+ ion beam at 75° off-normal incidence with different ion fluences. The image size is 1x1 μm2 with a vertical scale of 15 nm. The projected ion beam direction is shown by the white arrow. (a) RMS=0.70 nm, (b) RMS = 1.53 nm, (c) RMS = 3.62 nm, (d) RMS = 7.35 nm.

The AFM image for the surface etched with 75° off-normal ion incidence was re-plotted to the same scale as the simulation domain to make side by side comparisons of their surface morphologies. The comparison was made after etching to a depth of 36 nm, 72 nm and 180 nm respectively. In the simulation, a greater amount must be etched in order to observe roughness that is comparable to that observed in experiment because the surface is assumed to be perfectly flat and void of any defects or impurities before etching, which minimizes the initiation and propagation of surface roughening. The resulting general surface morphologies for both experiment and simulation, however, are comparable to each other, as depicted in Figures 3.31 and 3.32.

(a) AFM image (1x1 µm^2)   (b) contour of AFM (0.25x0.25 µm^2)   (c) simulation (0.25x0.25 µm^2)
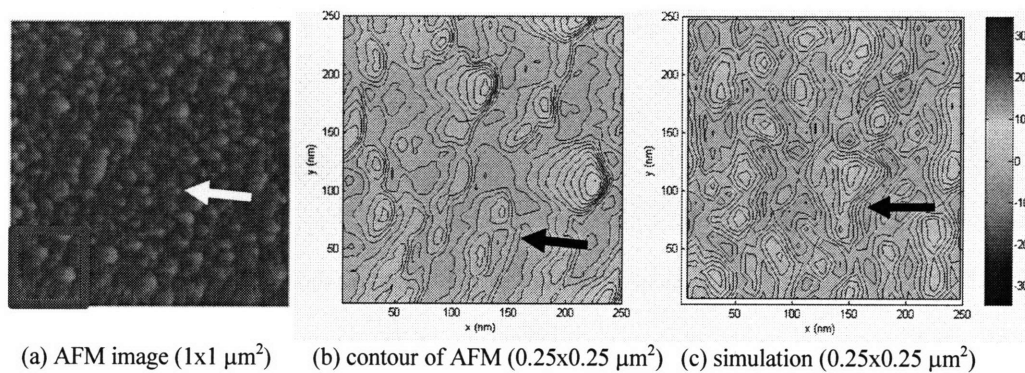
Figure 3.31: Side by side comparison of the surface morphology in experiments and simulation for 75° off-normal ion incidence. The amount etched for the experiment and for the simulation are 36 nm and 100 nm, respectively.

(a) AFM image (1x1 μm²)   (b) contour of AFM (0.25x0.25 μm²)   (c) simulation (0.25x0.25 μm²)
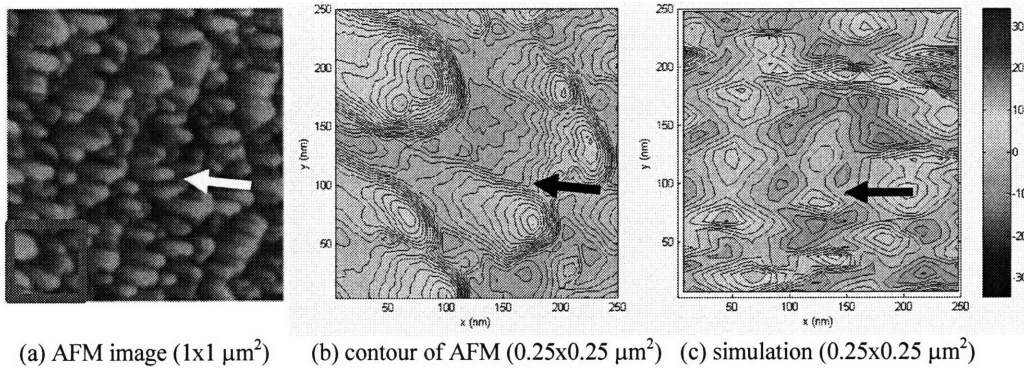
Figure 3.32: Side by side comparison of the surface morphology in experiments and simulation for 75° off-normal ion incidence. The amount etched for the experiment and for the simulation are 72 nm and 360 nm, respectively.

(a) AFM image (1x1 μm²)   (b) contour of AFM (0.25x0.25 μm²)   (c) simulation (0.25x0.25 μm²)
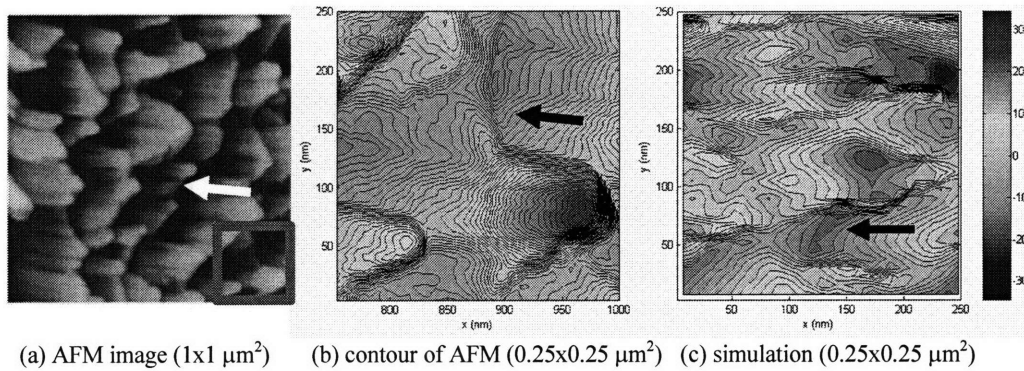
Figure 3.33: Side by side comparison of the surface morphology in experiments and simulation for 75° off-normal ion incidence. The amount etched for the experiment and for the simulation are 180 nm and 890 nm, respectively.

3.5.3. Correlation between the angular dependence yield curve and surface roughening

In sections 3.5.1 and 3.5.2, it was observed both in simulations and in experiments that the surface morphology changes with increasing off-normal angles of ion incidence. We surmise that this phenomenon may be related to the angular dependence of the sputtering yield. Recall that the simulation showed 4 distinct regions that resulted from different ion angles of incidence, namely: (1) the surface is roughened with no preferred orientation, (2) the development of ripples that are transverse to the ion beam direction,

118

(3) the surface remains smooth independent of the etching time, and (4) the formation of streaks aligned with the direction of the ion beam. These regions are labeled on the angular dependence yield curve shown in Figure 3.34. Note that the transition from a smooth surface (region 3) to striations parallel to the ion beam direction (region 4) occurs at about 15° below the angle corresponding to the peak yield (75°) as shown in Figure 3.34. The range of angles defined by region 3, where the surface is smooth, is about 10°, which is much narrower than regions 2 and 4. Transverse waves develop on the surface when the ion incidence angle is below 50°. (Note that region 1, where the roughened surface does not have any preferred orientation, occurs at normal incidence and is not shown in the plot.)

The shape of the angle-dependent yield curve may be slightly different for different materials and process conditions. For example, the peak position of the sputtering yield typically occurs at high angles of incidence for the sputtering of light atoms whereas it is at lower angles for the sputtering of heavy atoms[16]. It is worth exploring the effects of angular dependence on the evolution of surface morphology especially if the shape of the angular dependence yield curve is correlated with the resulting surface patterns, because the simulator can be used to predict the resulting surface roughness for any material by simply knowing the experimentally measured angular dependence of its etching yield.
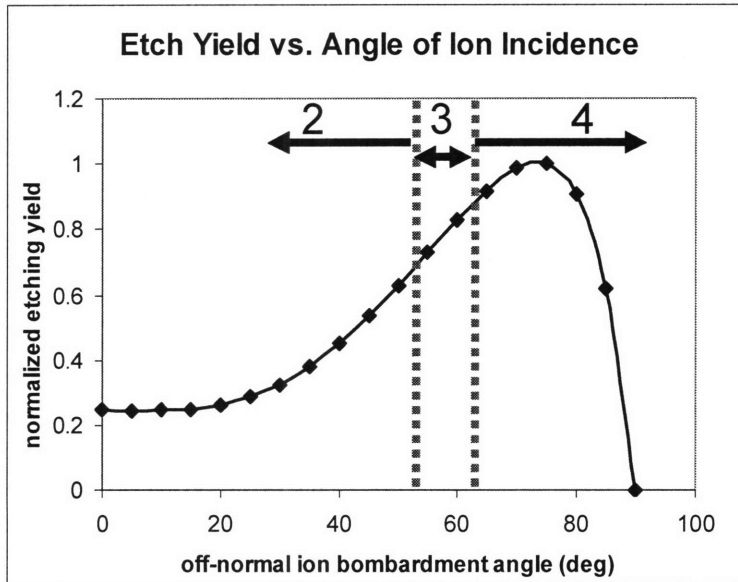
Figure 3.34: Correlation between the angular dependence of the sputtering yield and the different regions of surface roughening. Region 2: Formation of ripples perpendicular to the beam direction. Region 3: Surface remains smooth. Region 4: Formation of ripples parallel to the beam direction. (Region 1, where the surface roughness has random orientation, occurs at 0°, which is not shown.) The 10° window of smooth surface occurs at about 15° below the angle of the peak yield.

In order to verify the correlation between the angle corresponding to the peak yield and the transition angle, the former was shifted from 75° to 65° (Figure 3.35), and the etching of the surface at different off-normal ion angles of incidence was simulated using this angular dependence. The results are shown in Figure 3.36. The general trends are similar to the case with the peak yield at 75° (Figure 3.20), except that at 60° off-normal incidence, the surface is roughened significantly whereas it was smooth when the previous angular dependence curve was employed. Additionally, when the surface was etched at 45° off-normal incidence, the formation of ripples transverse to the beam direction is not very apparent, unlike the results obtained previously. The increase in RMS roughness with etching is also not as drastic. This suggests that the range of angles of incidence which results in a smooth surface lies somewhere between 60° and 45°.

120
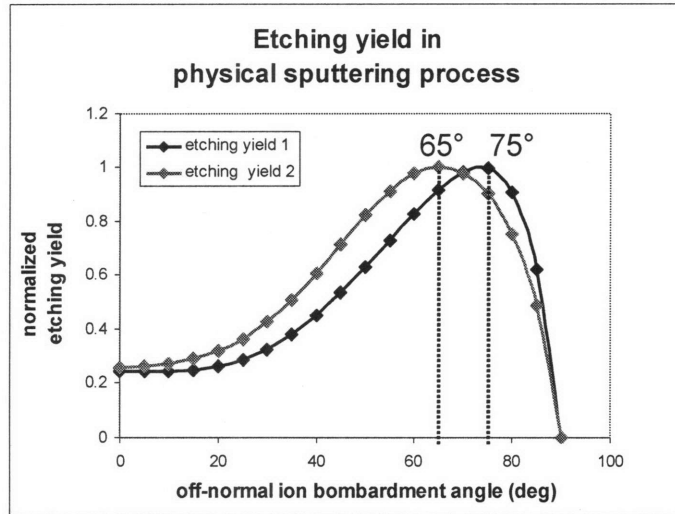
Figure 3.35: Shifting the angle of the peak yield from 75° to 65° off-normal incidence. The general shape of the yield curves are kept similar.
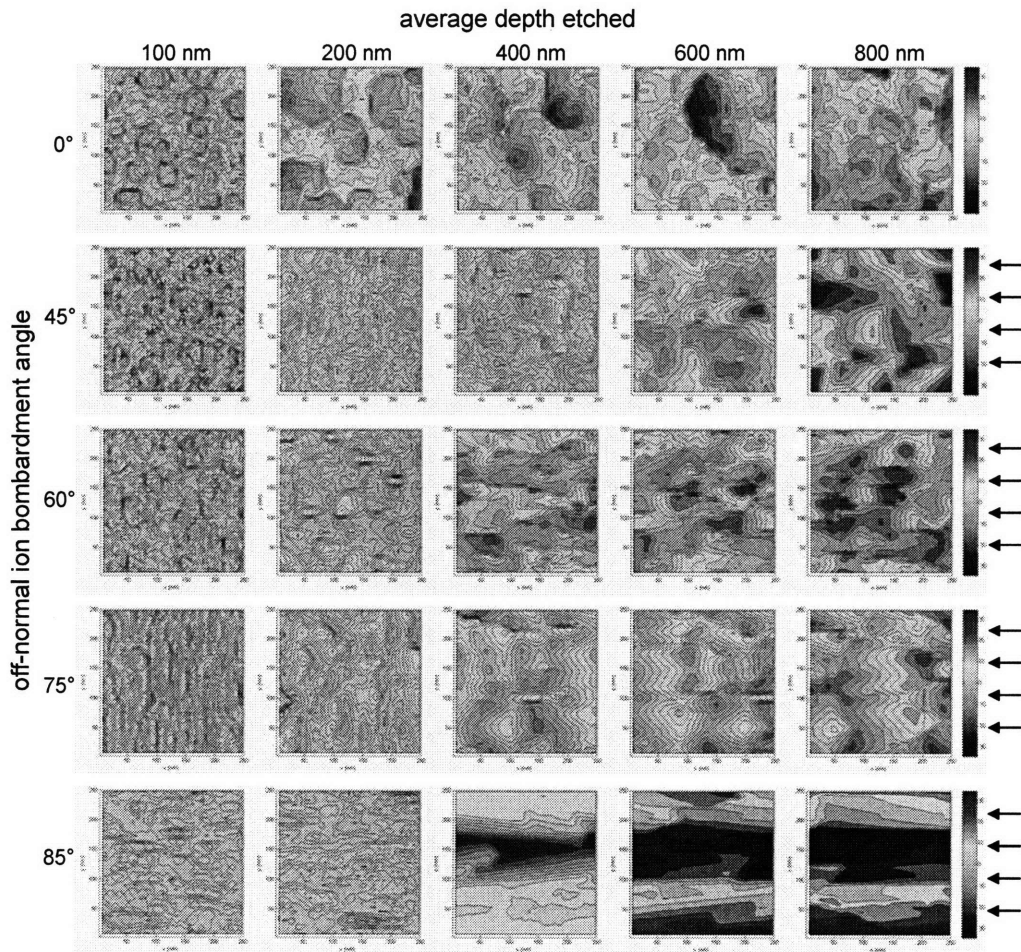
Figure 3.36: Surface etched with different off-normal ion incidence angles, using the angular dependence curve with its peak yield at 65°. The vertical scale is ±35 nm, and the arrows define the ion beam direction. The trends in surface morphology are similar to the case with the peak yield at 75° (Figure 3.20), except that the surface is roughened at 60° off-normal incidence, whereas in the previous case the surface remained smooth.
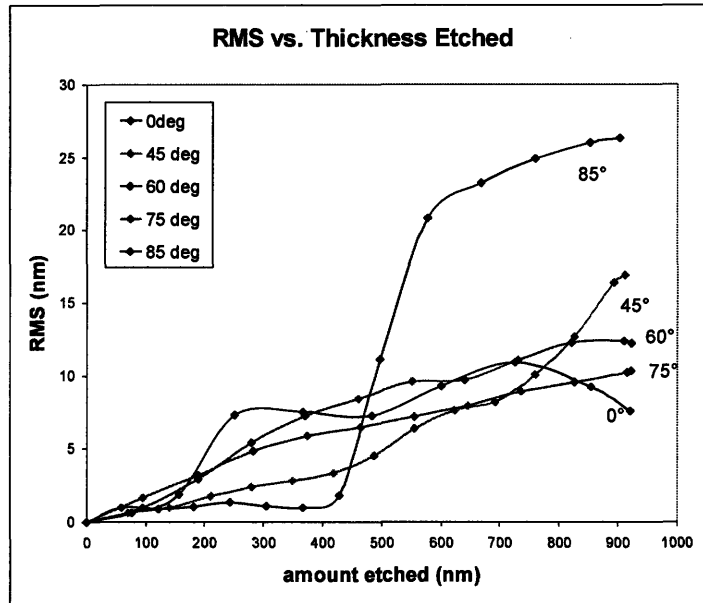
Figure 3.37: RMS roughness evolution for the angular dependence with peak yield at 65°. RMS increases with etching for all off-normal angles.

In order to determine at the angle at which the transitions occur, the etching of the surface was simulated at smaller increments of off-normal angles between 45° and 75°. As shown in Figure 3.38, the surface is roughened when it is etched at 45° off-normal incidence, but the surface remains smooth for off-normal incidence angles of 50° and 55°. This is also apparent from the low RMS roughness for these angles as shown in Figure 3.39. For angles of incidence of 60° and above, the surface is roughened again, and the structures formed on the surface became more aligned with the ion beam direction. These regions are labeled with the sputtering yield curve in Figure 3.40. The transition from a smooth (region 3) to a rough surface (region 4) occurs at about 10° below the peak yield angle (65°), and the angular range of the smooth region (region 3) is about 10°. These results are comparable to the case with peak yield at 75°, except that the transition angles are shifted about 10° lower.

average depth etched
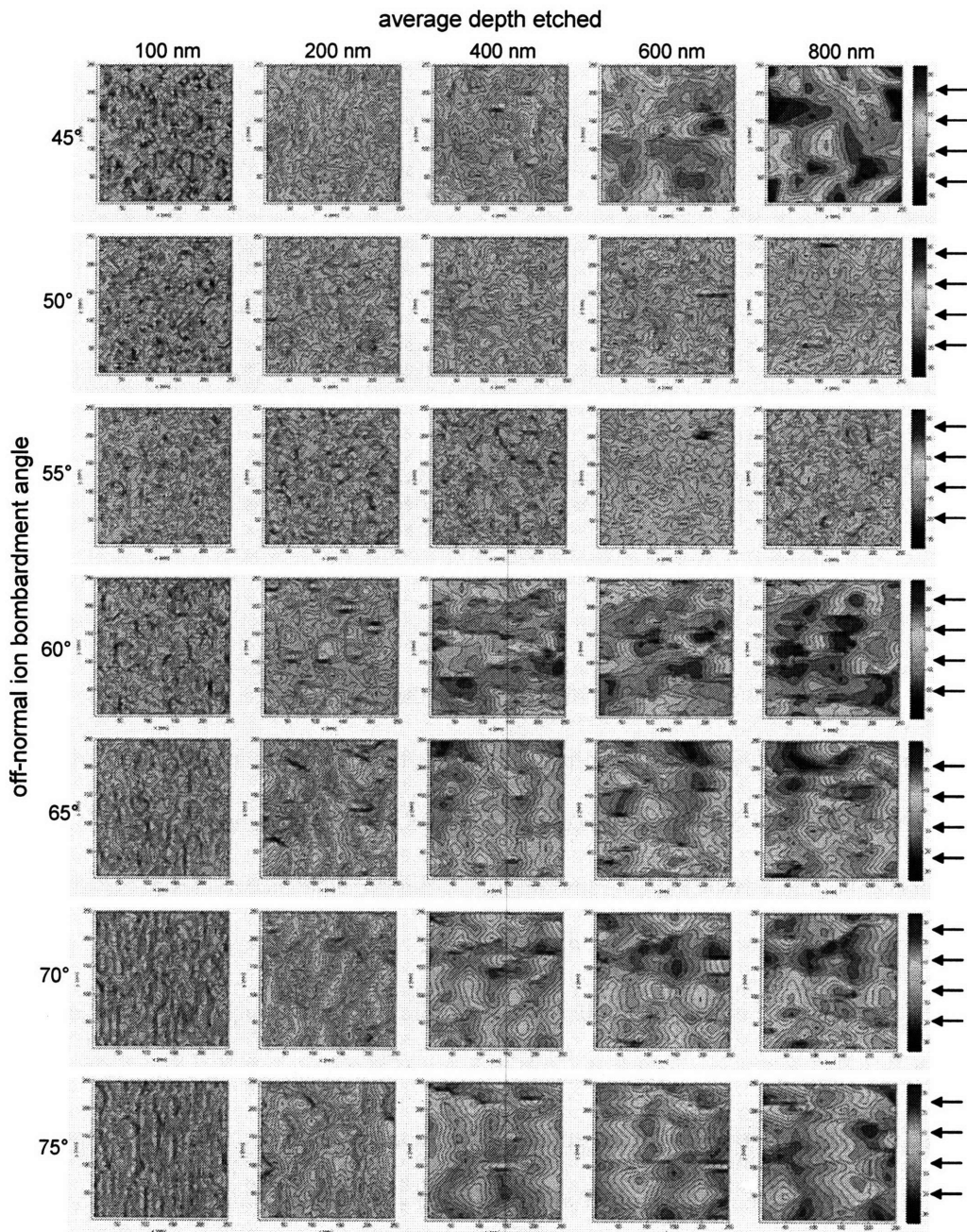
Figure 3.38: Surface etched with off-normal ion incidence angles between 45° and 75°, using the angular dependence with the peak yield at 65°. The vertical scale is ±35 nm, and the arrows give the ion beam direction. The surface is roughened at 45° off-normal incidence, smooth at 50° and 55°, and roughened again above 60°.
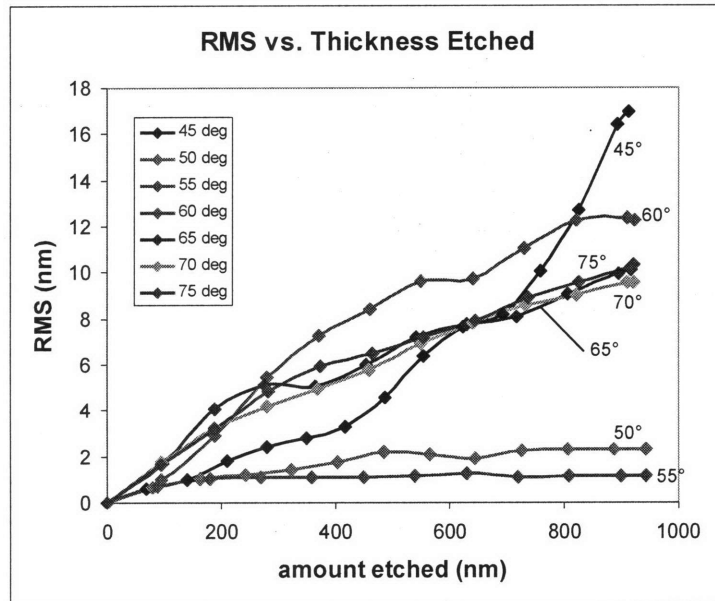
Figure 3.39: RMS roughness evolution for the angular dependence with peak yield at 65°. The RMS values are very low for the surfaces bombarded by 50° and 55° off-normal incidence.
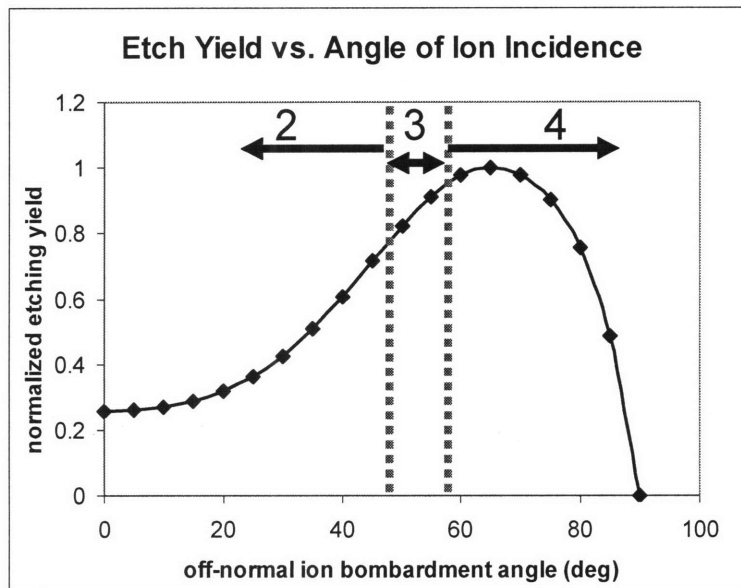
Figure 3.40: Correlation between the angular dependence of sputtering yield and the different regions of surface roughening. Region 2: Formation of ripples perpendicular to the beam direction. Region 3: Surface remains smooth. Region 4: Formation of ripples parallel to the beam direction. (Region 1, where the surface roughness has random orientations, occurs at 0°, which is not shown.) This 10° window of smooth surface occurs at about 10° below the angle of the peak yield.

The evolution of the surface roughness with ion angles of incidence between 45°
and 75° for the two different angular dependence curves is summarized in Figure 3.34.
In both cases, there is a region where the RMS values are very low. This low RMS
roughness region is observed at a lower off-normal ion incidence after shifting the peak
yield of the angular dependence curve to a lower off-normal ion incidence, which
suggests that there may be a correlation between the angle at which the yield peaks and
the angle at which the transition from a smooth to a rough surface occurs. This may be
explicated by the difference in the probabilities of ion scattering in the two cases. Recall
that the drop in the sputtering yield at high off-normal angles of incidence is due to the
increase in the scattering of ions. The angular dependence of the etching yield and
scattering probability for both cases are plotted in Figure 3.42. It was assumed that the
scattering of ions is negligible for off-normal angles of incidence below the angle
corresponding to the peak yield. For the case in which the yield peaks at 65°, the
scattering of ions occur above 65° and continues to increase with increasing angles of
incidence. However, for the case in which the yield peaks at 75°, ion scattering occurs
only when the off-normal angle of incidence is above 75°, which is higher than 65°.
Structures that align with the ion beam direction are formed largely due to the channeling
of ions, and this roughening process occurs at higher off-normal angles if the scattering
of ions occur only at those high off-normal angles.
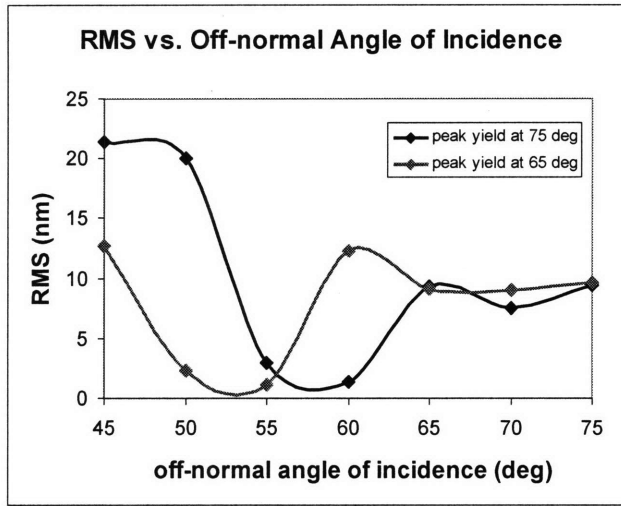
Figure 3.41: RMS roughness evolution with off-normal angle of ion incidence after etching 800 nm. For both angular dependences, there exists a range of angles where the RMS is very low. This range occurs at lower angles for the angular dependence with a lower peak yield angle.
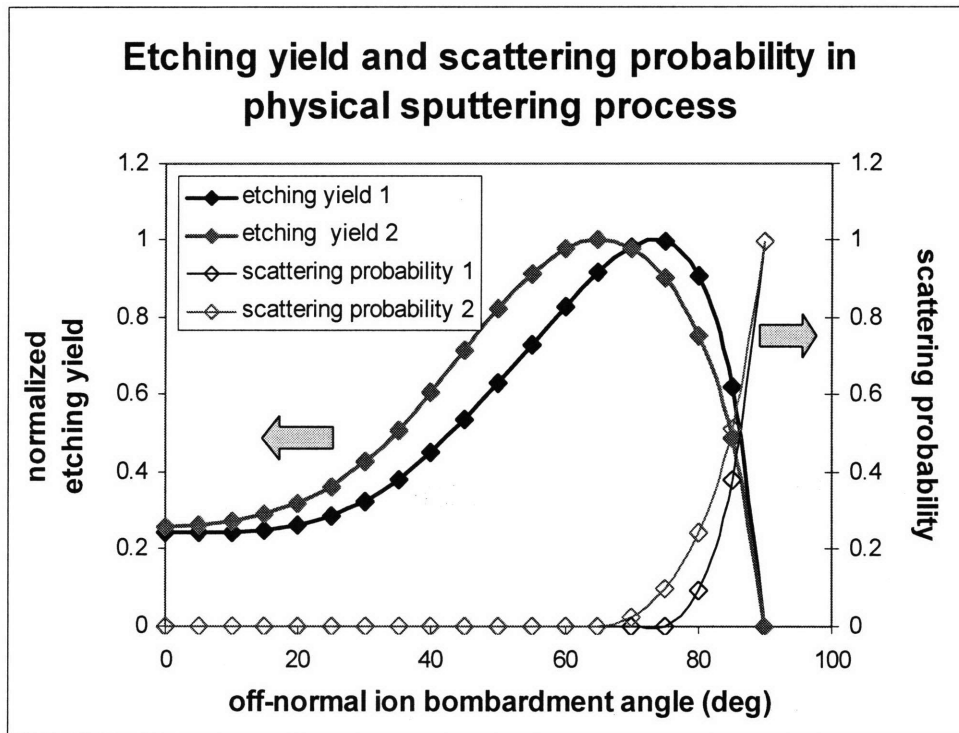
Figure 3.42: Etching yield and ion scattering probability in a physical sputtering process. (1) Peak yield is at 75°. (2) Peak yield is at 65°. The scattering probability starts increasing at lower off-normal angle for the angular dependence with peak yield at lower angle.

For certain materials and process conditions, the ratio of etching yield at normal incidence to the peak yield may be higher, as shown in Figure 3.43. This happens when the ion energy is very low or when the etching of the surface is more "chemical" rather than "physical," which means that it involves chemical reactions on the surface during the etching process. In this instance, is the evolution of surface morphology different from the case with a lower normal incidence to peak yield ratio? To answer this question, the same set of simulations was performed using the angular dependence of the etching yield curve (2) depicted in Figure 3.43.
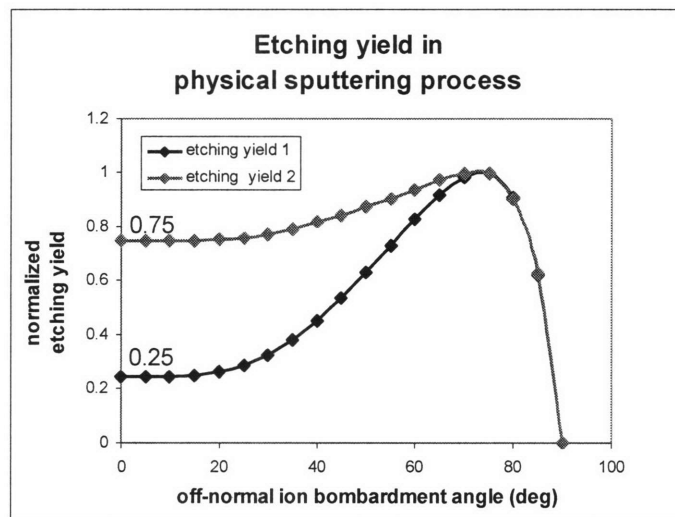
Figure 3.43: Angular dependent etching yield curves with different ratios of etching yields for normal to peak yield angles. (1) Ratio = 0.25. (2) Ratio = 0.75. The peak yield occurs at 75° off-normal for both curves.

The surfaces sputtered by different off-normal angles of ion incidence are shown in Figure 3.44, and their corresponding RMS evolution is shown in Figure 3.45. Similar transitions of surface patterns were observed, from no preferred orientation (0°) to perpendicular ripples (45°, 60°) to features parallel to the beam direction (75°, 85°) as the off-normal angle of incidence was increased, but there are certainly some differences in surface morphology compared to the case with a lower normal-to-peak yield ratio (see

Figure 3.20). For the surface sputtered with normal ion incidence, the depth of each cavity increases with etching, but the diameters of the cavities do not grow significantly. The increase in RMS roughness shown in Figure 3.45 also suggests a significant increase in the depth of the cavities. For the case with a lower normal-to-peak yield ratio (Figure 3.20), the diameters of the cavities grow as etching proceeds and as neighboring cavities merge, the surface becomes roughened in a more random fashion. Further etching does not cause any increase in the amplitudes of the cavity depth profiles. The surfaces etched with 45° and 60° off-normal angles of incidence resulted in a ripple formation perpendicular to the ion beam direction, but the wavelength of the ripples did not grow significantly with etching, unlike in the case with a lower normal-to-peak yield ratio. For 75° off-normal incidence, the surface morphology changes from ripples perpendicular to the beam direction to patterns aligned with the beam direction as the etching proceeds. While this trend is similar to the case with a lower normal-to-peak yield ratio, the peaks on the surface are significantly higher than those observed in the previous case at later stages of etching. This is also apparent from the large increase in RMS roughness with etching (compare Figure 3.46 with Figure 3.21). In addition, the edge of the peaks facing the ion beam is much steeper than in the previous case, as elaborated further below. For 85° off-normal incidence, the surface pattern is similar to the previous case, but the amplitude of the height profiles of the features grow to a much larger value.

These observations can be explained by the high etching yield for normal or close to normal ion incidence in this angular dependence curve. When the surface is bombarded by ions at normal incidence as shown in Figure 3.45a, the bottom of the crater (2) is eroded faster than the sidewalls (1, 3) because the etching yield at normal incidence

is higher compared to the etching yield at grazing angles of incidence. As the bottom of the crater is etched, the sidewalls become steeper, resulting in less ion flux incident upon them. If the etching yield at normal incidence is relatively low, as in the case with a low normal-to-peak yield ratio, the surface at points 1 and 3 will be eroded at a comparable rate with the bottom of the crater (2), resulting in an expansion of the crater diameter. When the surface is bombarded at a 45° off-normal ion angle of incidence, ripples are formed on the surface, and the wavelength of the ripples do not change significantly because there is less variation in the etch yield for off-normal angles between 0° and the peak yield angle (75° in this case). The surface etched with 75° off-normal incidence generated peaks with steep edges that faced the direction of the ion beam. This is because the edge facing the ion source is bombarded at or close to normal angles of incidence, which results in a higher erosion rate.

average depth etched
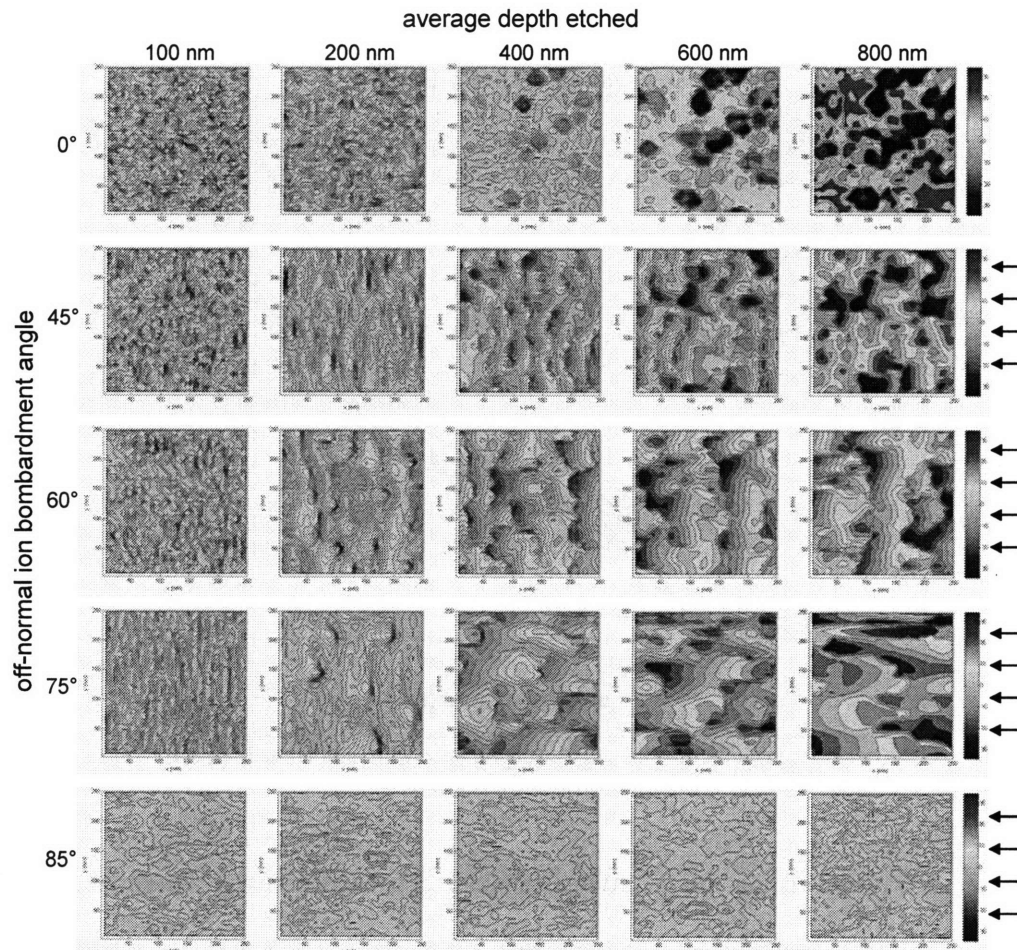
Figure 3.44: Surface etched with different off-normal incidence using the angular dependence with high normal-to-peak yield ratio. The transitions from no preferred orientation (0°) to transverse ripples (45°, 60°) to patterns parallel to the ion beam (75°, 85°) are observed, but the surface morphology is quite different from the case with a low normal-to-peak yield ratio.
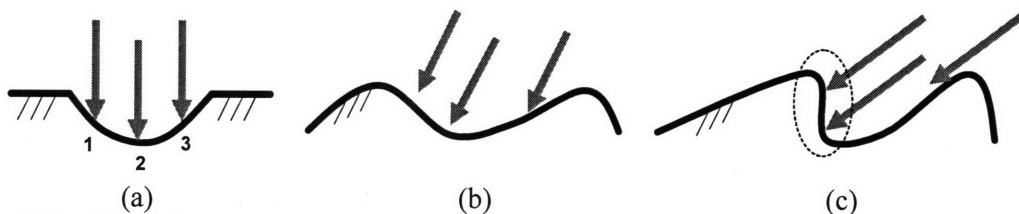
Figure 3.45: Schematic illustration of a surface bombarded at different off-normal angles. (a) Normal ion incidence. (b) 45° off-normal incidence. (c) 75° off-normal incidence. See text for description.
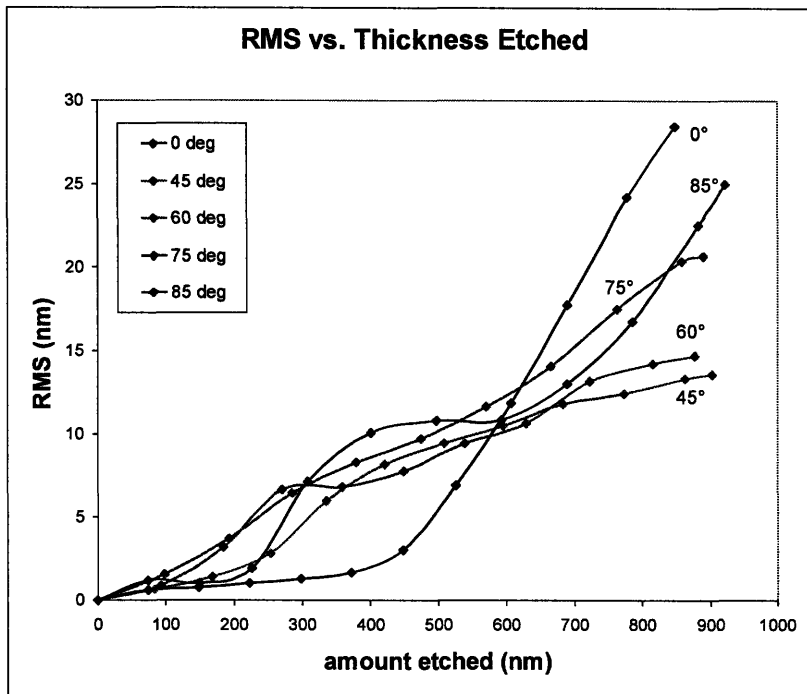
Figure 3.46: RMS roughness evolution for the angular dependence with high normal-to-peak yield ratio. For all off-normal angles, the RMS roughness increases with etching.

It was shown that for a different angular dependence curve, the surface goes through surface morphological transitions from no preferred orientation to perpendicular ripples to structures aligned with the ion beam direction as the off-normal angle of incidence was increased, but it is not clear whether there exists a range of angles where the surface remains smooth. To check the presence of this range of angles, the simulation was again performed with small increments of angles of off-normal incidence between 45° and 75° (Figure 3.47). Although the surface structures become more aligned with the ion beam direction as the off-normal angle of incidence increases, the range of angles resulting in a smooth surface was not observed. The RMS values are also comparable to each other, as shown in Figure 3.48. The RMS roughness evolution with off-normal ion incidence is summarized in Figure 3.49, together with the RMS data from previous cases

where a different angular dependence yield curve was used. As shown in Figure 3.49, the RMS remains relatively constant, unlike in the previous two cases. This shows that the range of angles generating a smooth surface appear only if the ratio of the etching yield at normal incidence to the peak yield is low, i.e. there is a large variation in the etch yield as a function of the off-normal angle of incidence. Although further experimental studies may be required to confirm these results, the simulation results suggest a high correlation exists between the angular dependence and the observed morphology of etched surfaces.
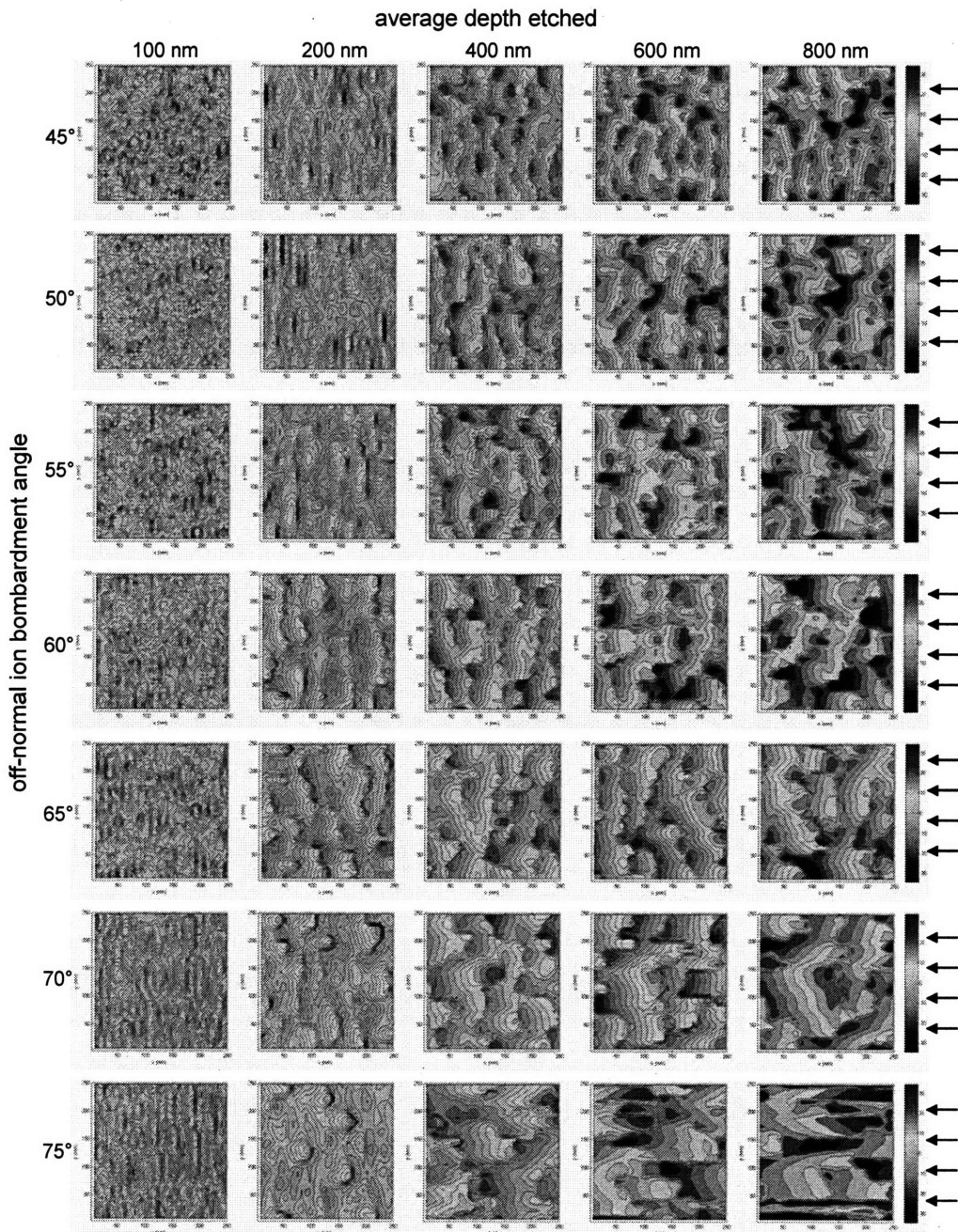
Figure 3.47: Surface etched with off-normal incidence between 45° and 75° using an angular dependence etch yield curve with a high normal-to-peak yield ratio. As the off-normal angle of incidence is increased, surface structures become more aligned with the ion beam direction, but there is no range of angles where the surface remains smooth.

134
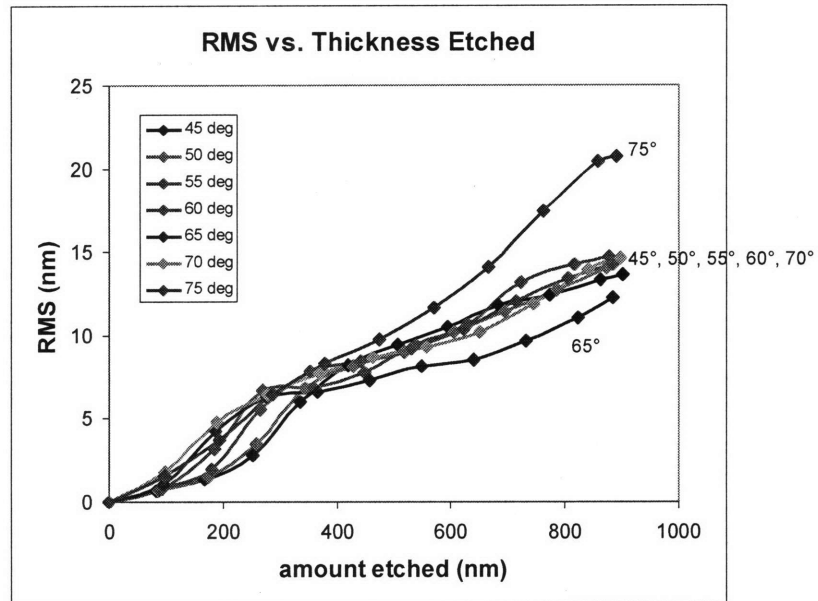
Figure 3.48: RMS roughness evolution for the angular dependence with high normal-to-peak yield ratio for angles of incidence between 45° and 75°. The RMS roughness values are comparable to each other.
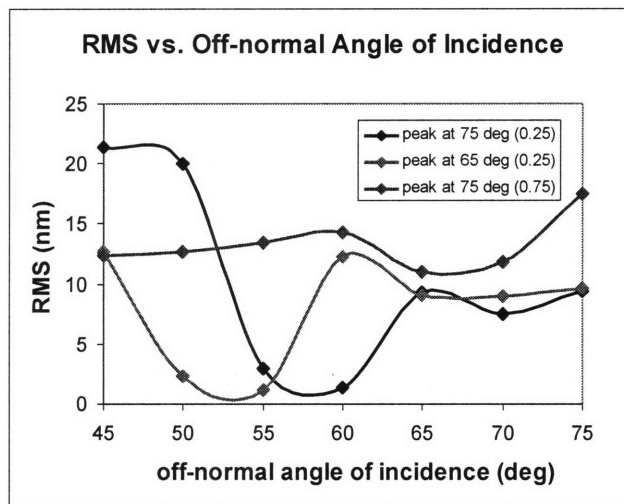
Figure 3.49: RMS roughness vs. off-normal incidence after etching 800 nm. The values in parenthesis in the legend show the normal-to-peak yield ratio. For the two cases with low normal-to-peak yield ratios, there is a range of angles where the RMS values are very low, whereas for the case of a high normal-to-peak yield ratio, the RMS values remain relatively constant.

135

3.5.4. Effects of angular distribution of ions after reflecting from the surface

In the previous cases, it was assumed that the ions scatter from the surface at perfectly specular angles. In reality, ions scatter from the surface according to an angular distribution. The molecular dynamics simulations of Ar+ impacting against a silicon surface showed that this distribution angle is about ±15°[17]. In order to examine the effect of angular distributions, the simulation case shown in Figure 3.20 was repeated, this time assuming that the scattered ions have an angular distribution about a certain specular angle. The angular distribution was assumed to follow a Gaussian distribution with a full width at half maximum (FWHM) of about 30° (±15°), as illustrated in Figure 3.50.
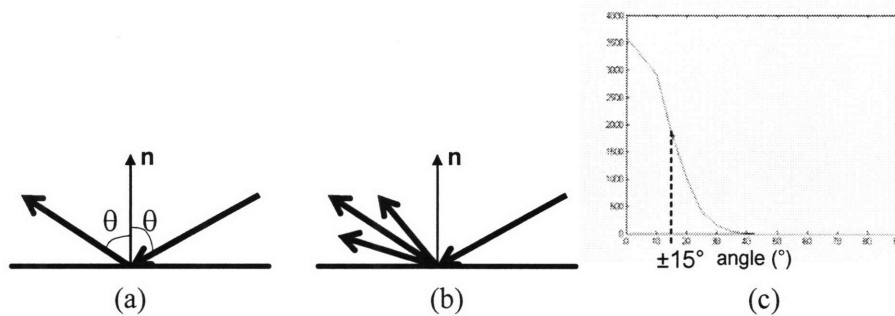
Figure 3.50: Angular distribution of scattered ions. (a) Specular scattering of bombarding ions. (b) Ions scatter from the surface with an angular distribution about a specular angle. (c) Gaussian angular distribution of scattered ions, with a FWHM of 15°.

The resulting surfaces are shown in Figure 3.51, and their corresponding RMS roughness is shown in Figure 3.52. The RMS roughness values for the case with no angular distribution are also plotted for comparison. For the surface etched with 0°, 45° and 60° off-normal ion angles of incidence, there is no significant difference in the roughness pattern from their counterparts with no angular distribution (see Figure 3.20). The RMS roughness values are also comparable at these angles, which is reasonable because at low off-normal angles of incidence the scattering probability of ions is very

low, and therefore changing the angular distribution has little effect on the etch profile. The scattering of ions increases as the surface is roughened since the local ion incidence angles will be significantly different from the macroscopic incidence angle (i.e. different from 0°, 45° and 60° off-normal ion incidence). However, once the surface is sufficiently roughened, scattered ions are dispersed widely even if there were perfect specular scattering because of large variations in the local incidence angles, as illustrated schematically in Figure 3.53. Therefore, the angular distribution of scattered ions does not make a significant difference in the resulting roughness pattern.
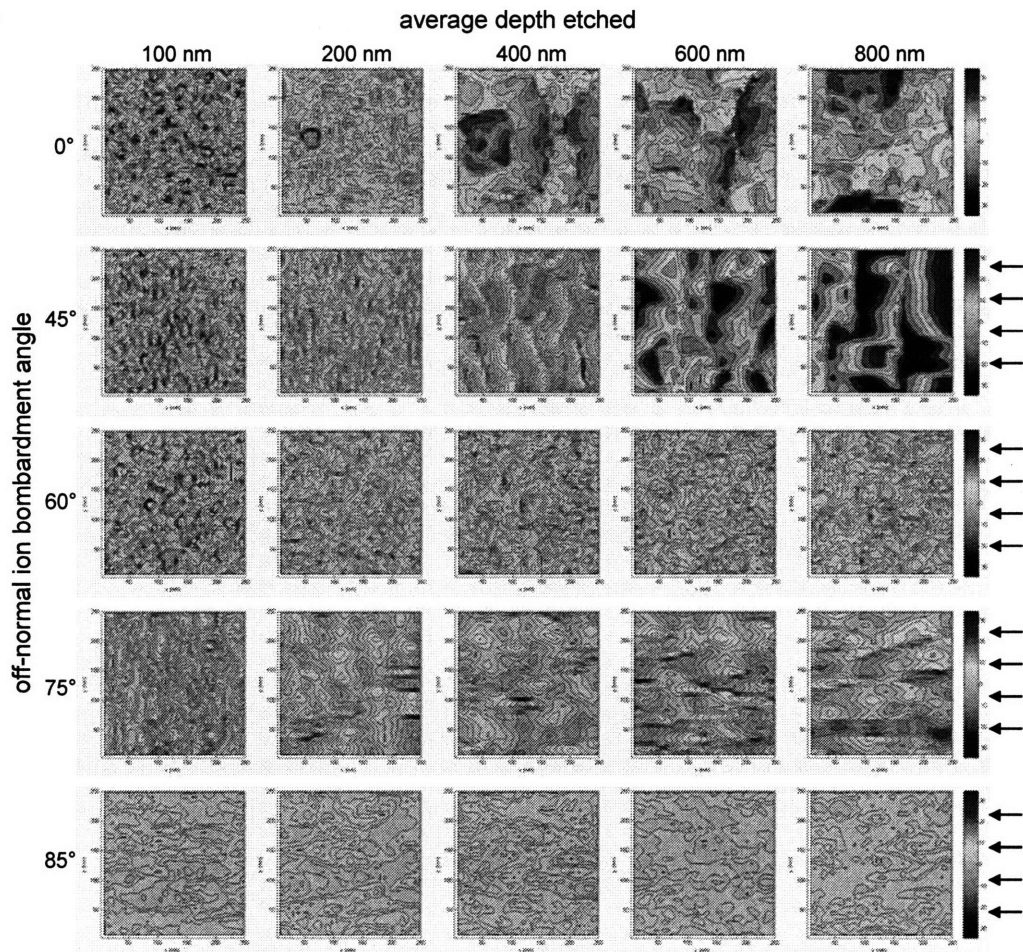
Figure 3.51: Surface etched with different off-normal ion incidence assuming 15° angular distribution of scattered ions. The surface morphology resembles the results for the case with no angular distribution of scattered ions, except at 85° off-normal incidence: The surface remains smooth whereas in the case with no angular distribution, the surface was roughened, with resulting features that were aligned with the beam direction.
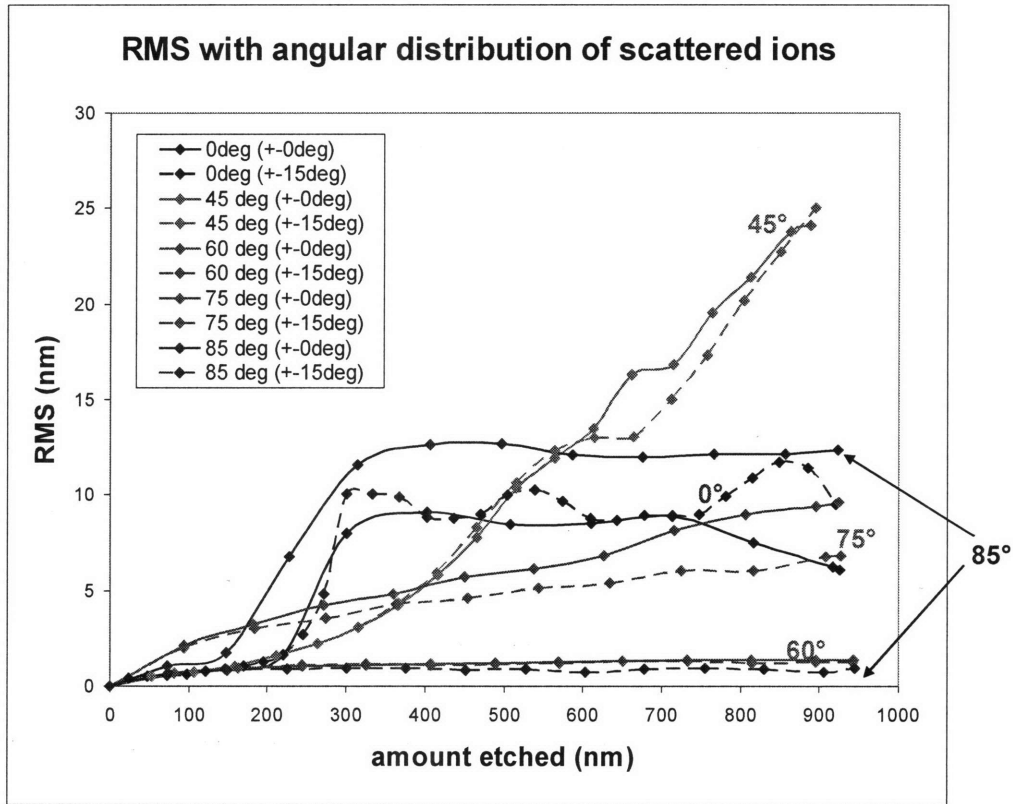
Figure 3.52: RMS roughness evolution for 0° (solid lines) and 15° (dashed lines) angular distributions of scattered ions. There is no significant deviation except for 85° off-normal incidence.
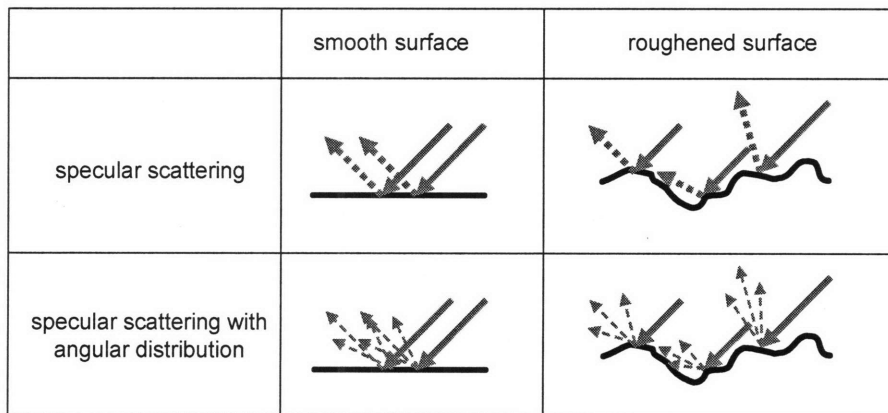
Figure 3.53: Schematic illustration of ion scattering with and without angular distribution. If the ions scatter from the smooth surface at a perfectly specular angle, all the scattered ions will have the same trajectory after leaving the surface. If the ions scatter according to an angular distribution, there will be a resulting distribution of scattered ion trajectories. If the surface is roughened, however, the angular distribution of scattered ions have less effect on etching because even with perfectly specular scattering, the reflected ions are dispersed widely due to large variations in the local angle of incidence on the roughened surface.

The surface etched at 75° off-normal incidence with an angular distribution of scattered ions does not show any significant difference from the case with no angular distribution (see Figure 3.20), but the height fluctuations of the features on the surface for the former is slightly lower than that of the latter case. The RMS roughness of the former case is about 20 to 30% lower than that of the latter. It is logical that the angular distribution of scattered ions affects the etching at 75° off-normal incidence more than in cases of lower off-normal incidence because the occurrence of ion scattering is higher at higher off-normal angles of incidence. The fluctuations in height, or amplitude, of the features formed are smaller for the case with angular distribution because the ion dispersion tends to make the flux to each part of the surface more uniform.

The surface etched at 85° off-normal ion incidence with an angular distribution of scattered ions resulted in a very smooth surface, whereas the case with no angular distribution at the same off-normal angle of incidence resulted in a very rough surface with striations on the surface aligned with the ion beam direction (see Figure 3.20). The difference in amplitude is also apparent from the RMS roughness values shown in Figure 3.52. The corresponding FFT spectra are shown in Figure 3.54. It is difficult to glean the roughness pattern from the surface plots in Figure 3.51, but it should be recalled that the absence of peaks at high frequency in the x-direction (parallel to the ion beam direction) in the FFT plots implies that the surface structures are still more aligned with the ion beam direction. The peaks are more dispersed (i.e. broader), indicating that there are more variations in the spatial frequency of the streaks, and the structures are less aligned with the beam direction compared to the case with no angular distribution. The absence of severe roughness for the case with an angular distribution of scattered ions suggests

that the roughening of the surface at very grazing angles is initiated by the focusing of scattered ions to form a shallow trench, which extends along the beam direction as the ions channel their way through the trench. If the scattered ions are dispersed, they do not get focused onto a small area, and the surface is thus etched more uniformly. It is therefore plausible to assume that some perturbation of the surface must be made before the channeling of ions can occur. In the experimental measurements, the surface is roughened severely at 85° off-normal incidence. This suggests that at very grazing angles, the angular distribution of scattered ions may be much smaller than ±15°. This is reasonable because ions retain more of their initial energy after scattering at high off-normal angles (grazing) than at low off-normal angles, thus minimizing the angular dispersion. Furthermore, the initial surface may not be perfectly smooth, and the small "seeds" of roughness on the surface may propagate to form a highly roughened surface, with patterns that are aligned with the beam direction.
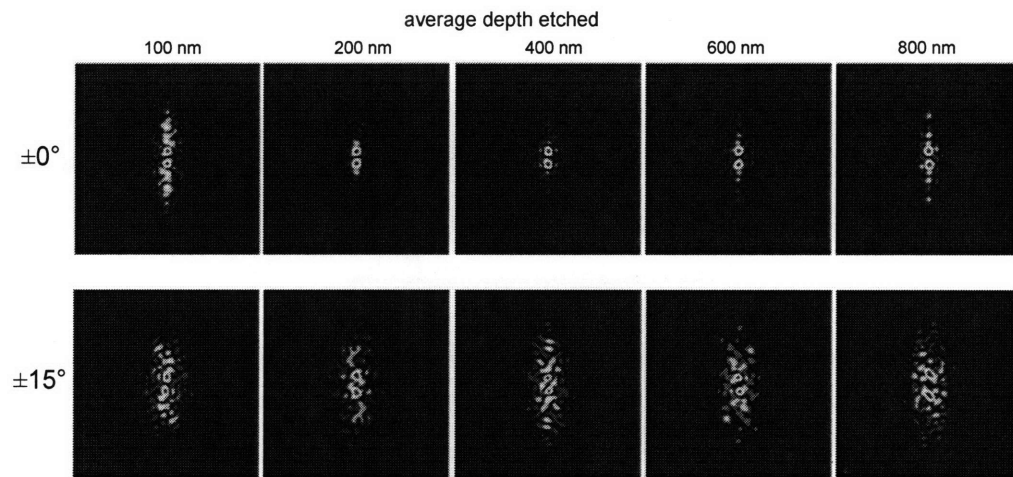
Figure 3.54: Fourier spectrum of the surface etched with 85° off-normal incidence, with 0° and ±15° angular distribution of scattered ions. In both cases, the peaks are concentrated along the center vertical line, indicating that the patterns are aligned with the ion beam direction. The peaks are broad and dispersed for the case with angular distribution, implying that the surface pattern is less ordered. The image range is ± 0.067 nm-1.

3.5.5. Effects of non-uniform density of the film

Although a single crystal silicon surface has a very uniform material density, many materials with non-uniform density are often used in the manufacturing of IC chips. These materials include porous materials that are used to replace silicon dioxide as the dielectric material for interconnects in order to reduce capacitive delay and power consumption. The insulator material is sometimes doped with carbon or fluorine to lower the dielectric constant (low-k), which also causes non-uniformity in the film density. The photoresist film used for patterning is also a chemically and structurally complex material that has a non-uniform density. In this section, the effect of non-uniform density on surface roughening is explored. The non-uniformity of the film density was generated by introducing pores of different sizes to the film at random positions (Figure 3.55), and the surface was allowed to be etched under different off-normal ion angles of incidence. The angular distribution of scattered ions was assumed to be ±15°. The average diameter of a pore in porous low-k dielectric films is about 4 nm with a size distribution of about 30 to 50%[18]. However, it is also possible to have larger pores due to the merging of several pores. In the simulation, slightly larger pores were also used to explore effects at the other extreme. The volume fraction of the pores is about 5%.
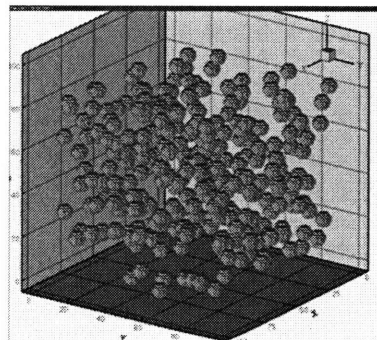
Figure 3.55: Illustration of pores in the film. The volume fraction of the pores is about 5%, and the position of the pores is randomized uniformly throughout the film.

142

Figure 3.56 shows the evolution of the porous films with different pore sizes etched at normal ion incidence, and their corresponding RMS roughness evolution is shown in Figure 3.57. The surfaces with pores are roughened faster than the surface without pores, and the larger the size of the pores, the faster the surface gets roughened. For the surface with very large pores ($r = 7.5$ nm), the resulting RMS roughness is much larger than the surface with small or no pores. It is understandable that a porous surface is roughened faster because the exposed pores contribute to the overall roughness of the surface, and this roughness is enhanced as the etching proceeds. Similar trends can be seen in the case with 45° off-normal ion incidence (Figures 3.58, 3.59). Additionally, it was observed that the ripples are less ordered for the porous films. This can be rationalized by the fact that the pores in the film cause more variations in the local etch rate. For 60° off-normal incidence, it should be recalled that the surface with no pores remained smooth independent of the amount etched. However, for porous films, the surface was roughened significantly with etching (Figure 3.60) and the RMS roughness generally increases with larger pore sizes (Figure 3.61). It can therefore be concluded in this case that the non-uniform density of the film causes enough variation in the local etch rate on the surface to initiate roughening. The surfaces etched with 75° off-normal ion incidence show similar roughening, independent of the pore sizes (Figures 3.62, 3.63). The porous surfaces etched with 85° off-normal incidence are roughened significantly, with the patterns aligned along the direction of the ion beam (Figure 3.64, 3.65). Recall that the surface without pores remained smooth when it was etched at 85° off-normal incidence with an angular distribution of scattered ions (±15°), and as mentioned before in the previous section, this is due to the fact that roughening at very grazing angles is

143

initiated by scattered ions focusing on a very localized area to form a small trench which propagates as etching proceeds. Subsequently, the dispersion of these scattered ions makes the initiation of roughening difficult. However, the porous films cause enough perturbations on the surface to initiate roughening even with the dispersion of scattered ions, and the channeling of scattered ions that ensues forms striations that are aligned with the beam direction. The RMS roughness is higher for the surface with larger pores (Figure 3.66) because they introduce greater perturbations to the surface.

In general, the non-uniformity of the film enhances the roughening of the surface. This trend is consistent with experimental measurements of roughening in the etching of non-uniform films such as porous low-k films and carbon-doped films[19]. It is therefore more challenging to exhibit control over the surface profile and minimize the amounts of roughening for these non-uniform materials.

average depth etched
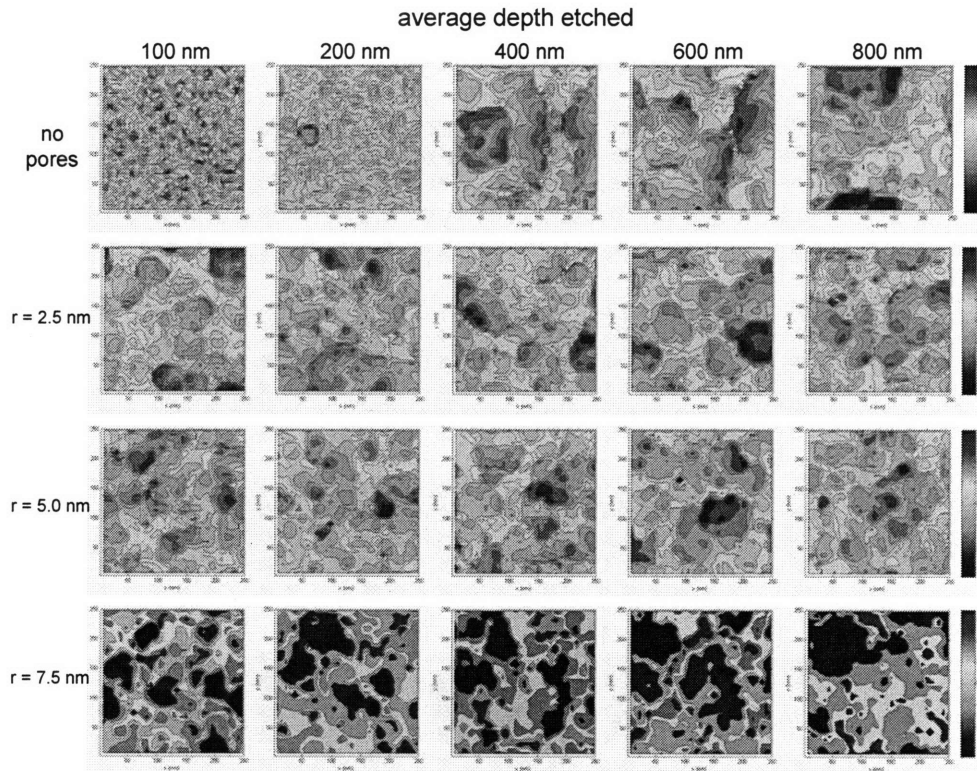
Figure 3.56: Surface with different radius of pores etched with normal ion incidence. The surfaces with pores are roughened at earlier stage of etching than the surface without pores.
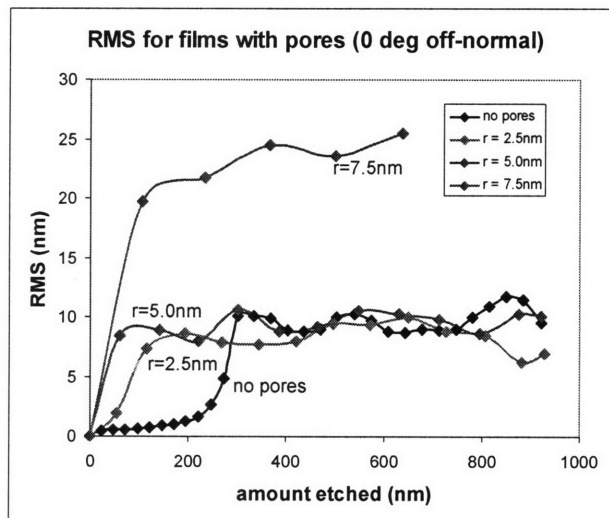
Figure 3.57: RMS roughness evolution for the films with different pore sizes etched with 0° off-normal ion incidence. For the surfaces with pores, the RMS increases at earlier stage of etching than for the surface without pores.

145

average depth etched
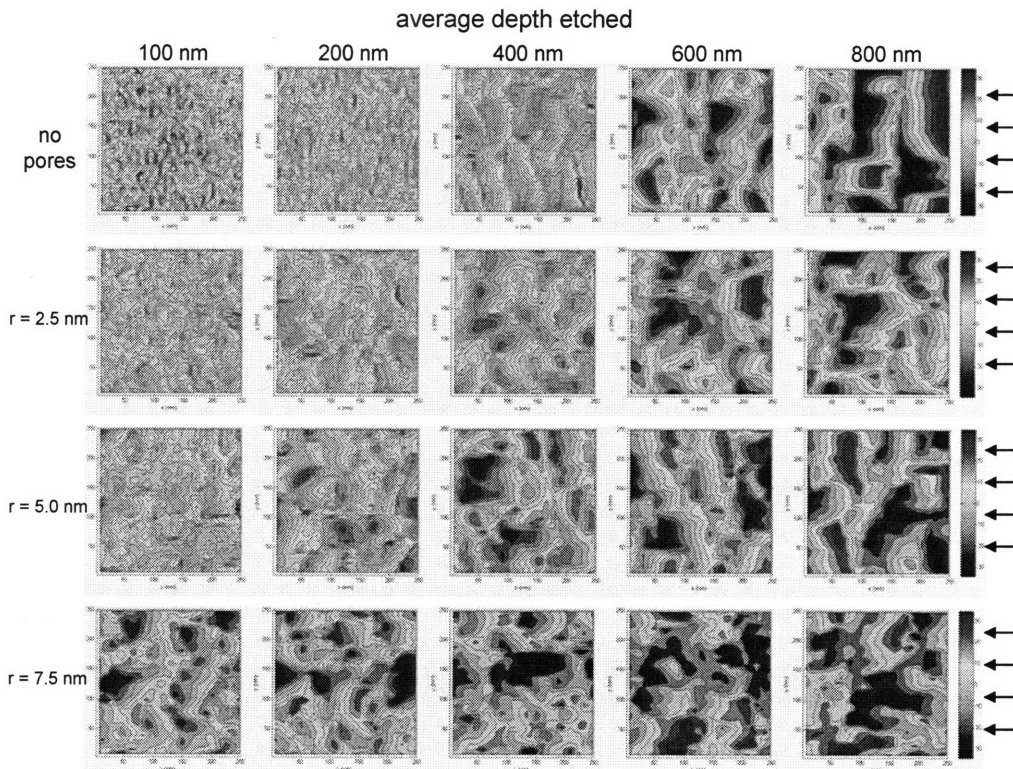
Figure 3.58: Surface with different radius of pores etched with 45° off-normal ion incidence. The surfaces with pores are roughened at an earlier stage of etching than for the surface without pores, and the larger the size of pores, the faster the surface becomes roughened. The surfaces with pores have less ordered ripples compared to the surfaces without pores.
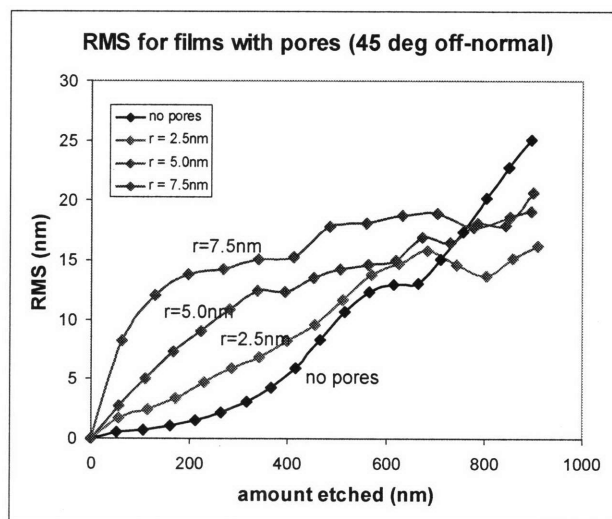
Figure 3.59: RMS roughness evolution for films with different pore sizes etched at 45° off-normal ion incidence. For the surfaces with pores, the RMS increases at an earlier stage of etching than for the surface without pores.

average depth etched
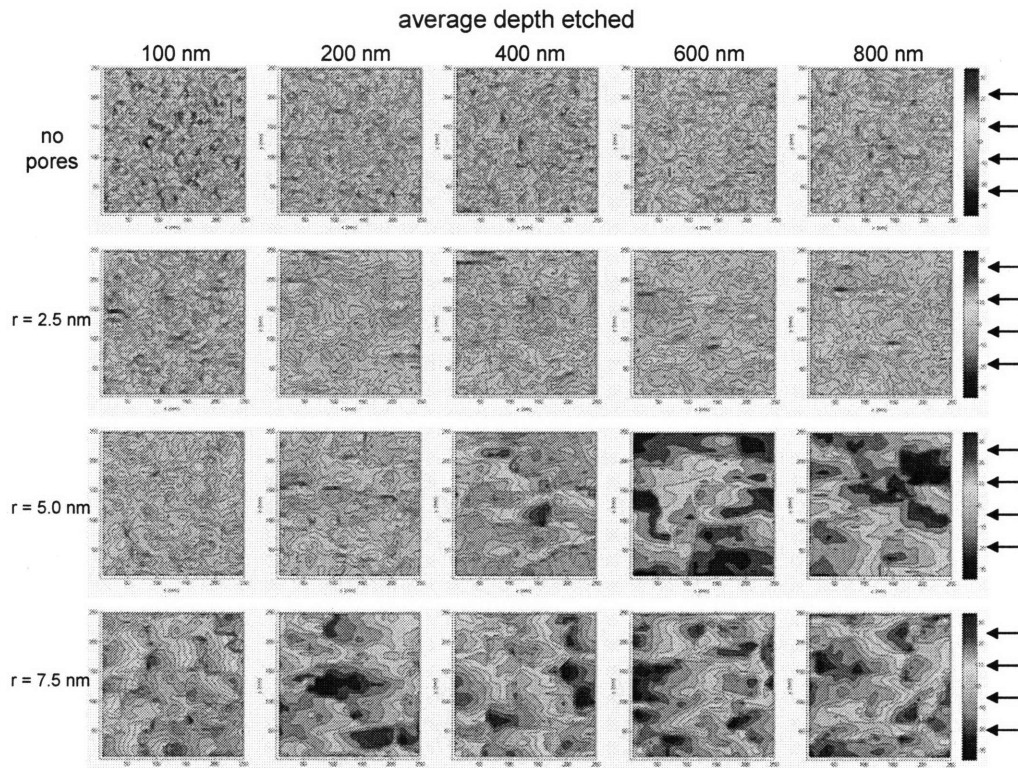
Figure 3.60: Surface with different radii of pores etched at 60° off-normal ion incidence. The surfaces with pores are roughened whereas the surfaces without pores remained smooth, and the larger the size of the pores, the more the surface was roughened.
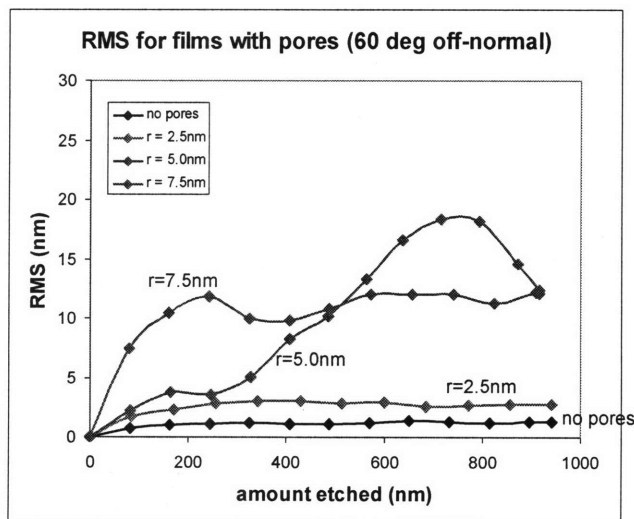
Figure 3.61: RMS roughness evolution for the films with different pore sizes etched with 60° off-normal ion incidence. The RMS is higher for the surface with larger pores.

average depth etched
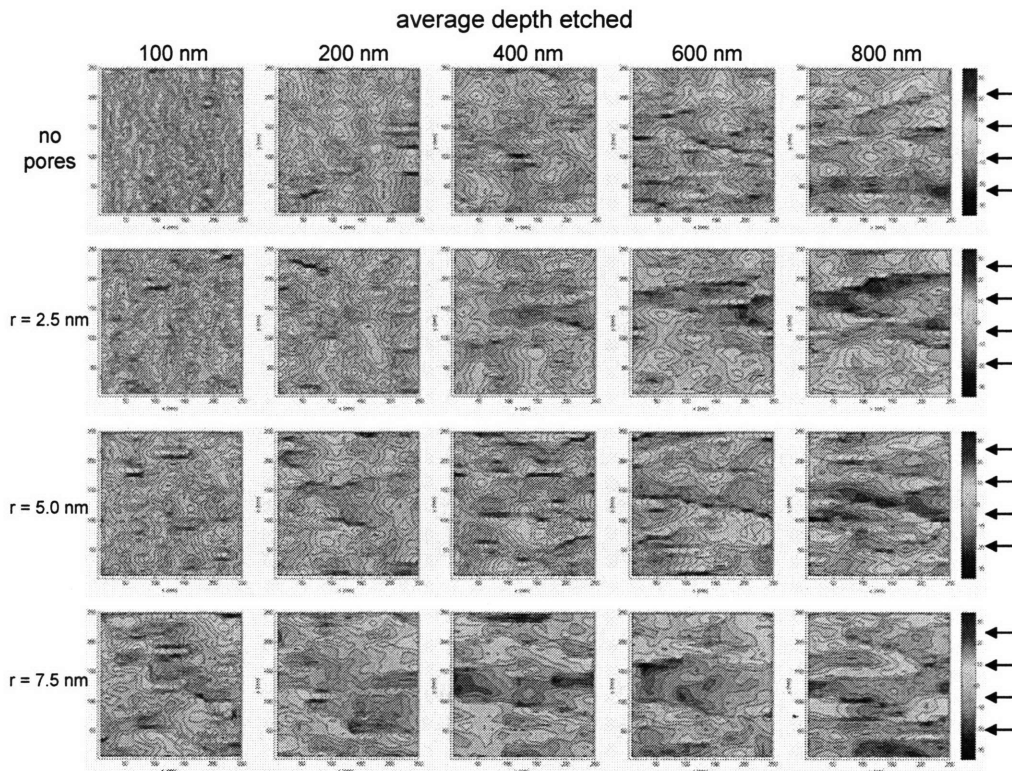
Figure 3.62: Surface with different radii of pores etched at 75° off-normal ion incidence. The roughening in all surfaces is comparable to each other.
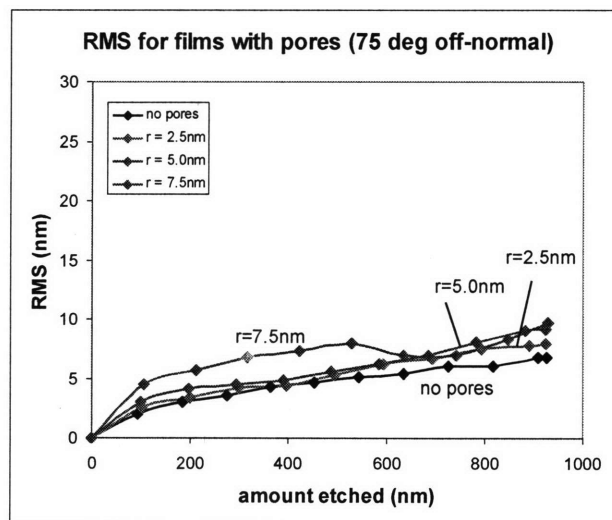
Figure 3.63: RMS roughness evolution for the films with different pore sizes etched at 75° off-normal ion incidence. There is no significant difference in the RMS values among the different surfaces.

148

average depth etched
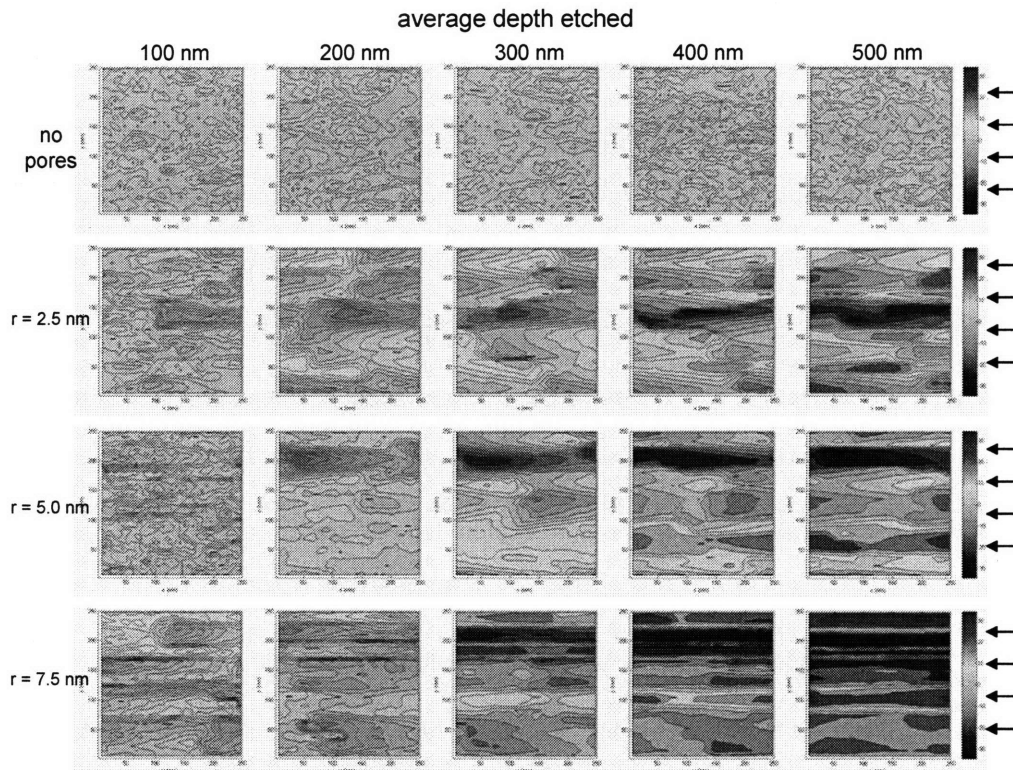
Figure 3.64:   Surface with different radius of pores etched with 85° off-normal ion incidence. The surfaces with pores are roughened, forming the patterns aligned with the ion beam direction.
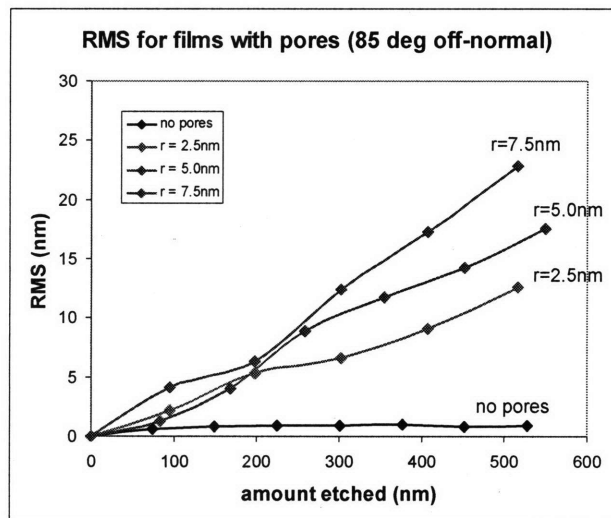
Figure 3.65:   RMS roughness evolution for the films with different pore sizes etched at 85° off-normal ion incidence. The RMS values increase significantly for the films with pores, and it is seen that the larger the pore size, the larger the increase in RMS roughness.

3.5.6. Etching of an initially roughened surface

When a perfectly flat surface is etched, the roughening of the surface is initiated by the stochastic removal of the surface atoms which creates some perturbations to the surface, and the resulting miniscule areas of roughness on the surface eventually grow to a length scale that becomes significant. What happens if the perturbations are already present on the surface? For example, some surfaces such as amorphous silicon are not atomically flat like single crystal silicon surfaces. In this section, some roughness was introduced to the surface before etching to explore the differences in surface morphology evolution when compared to a surface that is initially perfectly flat.

The pre-roughened surface was set up by introducing 200 bumps, each with a radius of 7.5 nm on a 250 x 250 nm^2 surface at random positions (Figure 3.66). The etching of this surface was simulated with different off-normal ion angles of incidence (Figure 3.67), and their corresponding RMS roughness evolution is plotted in Figures 3.68 and 3.69. The evolution of RMS roughness for the initially flat surface is also plotted for comparison. The scattered ions are assumed to have an angular distribution of ±15°.
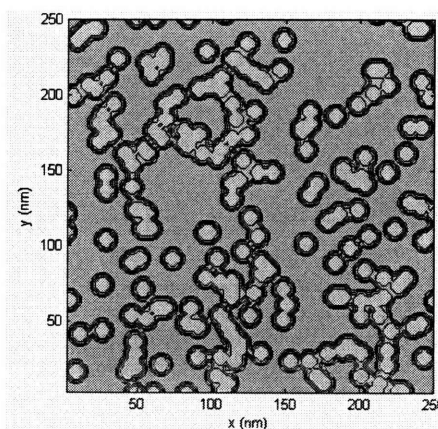
Figure 3.66: Surface with bumps on the surface. The radius of each bump is 7.5 nm.

There is no significant difference between the evolution of surface morphology for the pre-roughened and initially flat surface for each off-normal angle of ion incidence tested (Figure 3.67), except that the surface is roughened at early stage due to the initial roughness. For normal ion incidence, the RMS roughness for the pre-roughened surface increases at an early stage of etching, but saturates at an RMS roughness value similar to that of an initially flat surface (Figure 3.68). Similarly, for 45°, 60°, 75° and 85° off-normal incidence, the RMS values for the pre-roughened surface and the initially smooth surface become closer as the etching proceeds. For 60° and 85° off-normal incidence, the surface is smoothened at the beginning (i.e. RMS roughness decreases) and saturates at lower RMS values. In conclusion, these bumps alone are not enough to significantly affect the previously established transitions in surface morphology as a function of increasing off-normal incidence, and are not sufficient to initiate the roughening process for very grazing angles of ion incidence.
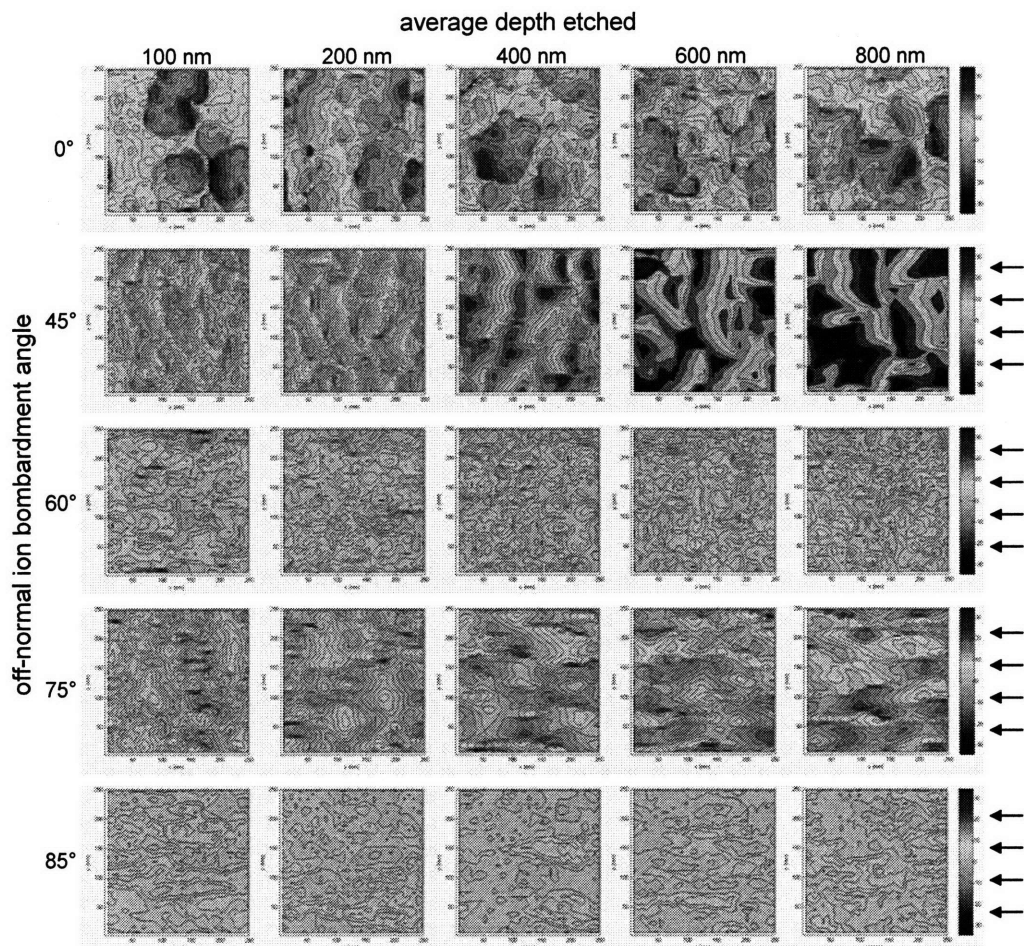
Figure 3.67: Surface with bumps etched at different off-normal ion angles of incidence. There is no significant difference in the evolution of the surface morphology between the pre-roughened and initially flat surface (see Figure 3.51), except that the surface in the case of the former is rougher at an early stage due to the initial roughness imposed.
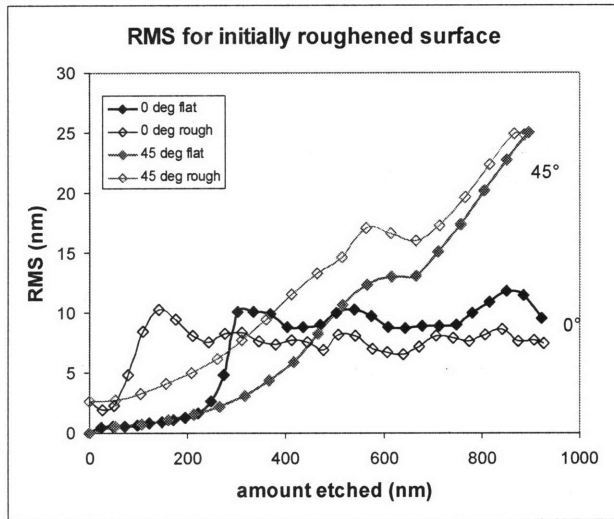
Figure 3.68: RMS roughness evolution for the initially flat and pre-roughened surfaces at 0° and 45° off-normal angles of incidence. For normal incidence, the RMS values of the initially rough surface increases at an early stage of etching, but saturates at a value similar to that of the initially flat surface. The RMS values of the initially rough surface etched at 45° off-normal incidence increases with etching at a rate similar to that of the initially flat surface, but their values converge at a later stage of etching.
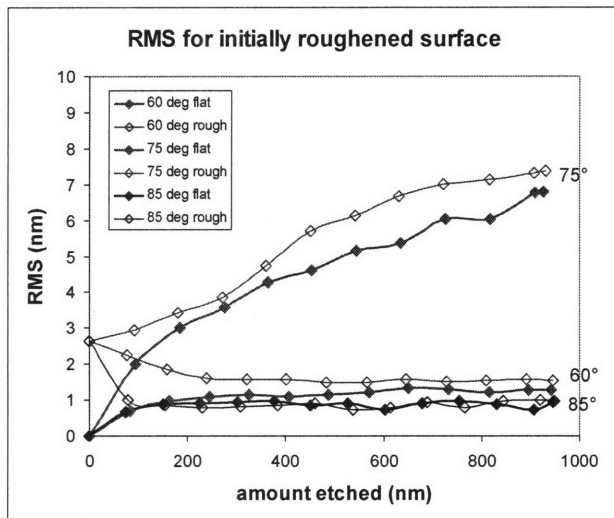
Figure 3.69: RMS roughness evolution for the initially flat and rough surfaces at 60°, 75° and 85° off-normal angles of incidence. As etching proceeds, the RMS roughness of the pre-roughened and initially flat surface approach similar values (within 10~20%).

153

3.5.7. Effects of re-deposition of sputtered particles on surface roughening

In all the previous simulation cases, the sputtered materials were assumed to leave the surface without being re-deposited onto other parts of the surface. In practice, however, some of the sputtered materials may be re-deposited and affect further etching of the surface. According to molecular dynamics (MD) simulations, the sputtered particles leave the surface close to the specular angle, with a wide angular distribution (±30~50°)[20]. The sticking probability of the etched particles may vary depending on the species and process conditions, but typical values are about 10~50 %[21]. In this section, the effect of re-deposition on surface roughening will be explored. A sticking probability of 10% was used, and the angular distribution of about ±50° was assumed for the sputtered particles. This is summarized schematically in Figure 3.70.
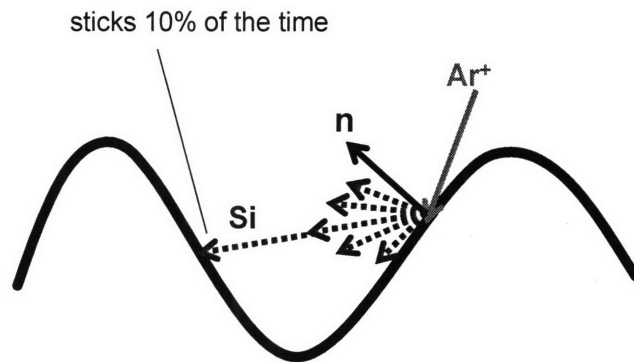
Figure 3.70: Schematic illustration of re-deposition of sputtered silicon atoms. The sputtered particles are assumed to have an angular distribution of about ±50° about the specular angle with a sticking probability of 10%.

The evolution of the surface etched at 75° off-normal incidence which includes the re-deposition mechanism is shown in Figure 3.71. The evolution of the surface without the re-deposition mechanism is also shown for comparison. The corresponding RMS roughness is plotted in Figure 3.72. At an early stage of etching, the surface morphology of the case which considers re-deposition is comparable to that of the case

154

without re-deposition. However, as the etching proceeds, the amplitude of the peaks for
the case with re-deposition becomes higher than that of the case without re-deposition.
This is also apparent from the RMS roughness plot in Figure 3.72. For the case which
accounts for re-deposition, the RMS values continue to increase drastically whereas for
the case without re-deposition, the increase in the RMS values is much slower.
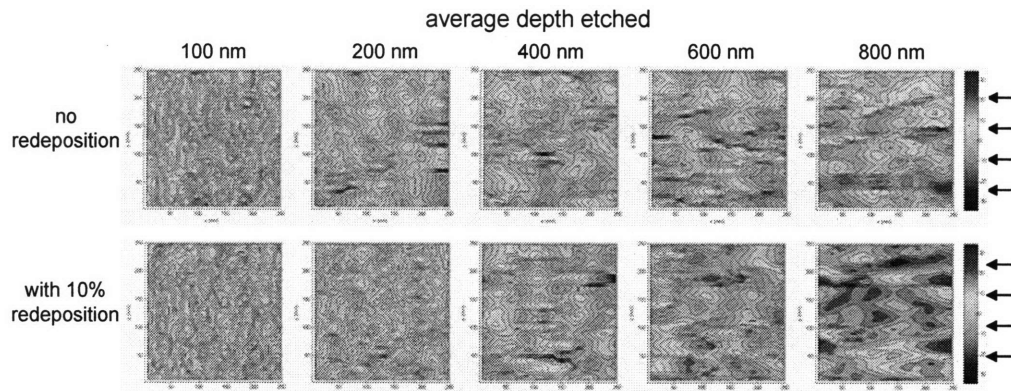
Figure 3.71: Surface etched with 75° off-normal ion incidence, with and without re-deposition. The sputtered particles are assumed to have an angular distribution of ±50°. The surfaces in the two cases have comparable features at an early stage of etching, but the amplitude of each peak in the case with re-deposition becomes larger than those in the case without re-deposition.
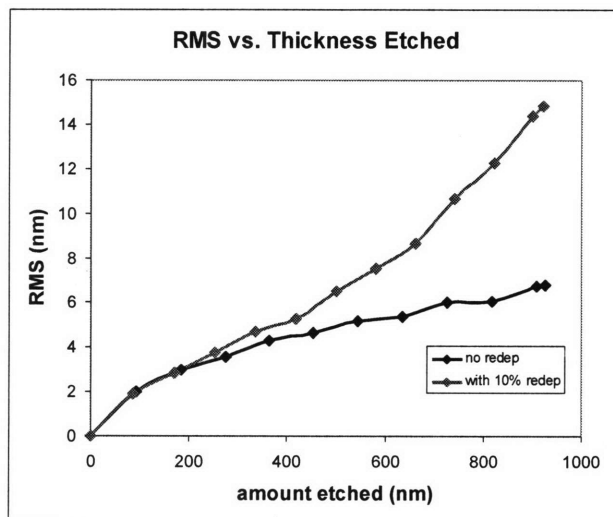
Figure 3.72: RMS roughness evolution of the surface etched with 75° off-normal incidence, with and without incorporating the re-deposition mechanism. Initially, the RMS values for the two cases are comparable to each other, but the increase in the RMS values for the case with 10% re-deposition eventually becomes more drastic compared to the case without re-deposition.

155

The re-deposition of sputtered materials affects the surface morphology only after the surface is roughened significantly because most of the sputtered material will scatter off a smooth surface without being re-deposited. If the surface is roughened, the sputtered material has a higher chance of being re-deposited because the surface features obstruct some of the scattered sputter material. This is illustrated schematically in Figure 3.73. The peaks on the surface for the case with re-deposition tend to be higher because the re-deposition of materials on the protrusions will slow down the etching of the peaks. Therefore, the re-deposition of sputtered materials enhances the roughening of the surface in etching processes.

smooth surface   roughened surface
       (a)   (b)
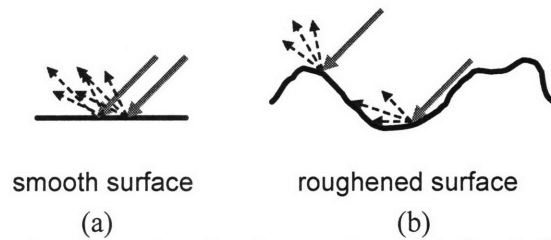
Figure 3.73: Schematic illustration of the trajectories of sputtered materials (blue dashed arrows) on smooth (a) and roughened (b) surfaces. Ion trajectories are shown by the red arrows. From geometric considerations, it is readily seen that the sputtered particles have a higher chance of being re-deposited after the surface is roughened.

3.6.   Conclusion

The sputtering of a silicon surface with argon ions was simulated. The simulator incorporated the angular and local curvature dependences on etching yield. Simulating the sputtering of a silicon surface with various off-normal angles of the argon ion beam showed that there is a significant change in its morphology with different off-normal angles of incidence. When etched at normal ion incidence, the surface becomes roughened with no preferred orientation. When etched with an off-normal ion incidence

below 50°, the surface develops ripples that are oriented perpendicular to the ion beam direction (i.e. wave vector is parallel to the ion beam). For off-normal angles of incidence between 50° and 60°, the surface remains smooth independent of the etching time. The surface is roughened again for angles of incidence above 60°, forming patterns that are aligned with the ion beam direction. These trends match qualitatively with those observed in experimental measurements. The simulation results further showed that these transitions of surface morphology with increasing off-normal angles of ion incidence are related to the angular dependence of etching yield. The angle at which each transition occurs depends on the angle at which the peak yield occurs. This correlation is very useful because the roughening of a surface can be predicted approximately from the experimentally obtained angular dependence yield curve. The effects of other factors were also investigated using the simulator, and they include the angular distribution of scattered ions, the non-uniformity of the film density, the initial roughness of the surface, and the re-deposition of sputtered materials. The analysis of the effects of each factor on surface roughening has provided great insight into understanding the roughening mechanism in the sputtering process.

3.7. References

1.   E. –H. Cirlin, Thin Solid Films **220**, 197 (1992).
2.   M. Navez, C. Sella, and D. Chaperot, Comptes Rendus **254**, 240 (1962).
3.   T. M. Mayer, E. Chason, and A. J. Howard, Journal of Applied Physics **76**, 1633 (1994).
4.   P. Sigmund, Journal of Material Science **8**, 1543 (1973).
5.   M. A. Makeev, R. Cuerno, and A. –L. Barabasi, Nuclear Instruments and Methods in Physics Research B **197**, 185 (2002).

6. R. M. Bradley and J. M. E. Harper, Journal of Vacuum Science and Technology A **6**, 2390 (1988).

7. E. Chason, T. M. Mayer, B. K. Kellerman, D. T. McIlroy, and A. J. Howard, Physical Review Letters **72**, 3040 (1994).

8. C. C. Umbach, R. L. Headrick, and K.-C. Chang, Physical Review Letters **87**, 246104 (2001).

9. M. A. Makeev and A. –L. Barabasi, Nuclear Instruments and Methods in Physics Research B **222**, 335 (2004).

10. A. Mahorowala and H. H. Sawin, Journal of Vacuum Science and Technology B **20**, 1064 (2002).

11. E. Pargon, D. Nest, and D. B. Graves, Journal of Vacuum Science and Technology B **25**, 1236 (2007).

12. B. Ziberi, F. Frost, Th. Hoche, and B. Rauschenbach, Physical Review B **72**, 235310 (2005).

13. B. Ziberi, F. Frost, and B. Rauschenbach, Journal of Vacuum Science and Technology A **24**, 1344 (2006).

14. W. L. Chan, N. Pavenayotin, and E. Chason, Physical Review B **69**, 245413 (2004).

15. U. Valbusa, C. Boragno, and F. Buatier de Mongeot, Journal of Physics: Condensed Mater **14**, 8153 (2002).

16. R. D. Kolasinski, J. E. Polk, D. Goebel, and L. K. Johnson, *American Institute of Aeronautics and Astronautics*, July 2006.

17. B. A. Helmer, and D. B. Graves, Journal of Vacuum Science and Technology A **16**, 3502 (1998).

18. V. Jousseaume, G. Rolland, D. Babonneau, and J. –P. Simon, Applied Surface Science **254**, 473 (2007).

19. Y. P. Yin, Thesis, 2007.

20. C. F. Abrams and D. B. Graves, Journal of Vacuum Science and Technology A **16**, 3006 (1998).

21. M. Tuda and K. Ono, Japanese Journal of Applied Physics, Part 1 **36**, 2482 (1997).

4. 3-D Profile Evolution of Polysilicon in Cl_2 Plasma

4.1. Introduction

The roughening of the sidewalls of etched profiles is one of the most challenging problems in integrated circuit (IC) manufacturing due to its complexity. As mentioned in chapter 1, the patterning of the film involves many etching steps, each of which may contribute to the roughness of the sidewalls of the resulting feature. Much attention has been given to the sidewall roughness formed during the lithographic processing of the photoresist film, and many experimental and simulation studies have appeared in the literature[1-3] as it is obviously critical to have a smooth photoresist mask in order to minimize the transfer of roughness to the underlying layers in subsequent etch steps. However, it is also important to explore how the consecutive etching processes affect the sidewall roughness since the device performance is ultimately determined by the profile of the final etched features. The 3-D simulation of the profile evolution is very useful in understanding the origin and evolution of sidewall roughness in etching processes. In this chapter, the evolution of sidewall roughness in the etching of patterned polysilicon in Cl_2 plasma was investigated using our 3-D Monte Carlo profile simulator. Some of the experimentally observed trends in sidewall roughening will be discussed first, followed by simulation results showing the effects of photoresist roughness on the final etched features.

4.2.   Experimental observations of sidewall roughening during etching

The evolution of the sidewall roughness during plasma etching has been measured

by Rasgon et al. using atomic force microscopy (AFM)[4,5]. Figure 4.1 shows the AFM

image of a sidewall at 4 stages of the etching process: (1) After photoresist development

(before etching); (2) After etching of the anti-reflective coating (ARC) layer; (3) After

etching 0.2 μm of the SiO_2 layer; and (4) After etching 0.5 μm of the SiO_2 layer. After

the photoresist was developed as shown in (1), the sidewall of the photoresist has an

isotropic roughness with an average RMS value of ~3-5 nm. After the ARC layer is

opened (2), the morphology of the sidewall is transformed from isotropic to anisotropic

roughness with mild striations along the sidewall surface. High points on the sidewall

were washed away due to the anisotropic bombardment. After etching 0.2 μm of the

oxide layer (3), the top of the remaining resist is heavily roughened, but the oxide

sidewall remains relatively smooth. After etching 0.5 μm of oxide, the top of the resist is

roughened further, and the roughness is also transferred to the ARC and oxide layers,

forming severe anisotropic striations along the sidewalls of the oxide. These data show

that the roughness on the sidewalls of the final feature is not a result of simple

transferring (or templating) of the initial roughness of the photoresist sidewall to the

underlying layer. Instead, the photoresist sidewall is heavily roughened by the ion

bombardment throughout the etching process, and the sidewall roughness is eventually

spread to the underlying layers. The surface profile (i.e. cross-section of the surface) at

different locations along the sidewall is shown in Figure 4.2. The amplitude is highest at

the top of the resist, and decreases with distance from the top. Note that some of the

ripples at the sidewalls of the photoresist are spatially correlated with the ripples at lower

parts of the sidewall. This drop in amplitude is also apparent from the RMS roughness plotted against location on the sidewall in Figure 4.3. These measurements were made for the etching of SiO_2, but very similar trends have been observed for the etching of silicon[6].

1) Sidewall AFM image after development
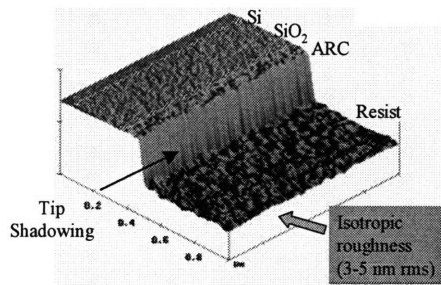
2) Sidewall AFM image after N2 – H2 organic ARC open
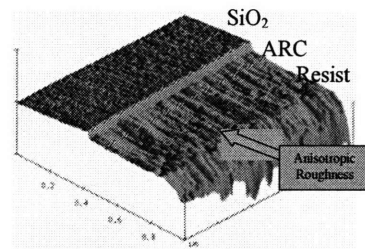
3) Sidewall AFM image after 45s (0.2μm) oxide etch
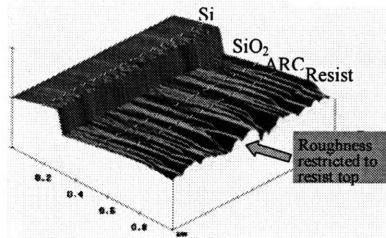
4) Sidewall AFM image after 90s (0.5μm) oxide etch
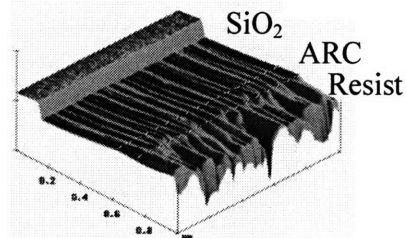
Figure 4.1: AFM images of sidewall at 4 steps in the etching of patterned SiO_2. Photoresist sidewall has an isotropic roughness after development. The morphology of the sidewall changes from isotropic to anisotropic roughness after etching ARC layer. As the SiO_2 layer is etched, the photoresist layer is further roughened and severe anisotropic striations are formed along the sidewall. (Ref. 4, 5)
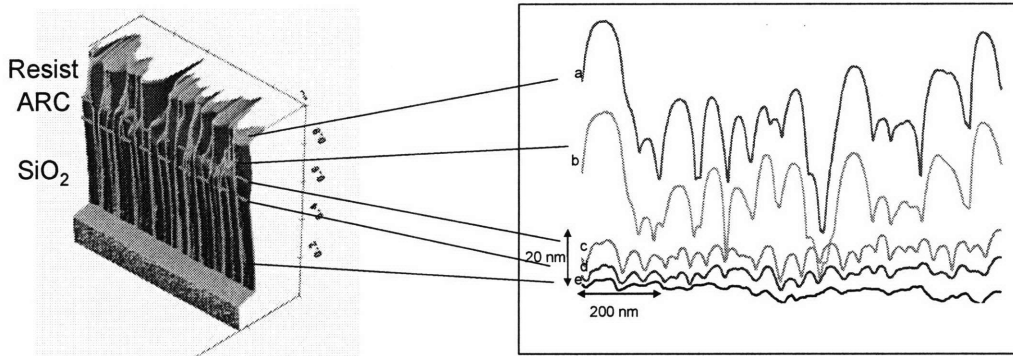
Figure 4.2: Surface profiles at different locations along the sidewall after etching 0.5 μm of oxide. (a) Near the top of the resist, (b) in the middle of the resist, (c) at the interface of resist and ARC, (d) at the interface of ARC and oxide, (e) near the bottom of the oxide. The amplitude of striations decreases with depth. (Ref. 5, 6)
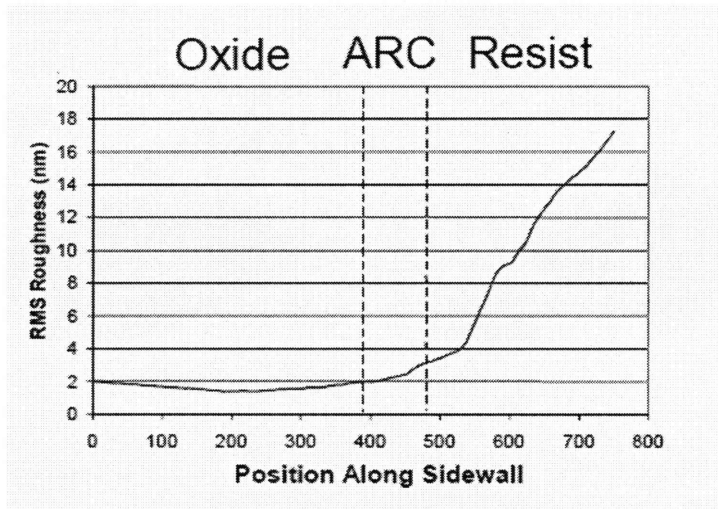
Figure 4.3: RMS roughness on the sidewall at different position along sidewall after etching 0.5 μm of oxide. The RMS is highest at the top of the resist, and it decreases with depth.

4.3. 3-D simulation of profile and sidewall roughness evolution of patterned polysilicon etched in Cl_2 plasma

Our developed 3-D Monte Carlo simulator was used to investigate the evolution of the feature profiles and sidewall roughness during the etching of patterned polysilicon in Cl_2 plasma. The assumptions made in the simulation will first be described, followed

by a discussion of simulation results which is focused on the effects of photoresist sidewall morphology on the sidewall roughness of final etched features.

4.3.1. Model assumptions

A stack of photoresist, ARC and polysilicon (Figure 4.4) was introduced as an initial feature. The dimensions and geometry of the feature is shown in Figure 4.5. The simulation domain has a periodic boundary condition on each side, thus representing the pattern with infinite photoresist lines and spaces. Two etch steps were simulated: ARC opening and polysilicon etching. The ARC layer was etched by O_2 plasma, and its etching characteristic was assumed to follow the angular dependence of sputtering (peak yield at 65°) shown in Figure 4.6. The selectivity of the ARC etch over that of the photoresist was assumed to be very low, i.e. the photoresist was etched at an equal rate with the ARC layer during ARC opening. The photoresist etching also followed the angular dependence of sputtering. The ARC layer was etched until the polysilicon layer was exposed. The selectivity of ARC etch over polysilicon during ARC opening was assumed to be infinity, i.e. polysilicon was not etched during the ARC opening step. The etching of the underlying polysilicon substrate commenced only after it became exposed. Polysilicon was etched by Cl_2 plasma, where the etch characteristics follow the angular dependence of Cl_2 ion-enhanced etching and is different from sputtering, as shown in Figure 4.6. Chlorine ions can also etch photoresist, ARC as well as polysilicon. The selectivity of polysilicon over photoresist and ARC was assumed to be 9 to 1. The re-deposition of etch products was ignored unless mentioned.

163
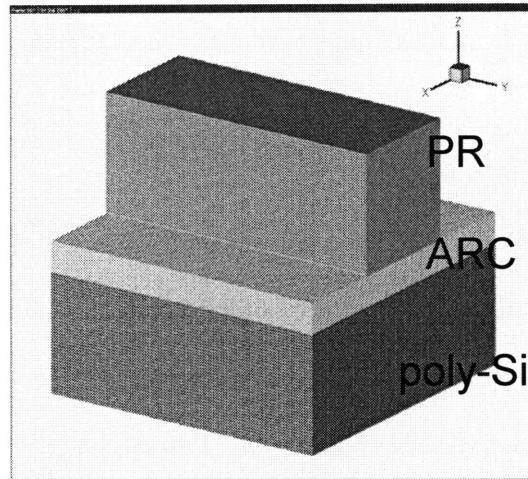
Figure 4.4: The stack of photoresist, ARC and polysilicon was used as an initial feature in simulation. Cells are attributed to different materials.
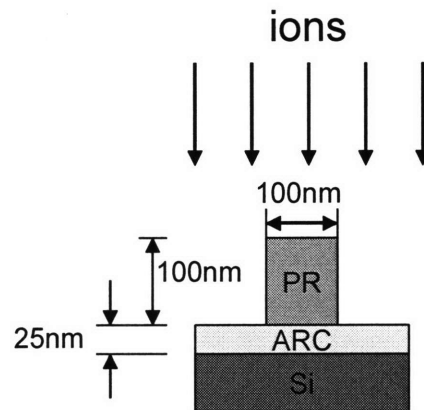
Figure 4.5: Dimension of the initial feature in simulation. The thickness of photoresist and ARC layers are 100 nm and 25 nm, respectively.

Etching yield vs. angle of ion incidence
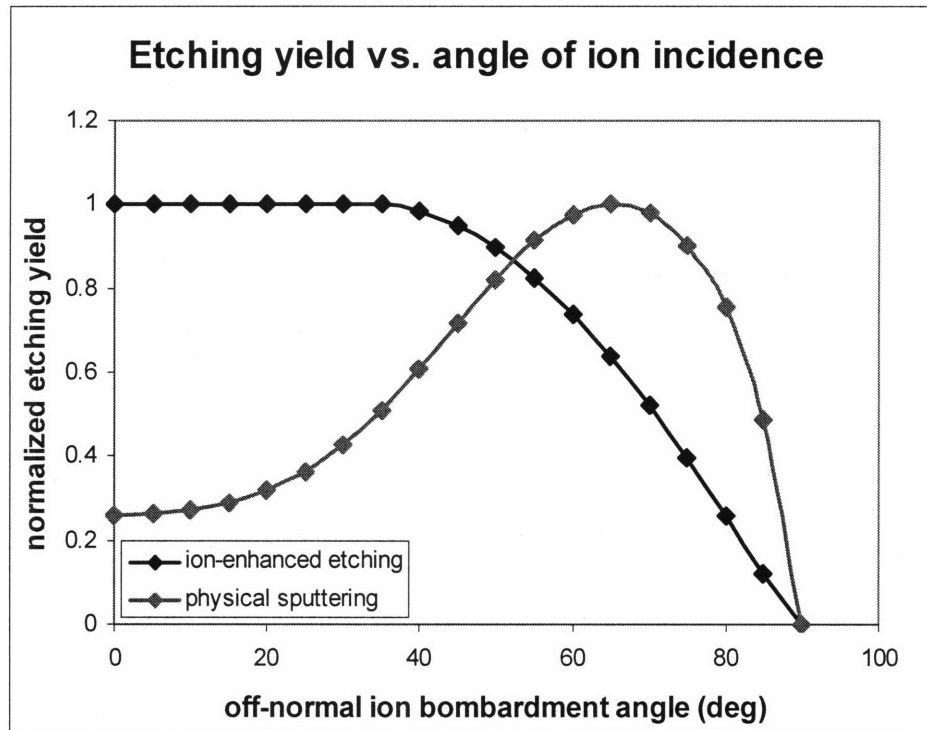
Figure 4.6: Angular dependence of ion-enhanced etching and physical sputtering. The etching of photoresist and ARC follows the angular dependence of physical sputtering, and the etching of polysilicon follows that of ion-enhanced etching.

4.3.2. Roughening of the sidewall: Perfectly smooth photoresist

The etching of ARC and polysilicon was simulated, assuming that the sidewalls of the photoresist before the ARC etch are perfectly flat and vertical (Figure 4.7a). In Figure 4.7, the feature profiles at 3 etch steps are shown. After ARC-open, the photoresist sidewall is tapered, but does not have any apparent streaks. After etching about 50 nm of polysilicon, small height variations on the sidewall as well as the bottom of the feature can be observed, though the sidewalls in general remained relatively smooth. Figure 4.8 shows the surface profile at 3 locations along the sidewall: (1) in the middle of the photoresist, (2) at the ARC layer and (3) at the bottom of the polysilicon sidewall. The amplitude of the roughness is within 3 nm at all these locations. The RMS

165

roughness plotted against the depth (Figure 4.9) also shows that the sidewall roughness is very small, with an RMS value less than 2 nm. This result is consistent with the fact that photoresist sidewalls which are smooth minimize the resulting sidewall roughness of etched features.

| (a) | (b) | (c) |
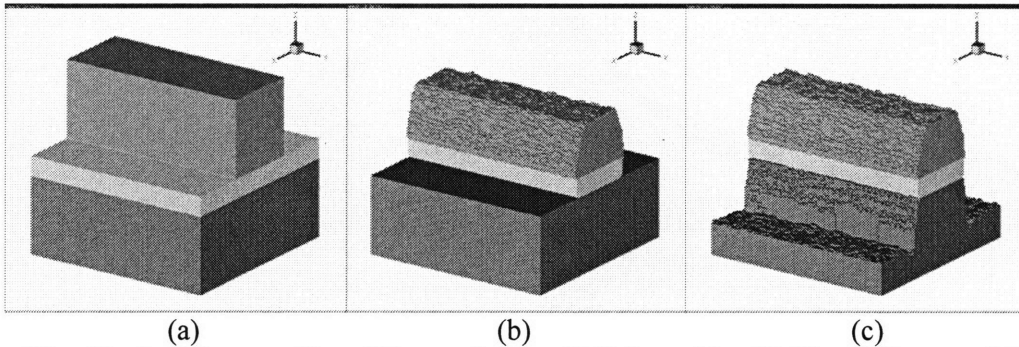
Figure 4.7: Simulated feature profile at different etch steps. (a) Before etching, (b) After ARC open, and (c) After etching 50 nm of polysilicon. The sidewall of the photoresist before ARC open was assumed to be perfectly flat and vertical. The sidewall remains relatively smooth.

Figure 4.8: Surface profiles at different locations along the sidewall after etching 50 nm of polysilicon. (1) In the middle of the photoresist, (2) at the ARC layer and (3) at the bottom of the polysilicon sidewall. The amplitude of sidewall roughness remains within 3 nm for all locations.
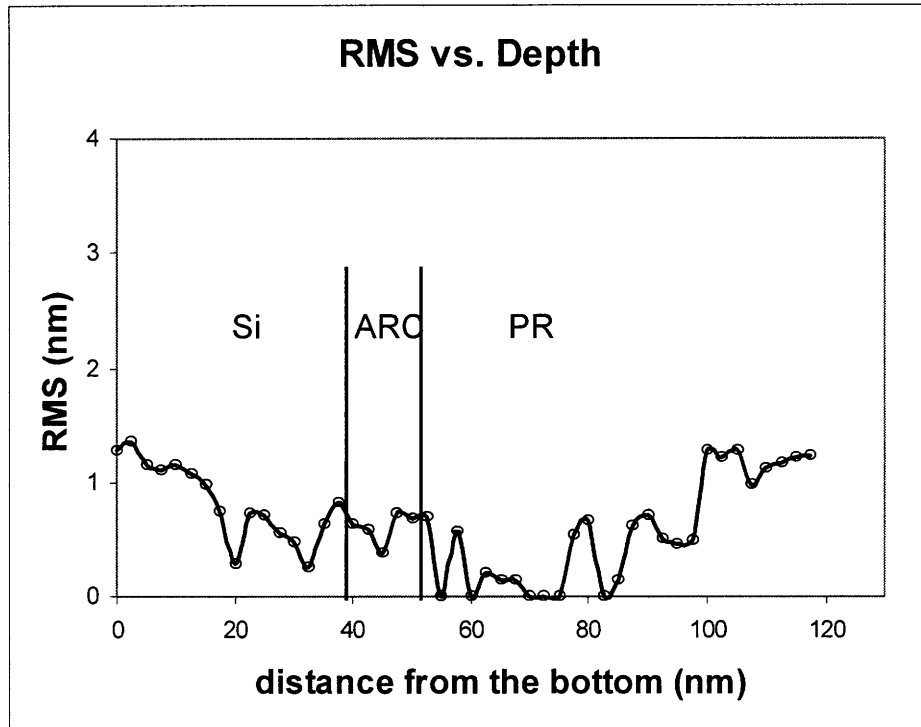
Figure 4.9: RMS roughness as a function of depth. At all layers, the RMS of the sidewall remains less than 2 nm.

The cross-section of the profile is shown in Figure 4.10 to show some of the common etch artifacts seen in the etching of polysilicon in Cl_2 plasma. The corner of the photoresist formed a facet due to the characteristic angular dependence of the sputtering yield. The facet angle is about 67°, which is approximately equal to the angle of peak yield in sputtering (65°). This makes sense because the most rapid surface advancement occurs at this angle. The slight bowing of polysilicon sidewall and the formation of microtrenches at the foot of the sidewall are caused by the angular dependence of ion-enhanced etching yield of polysilicon in Cl_2. The ions scattered from the bowed sidewall and from the faceted photoresist are focused at the foot of the sidewall to form microtrenches. This is shown schematically in Figure 4.11. These features are consistent

with the etch artifacts commonly observed experimentally in the etching of polysilicon in

Cl_2 plasma, as mentioned in chapter 1.
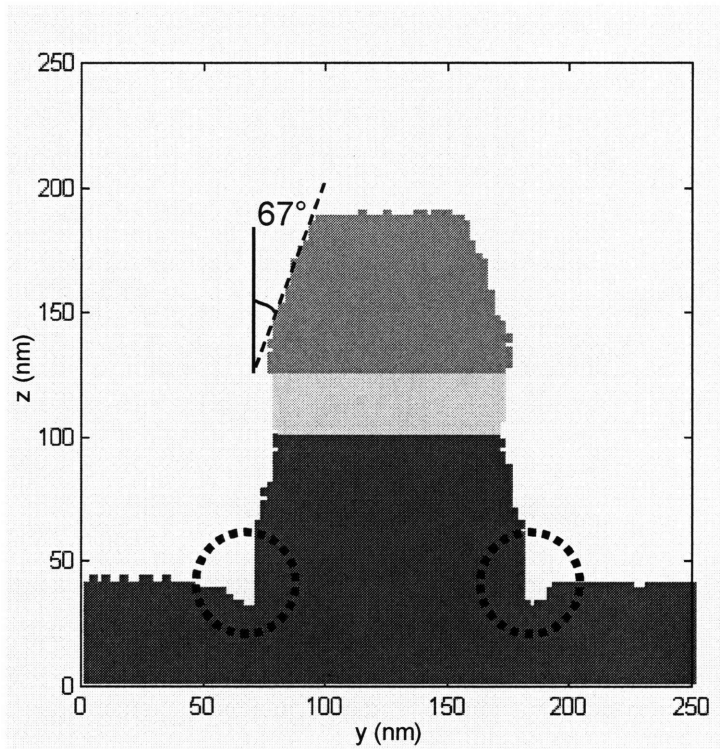
Figure 4.10: Feature profile of the polysilicon etched in Cl_2 plasma. Etch artifacts, including the faceting of photoresist, sidewall bowing and microtrenching, commonly observed in the experiments are captured by the simulation.
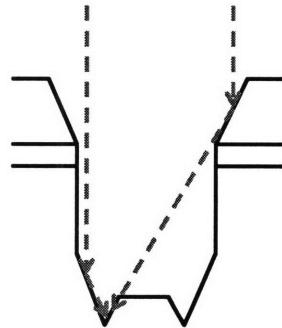
Figure 4.11: Schematic illustration of the formation of microtrenches. The ions scattered from the bowed sidewall and faceted photoresist are focused at the foot of the sidewall, forming microtrenches.

4.3.3. Roughening of the sidewall: Photoresist with initial roughness

In the previous section, it was seen that the overall sidewall remains relatively smooth when the sidewall of the photoresist layer is perfectly smooth before the etching of the ARC and polysilicon substrate. However, as mentioned in section 4.2, this is not the case in reality. The sidewall of the photoresist after development has an isotropic roughness with a RMS value of about 3 to 5 nm. In this section, the effect of photoresist roughness on the final sidewall roughness of the etched feature will be explored.

The roughness on the photoresist sidewall was introduced by placing some bumps with the radius of about 7 nm (RMS of about 3 nm), as shown in Figure 4.12a. The ARC layer and polysilicon substrate were allowed to be etched, and their corresponding profiles are shown in Figure 4.12b and c. The general characteristics of the etched feature, such as faceting of the photoresist and microtrenching at the bottom of the sidewall, are comparable to those obtained from the case of a perfectly smooth photoresist as shown in the previous section. The bumps on the sidewall are washed away during ARC-open, but the resulting sidewall of the etched feature is not the same as the case without bumps. The amplitude of the sidewall roughness at the photoresist layer is about 8 nm, which is larger than that for the feature starting from the perfectly smooth photoresist. The RMS roughness of the sidewall as a function of depth is plotted in Figure 4.14, together with the RMS of the sidewall for the feature starting from the perfectly smooth photoresist. At the photoresist and ARC layers, the RMS roughness is much higher for the case starting from the rough photoresist than for the case with smooth photoresist. Some of the sidewall roughness is transferred to the underlying ARC layer as well as to the polysilicon layer close to the ARC/polysilicon interface. The

bottom of the polysilicon sidewall still remains relatively smooth. Although the roughening of the photoresist is not as heavy as the experimentally measured roughness, the trend that the RMS roughness drops with the depth along the sidewall is consistent with experimental observation (see section 4.2).

(a)   (b)   (c)

Figure 4.12:   Simulated feature profile at different etch steps for the rough photoresist mask. (a) Before etching, (b) After ARC open, and (c) After etching 50 nm of polysilicon. Some bumps with the radius of 7 nm were placed on the sidewall of the photoresist before ARC-open to introduce isotropic roughness. The bumps are washed away during the ARC-open step, but some of the roughness is transferred to the underlying ARC and polysilicon layers.
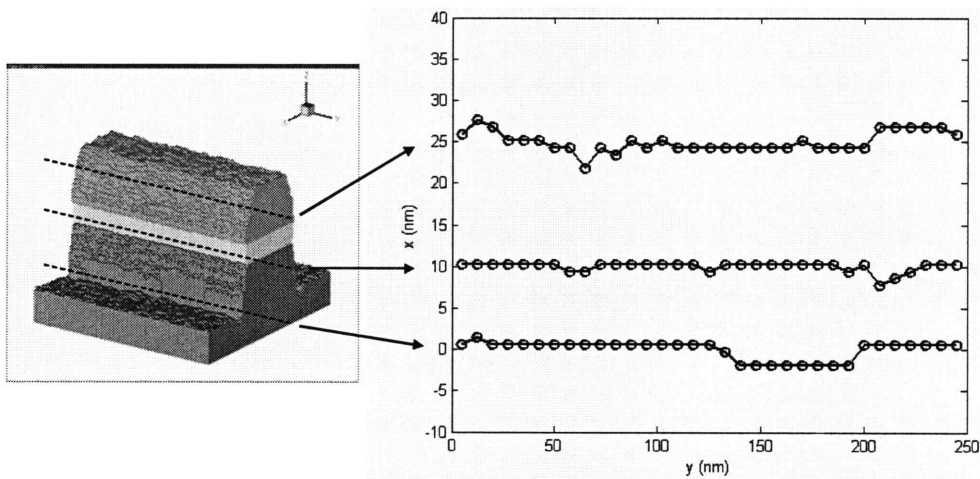

Figure 4.13:   Surface profiles at different locations along the sidewall after etching 50 nm of polysilicon. (1) In the middle of the photoresist, (2) at the ARC layer and (3) at the bottom of the polysilicon sidewall. The amplitude is largest at the photoresist mask, upto 8 nm.
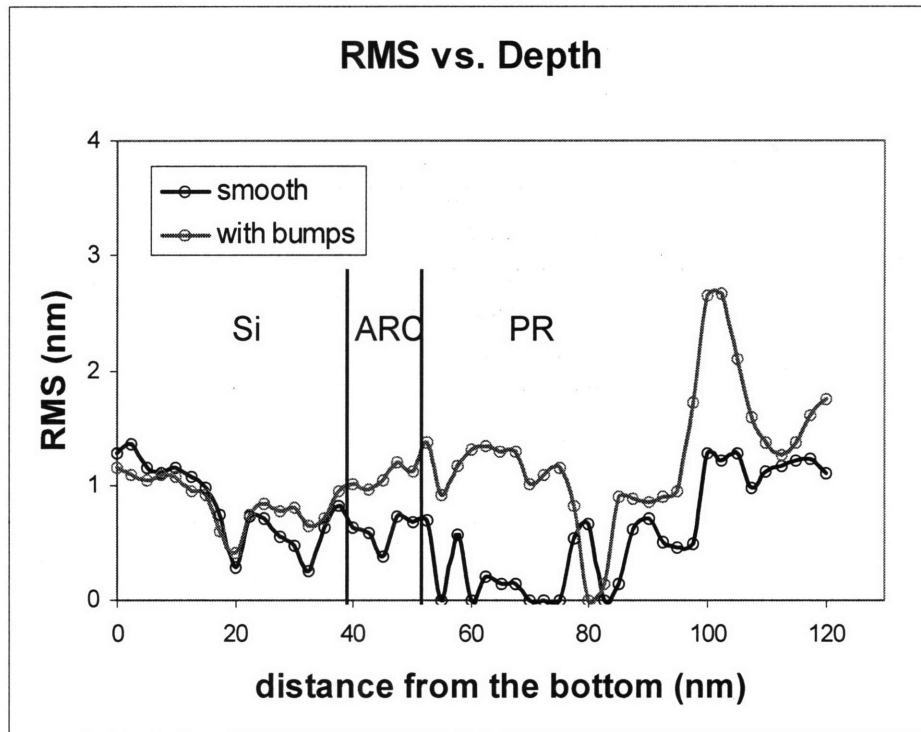
Figure 4.14: RMS roughness as a function of depth for smooth photoresist and photoresist with bumps on the sidewall. RMS of the sidewall is larger for the photoresist with bumps on the sidewall than for the smooth photoresist.

4.3.4. Roughening of the sidewall: Photoresist with slight wiggling

Depending on the process conditions, the photoresist mask may have some wiggling after development. For example, some photoresists may be heat sensitive and become thin at high thermal heat, and this non-uniform slimming leads to the collapse of photoresist in random directions[7]. The top-down view of an example of photoresist wiggling in a nitride etching is shown in Figure 4.16. The bottom of the photoresist remains straight, but the top of the photoresist is tilted to the left or right, causing the photoresist wall to be non-vertical.
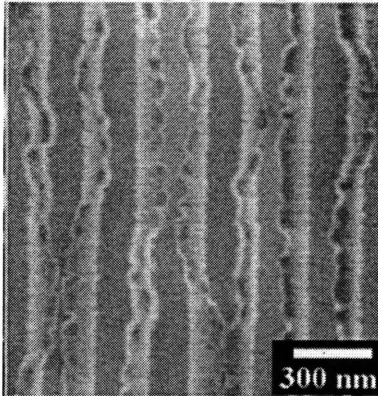
Figure 4.15: Top-down view of wiggling of photoresist. The slimming of the photoresist by thermal heat causes it to collapse in random directions.

The effect of wiggling of photoresist on subsequent etching was examined in the simulation. The dimension of wiggling of photoresist in the simulation is shown in Figure 4.16. The wavelength and amplitude of the wiggling were assumed to be about 170 nm and 45 nm, respectively. The mask was tilted to either side, with maximum angle of 83°. The wiggling introduced in the simulation is not as extreme as in the experimental observation, but as shown in Figure 4.17, this small wiggling is enough to cause severe sidewall roughness of the etched feature. After the ARC layer is etched, some of the wiggling disappears because of the faceting of the photoresist corners. However, the waviness of the photoresist is transferred to the ARC layer as well as to the polysilicon sidewall in subsequent etching steps. The surface plot at each location on the sidewall shows that the striations on the polysilicon and ARC layers are spatially correlated with the striation at the photoresist layer, which is consistent with the trends observed experimentally.

172
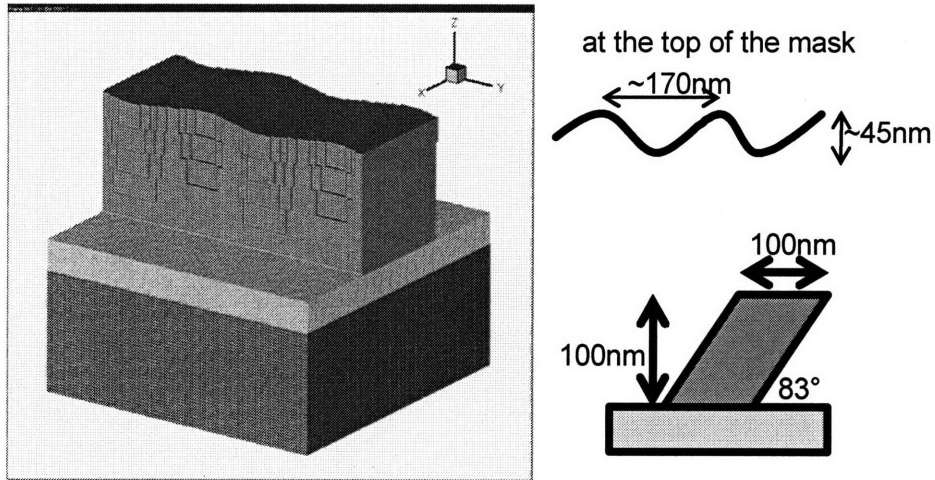
Figure 4.16: The initial feature with wiggling of photoresist. The photoresist was assumed to have a wiggling with the wavelength and amplitude of about 170 nm and 45 nm, respectively. The mask angle was assumed to be up to 83°.
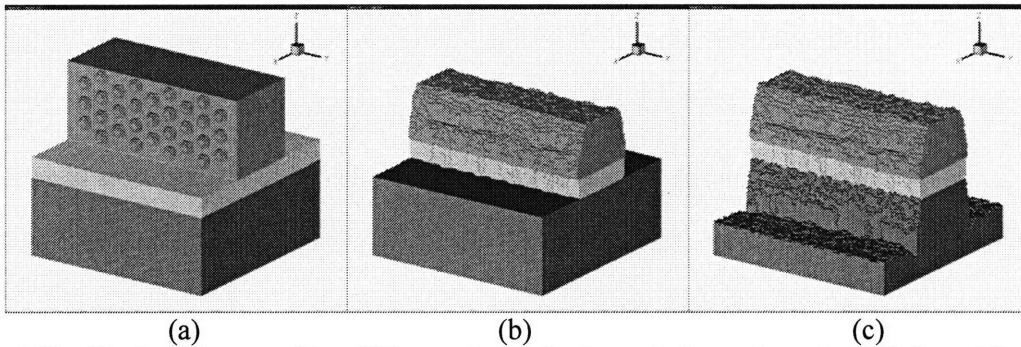

(a)   (b)   (c)
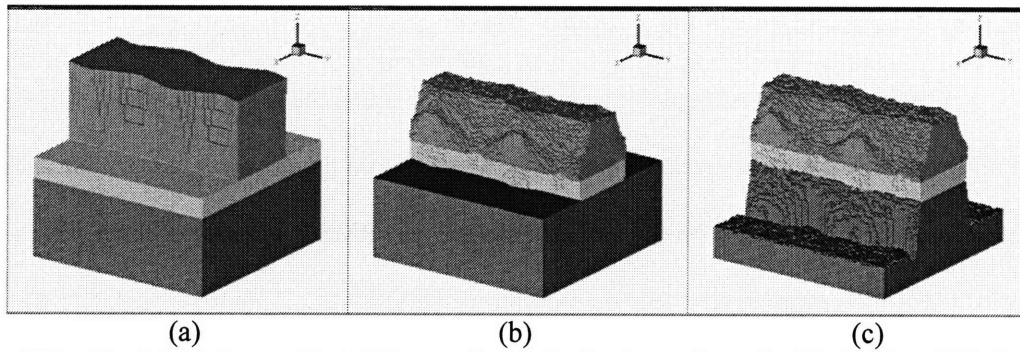
Figure 4.17: Simulated feature profile at different etch steps for the photoresist mask with wiggling. (a) Before etching, (b) After ARC open, and (c) After etching 50 nm of polysilicon. After ARC open, some of the wiggling of the photoresist disappears due to faceting of the corners, but waviness of the photoresist layer is transferred to the ARC layer and also to polysilicon sidewall during the subsequent etching.
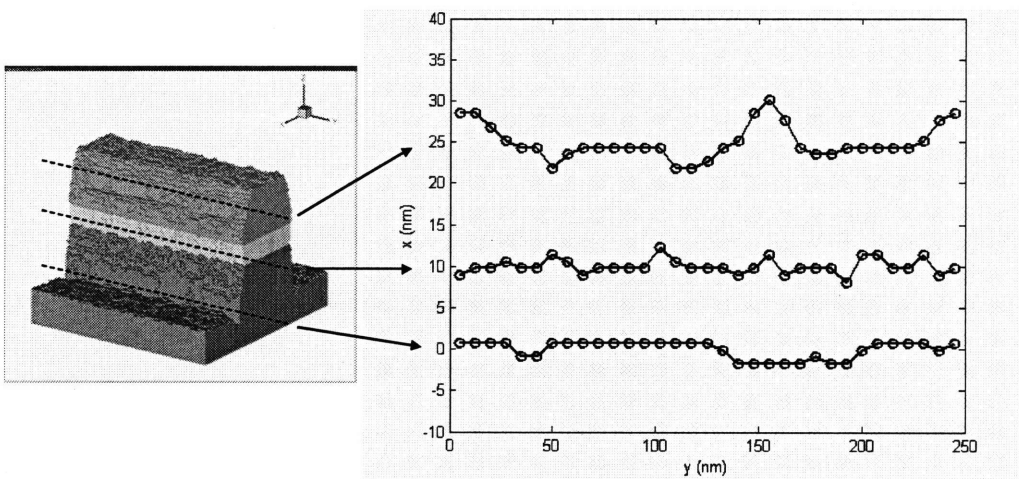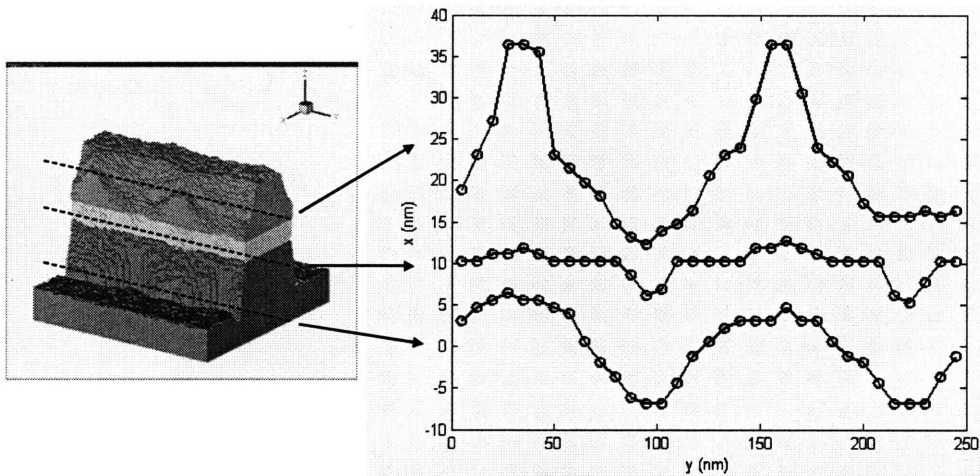
Figure 4.18: Surface profiles at different locations along the sidewall after etching 50 nm of polysilicon. (1) In the middle of the photoresist, (2) at the ARC layer and (3) at the bottom of the polysilicon sidewall. The amplitude is largest at the photoresist mask, up to 24 nm. The roughness on the photoresist is transferred down to ARC and polysilicon layers during etching.

The RMS roughness is plotted against the depth along the sidewall in Figure 4.19. At all locations along the sidewall, the RMS value is more than 3 times larger than the RMS obtained in the case with the smooth photoresist. RMS roughness decreases with depth, but it increases slightly near the bottom of the sidewall. This may be due to the variation in sidewall bowing in the polysilicon layer caused by severe roughening on the sidewall. The resulting sidewall roughness in experimental measurements may be more severe because the wiggling is more extreme compared to the wiggling introduced in the simulation. The simulation results confirmed that the small deviation from flat and vertical mask causes significant roughening of the sidewall in subsequent etching steps.
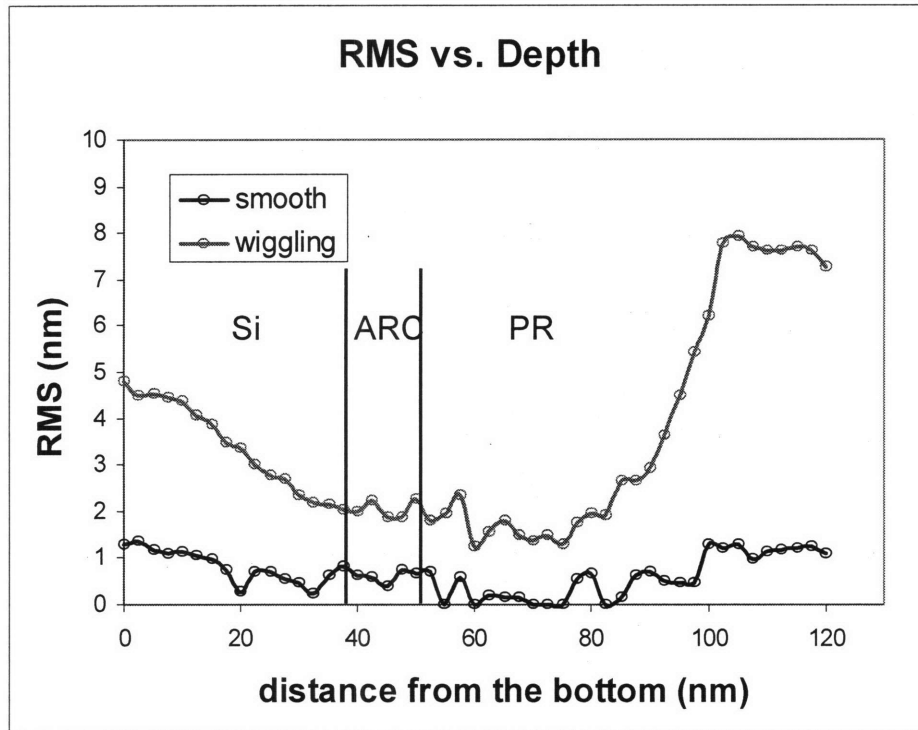
Figure 4.19: RMS roughness as a function of depth for smooth photoresist and photoresist with wiggling. RMS of the sidewall is larger for the photoresist with wiggling than for the smooth photoresist.

4.3.5. Roughening of the sidewall: Effects of redeposition of sputtered photoresist

In the previous cases, the redeposition of sputtered photoresist materials was ignored for simplicity. In this section, the effect of redeposition of photoresist materials during ARC open on sidewall roughening will be explored. It was assumed that the photoresist and ARC are composed of same material (carbon only), and the redeposition of photoresist material on ARC will affect the etching rate of the redeposited surface but not change the angular dependence of etching yield. The sputtered particles were assumed to have about ±5° angular distribution about the specular angle. The sticking probability of sputtered particles was assumed to be 40%. The schematic illustration of the redeposition of sputtered particles is shown in Figure 4.20. The redeposition of

photoresist during polysilicon etching was ignored to avoid the mixed composition of carbon and silicon for simplicity. This assumption is reasonable because the selectivity of silicon over photoresist and ARC is high, and therefore the sputtering of photoresist during polysilicon etch is not significant.
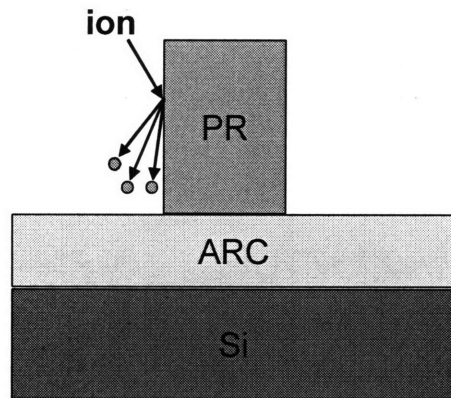
Figure 4.20: Schematic illustration of the redeposition of sputtered photoresist materials on ARC surface. The sputtered photoresist materials were assumed to have ±5° distribution about the specular angle and 40% sticking probability.

The initial feature was assumed to have a perfectly smooth and vertical photoresist, as shown in Figure 4.21a. After ARC open, the sidewall of the ARC layer is covered by photoresist materials. This is because the ions strike the photoresist at very grazing angle, and the sputtered particles will leave the surface at very grazing angle as well, reaching the sidewall of the ARC layer. The redeposition of the particles causes more variation in photoresist and ARC sidewall topography, and this variation affects the subsequent polysilicon etching. The surface profiles in Figure 4.22 show that the amplitude of roughness is largest at photoresist layer (~10 nm), and the amplitude and wavelength decrease with depth, which is similar to the trend observed in the previous cases. However, as shown in Figure 4.23, the RMS roughness is slightly higher than the

case with smooth photoresist for most part of the sidewall. Therefore, in general, the

redeposition of photoresist enhances the sidewall roughness.

(a)   (b)   (c)
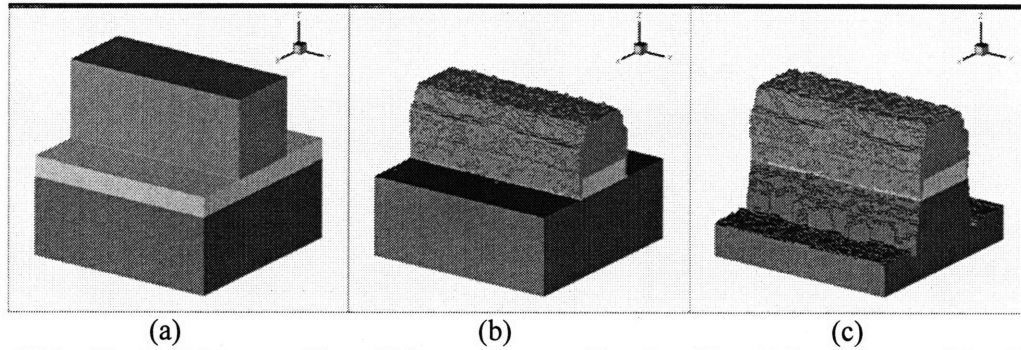
Figure 4.21: Simulated feature profile at different etch steps with redeposition of photoresist materials. (a) Before etching, (b) After ARC open, and (c) After etching 50 nm of polysilicon. After ARC open, the ARC sidewall is covered with photoresist materials. The redeposition causes more variations in the sidewall topography, enhancing the sidewall roughness.
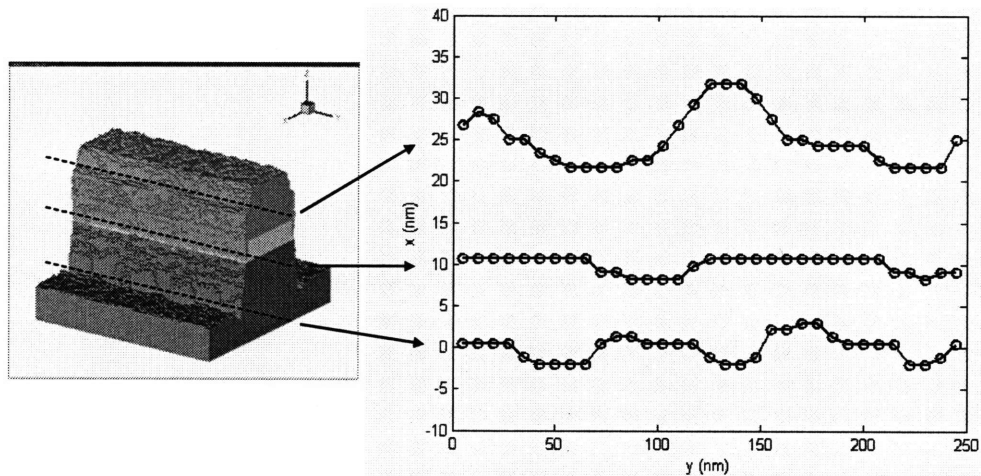
Figure 4.22: Surface profiles at different locations along the sidewall after etching 50 nm of polysilicon. (1) In the middle of the photoresist, (2) at the ARC layer and (3) at the bottom of the polysilicon sidewall. The amplitude is largest at the photoresist mask, up to 10 nm. The amplitude and wavelength of the roughness decrease with depth.

177
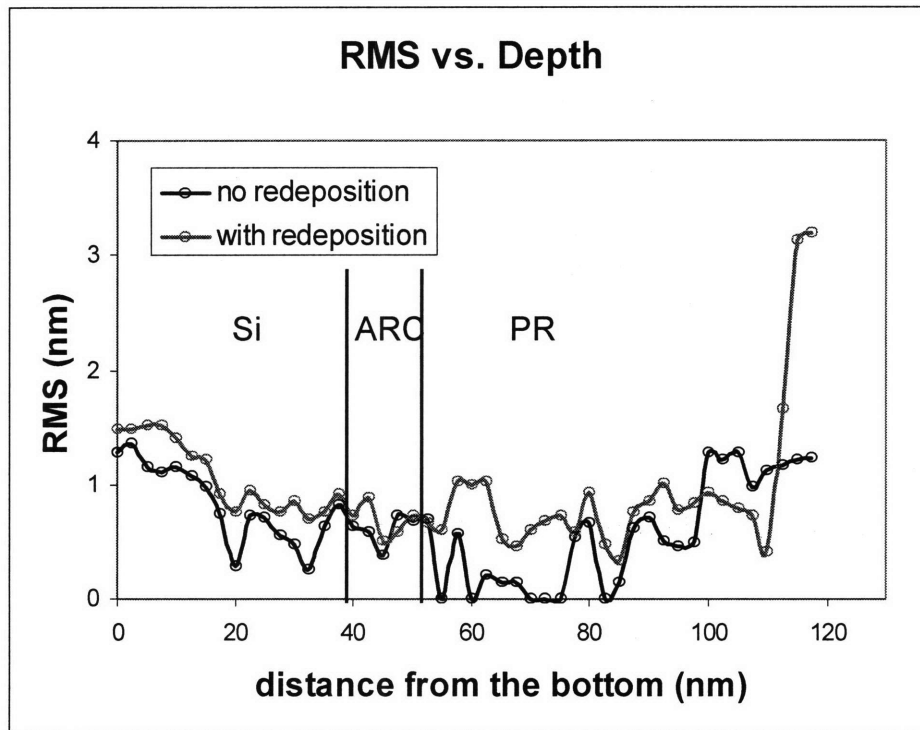
Figure 4.23: RMS roughness as a function of depth for smooth photoresist with and without photoresist redeposition. RMS of the sidewall is slightly larger for the photoresist with redeposition than for the case without redeposition.

How does the tapering of the photoresist, shown in Figure 4.24, affect the redeposition of sputtered photoresist materials and sidewall roughness of the etched feature? The simulation was performed using the initial feature shown in Figure 4.24, and the resulting feature profiles are plotted in Figure 4.25. Figure 4.25b shows that the foot of the ARC layer is not completely cleared, and these ARC and photoresist materials left on the surface affect the sidewall roughness in the subsequent polysilicon etching (Figure 4.25c). The schematic illustration of the effect of redeposition is shown in Figure 4.26. Since the tapered photoresist sidewall is bombarded by ions more than the vertical sidewall, more photoresist materials are expected to be sputtered off from the sidewall. The sputtered particles are assumed to leave the surface close to specular angle, and

178

therefore the particles are redeposited mostly at the foot of the photoresist/ARC layers during the ARC etching. As shown in Figure 4.25b, the clearing of the foot of ARC layer during ARC open step becomes difficult due to continuous redeposition of photoresist materials. If the etching of the substrate starts without clearing the foot of the ARC, the photoresist and ARC materials left on the surface cause micromasking of the polysilicon and decreases the etching of polysilicon masked by these materials. This enhances the sidewall roughness during the etching of polysilicon, as shown in Figure 4.25c.
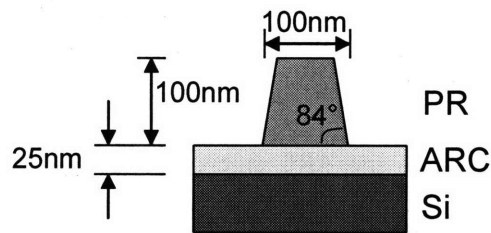
Figure 4.24: Dimension of the initial feature with tapered photoresist. The photoresist was assumed to have an angle of about 84°.

    (a)   (b)   (c)
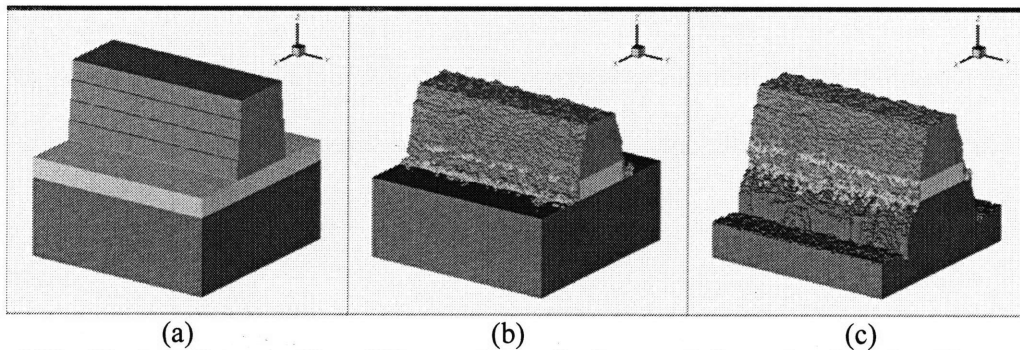
Figure 4.25: Simulated feature profile at different etch steps for the tapered photoresist with redeposition. (a) Before etching, (b) After ARC open, and (c) After etching 50 nm of polysilicon. After ARC open, the foot of the ARC sidewall is not completely cleared due to the heavy redeposition of photoresist materials sputtered from the tapered sidewall. If the polysilicon is etched before completely clearing the ARC layer, the sidewall roughness is enhanced due to the micromasking of polysilicon by the ARC particles left on the surface.
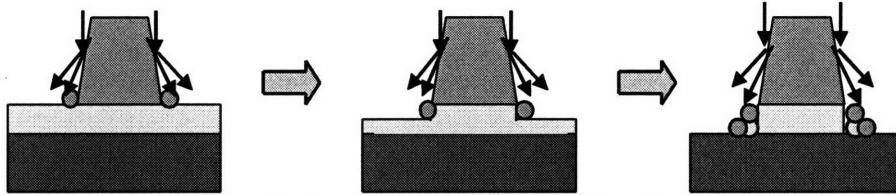
Figure 4.26: Schematic illustration of redeposition of photoresist. Since the sputtered materials leave the sidewall at close to the specular angle, particles are redeposited mostly at the foot of the photoresist/ARC sidewall.

The surface profiles at different locations along the sidewall are shown in Figure 4.27. The sidewall of ARC layer is roughened severely due to the redeposition of photoresist materials at the foot of ARC layer before the polysilicon etch step, and the roughness is transferred to the underlying polysilicon sidewall during the polysilicon etch. The transfer of roughness from the ARC sidewall to the polysilicon sidewall is also supported by the RMS roughness along the sidewall (Figure 4.28). RMS roughness is at photoresist/ARC interface and decreases with depth. The roughness may be transferred further down the sidewall if the etching time was increased and the polysilicon surface was etched further. Therefore, the tapering of photoresist enhances the redeposition of photoresist during the ARC open, which increases the sidewall roughness of the final etched feature.
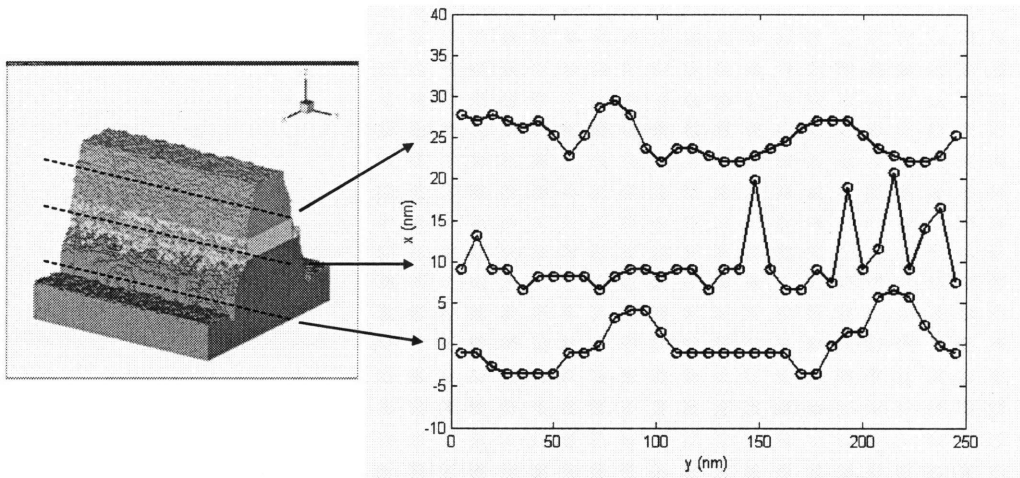
Figure 4.27: Surface profiles at different locations along the sidewall after etching 50 nm of polysilicon. (1) In the middle of the photoresist, (2) at the ARC layer and (3) at the bottom of the polysilicon sidewall. The sidewall of ARC is heavily roughened, with the amplitude of 10 nm.
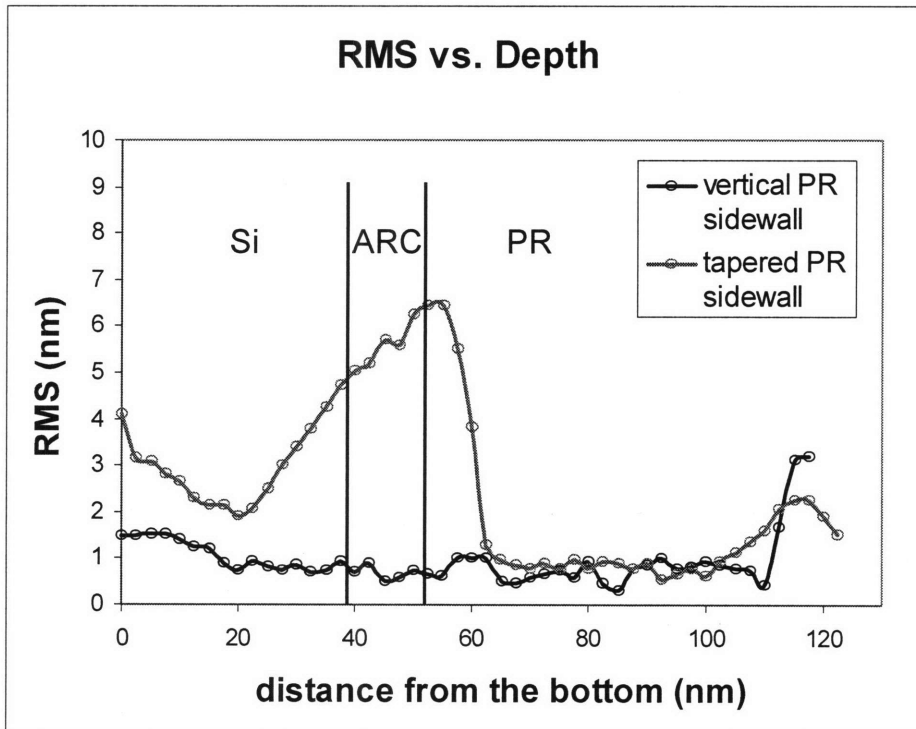
Figure 4.28: RMS roughness as a function of depth for vertical and tapered photoresist, with photoresist redeposition. For the tapered photoresist sidewall, the RMS is largest at photoresist/ARC interface and decreases with depth. The RMS is significantly larger than the case with vertical photoresist sidewall.

181

4.4. Conclusion

The roughening of the sidewall of patterned polysilicon in Cl_2 was explored using the 3-D Monte Carlo profile simulator. The simulation results showed that the sidewall roughness of the etched feature is minimal if the photoresist sidewall is perfectly smooth and vertical, where as the roughened or wiggled photoresist enhanced the sidewall roughness. The primary cause of sidewall roughness is the translation of roughness on the photoresist/ARC sidewall to the underlying polysilicon sidewall during the etching of polysilicon, but the roughening process is complicated by the fact that the roughness on the photoresist sidewall also changes throughout the etching process. The RMS roughness of the resulting feature is highest at the photoresist sidewall and decreases with depth. This trend is consistent with the experimental observations. The simulation also showed that the redeposition of sputtered photoresist particles will enhance the sidewall roughness. The effect of redeposition is greater for the tapered photoresist sidewall because more ions will strike the sidewall and sputter off more photoresist particles that will redeposit at the foot of the sidewall. The redeposited photoresist causes micromasking on the polysilicon surface which increases the sidewall roughening. Therefore, the simulation results confirmed that the sidewall roughness can be minimized by: (1) keeping the photoresist sidewall as smooth as possible, and (2) etch the ARC layer completely and clear out the foot of the photoresist/ARC sidewall before etching subsequent polysilicon layer. The simulator can be extended to study more detailed roughening by considering the inhomogeneity of photoresist film, larger feature size and longer etching time.

4.5. References

1. G. P. Patsis and E. Gogolides, Microelectronic Engineering **57-58**, 563 (2001).
2. G. W. Reynolds, J. W. Taylor, and C. J. Brooks, Journal of Vacuum Science and Technology B **17**, 3420 (1999)
3. N. Rau *et al.*, Journal of Vacuum Science and Technology B **16**, 3784 (1998).
4. D. L. Goldfarb *et al.*, Journal of Vacuum Science and Technology B **22**, 647 (2004).
5. S. A. Rasgon, Ph.D. Thesis, MIT (2005).
6. C. H. Lee, K. Jiang, and G. J. Davies, Materials Characterization **58**, 603 (2007).
7. J. Kim *et al.*, Journal of Vacuum Science and Technology B **21**, 790 (2003).

5. Conclusions and Future Work

5.1. Conclusions

A 3-D Monte Carlo simulator was developed to model the surface advancement in etching and deposition processes. The simulator employed a Monte Carlo algorithm to model mass transport and surface reaction kinetics and a cell-based representation for tracking surface compositions, allowing for the incorporation of both physical and chemical processes that occur in plasma etching. The local surface topography was simulated by fitting to a polynomial surface, from which the surface normal was computed. The surface advancement algorithm in the simulator considered both the movement of the surface in the direction of the surface normal and the smoothing of the surface caused by diffusion and surface relaxation. The good match between our simulation and the corresponding theoretical surface conformation in each case verified that our surface advancement algorithm has a sufficient basis for incorporating further complex factors in the plasma etching process.

The sputtering of a silicon surface with argon ions was simulated using a 3-D Monte Carlo simulator. The simulator incorporated the angular and local curvature dependences on etching yield. Simulating the sputtering of a silicon surface with various off-normal angles of the argon ion beam showed that there is a significant change in its morphology with different off-normal angles of incidence. When etched at normal ion incidence, the surface becomes roughened with no preferred orientation. When etched with an off-normal ion incidence below 50°, the surface develops ripples that are oriented perpendicular to the ion beam direction (i.e. wave vector is parallel to the ion beam). For off-normal angles of incidence between 50° and 60°, the surface remains smooth

independent of the etching time. The surface is roughened again for angles of incidence above 60°, forming patterns that are aligned with the ion beam direction. These trends match qualitatively with those observed in experimental measurements. The simulation results further showed that these transitions of surface morphology with increasing off-normal angles of ion incidence are related to the angular dependence of etching yield. The angle at which each transition occurs depends on the angle at which the peak yield occurs. This correlation is very useful because the roughening of a surface can be predicted approximately from the experimentally obtained angular dependence yield curve. The effects of other factors were also investigated using the simulator, and they include the angular distribution of scattered ions, the non-uniformity of the film density, the initial roughness of the surface, and the re-deposition of sputtered materials. The analysis of the effects of each factor on surface roughening has provided great insight into understanding the roughening mechanism in the sputtering process.

The roughening of the sidewall of patterned polysilicon in Cl_2 was explored using the 3-D Monte Carlo profile simulator. The simulation results showed that the sidewall roughness of the etched feature is minimal if the photoresist sidewall is perfectly smooth and vertical, where as the roughened or wiggled photoresist enhanced the sidewall roughness. The primary cause of sidewall roughness is the translation of roughness on the photoresist/ARC sidewall to the underlying polysilicon sidewall during the etching of polysilicon, but the roughening process is complicated by the fact that the roughness on the photoresist sidewall also changes throughout the etching process. The RMS roughness of the resulting feature is highest at the photoresist sidewall and decreases with depth. This trend is consistent with the experimental observations. The simulation also

showed that the redeposition of sputtered photoresist particles will enhance the sidewall roughness. The effect of redeposition is greater for the tapered photoresist sidewall because more ions will strike the sidewall and sputter off more photoresist particles that will redeposit at the foot of the sidewall. The redeposited photoresist causes micromasking on the polysilicon surface which increases the sidewall roughening. Therefore, the simulation results confirmed that the sidewall roughness can be minimized by: (1) keeping the photoresist sidewall as smooth as possible, and (2) etch the ARC layer completely and clear out the foot of the photoresist/ARC sidewall before etching subsequent polysilicon layer. The simulator can be extended to study more detailed roughening by considering the inhomogeneity of photoresist film, larger feature size and longer etching time.

5.2. Future work

The 3-D Monte Carlo simulator developed has a capability of extending to plasma etching systems using other chemistries and/or materials. By incorporating the appropriate surface kinetics model, the etching and roughening of dielectric materials such as SiO_2 films in fluorocarbon plasma may be simulated. In addition, the code may be further optimized to enhance the speed of the simulation for larger feature size. The simulator can also be used for exploring the profile and roughness evolutions in various 3-D features such as contact holes.

186

6. Appendices

6.1. Rotating a coordinate system

As mentioned in section 2.4.2, sometimes the coordinate system must be rotated in order to accurately fit the polynomial surface to the surface cells. This was done by determining a new z-axis by connecting the point of the center of mass and the center point of the cell under consideration, as illustrated in Figure 2.8. Then the two other axis (new x and y axes) are defined based on the new z-axis.

This is determined by COM
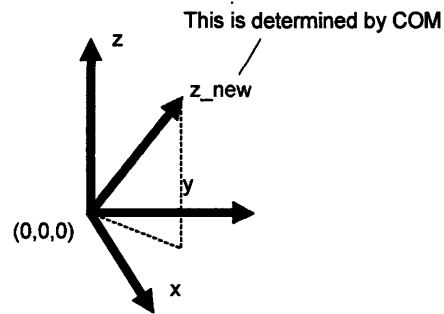
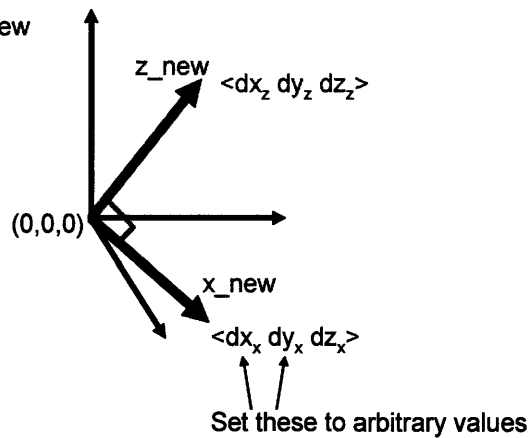x_new must be perpendicular to z_new

i.e.
$<dx_z\ dy_z\ dz_z> * <dx_x\ dy_x\ dz_x> = 0$

We know $<dx_z\ dy_z\ dz_z>$ and dx_x, dy_x

So...

$$dz_x = \frac{-(dx_z dx_x + dy_z dy_x)}{dz_z}$$

Set these to arbitrary values

y_new must be perpendicular to both
z_new and x_new

i.e.

$<dx_y \, dy_y \, dz_y> \; = \; <dx_z \, dy_z \, dz_z> \; \times \; <dx_x \, dy_x \, dz_x>$

$(0,0,0)$

z_new $<dx_z \, dy_z \, dz_z>$

y_new $<dx_y \, dy_y \, dz_y>$

x_new

$<dx_x \, dy_x \, dz_x>$
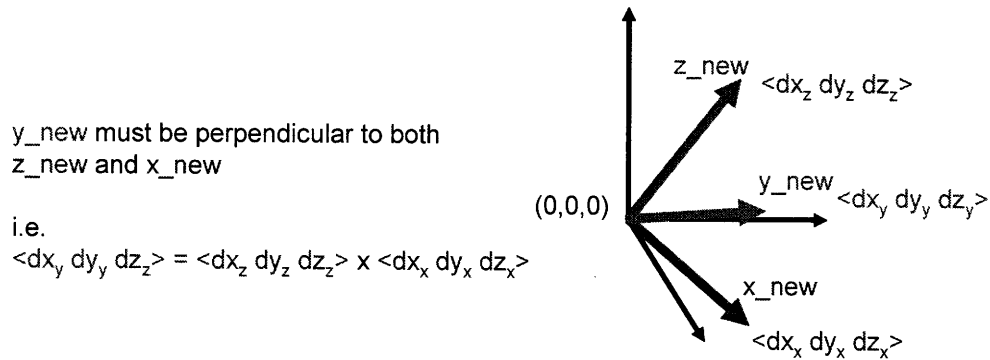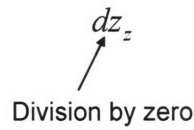
Each vector of axis is normalized, as shown below.

x-axis	y-axis	z-axis
$dx_x = \dfrac{dx_x}{\sqrt{dx_x{}^2 + dy_x{}^2 + dz_x{}^2}}$	$dx_y = \dfrac{dx_y}{\sqrt{dx_y{}^2 + dy_y{}^2 + dz_y{}^2}}$	$dx_z = \dfrac{dx_z}{\sqrt{dx_z{}^2 + dy_z{}^2 + dz_z{}^2}}$
$dy_x = \dfrac{dy_x}{\sqrt{dx_x{}^2 + dy_x{}^2 + dz_x{}^2}}$	$dy_y = \dfrac{dy_y}{\sqrt{dx_y{}^2 + dy_y{}^2 + dz_y{}^2}}$	$dy_z = \dfrac{dy_z}{\sqrt{dx_z{}^2 + dy_z{}^2 + dz_z{}^2}}$
$dz_x = \dfrac{dz_x}{\sqrt{dx_x{}^2 + dy_x{}^2 + dz_x{}^2}}$	$dz_y = \dfrac{dz_y}{\sqrt{dx_y{}^2 + dy_y{}^2 + dz_y{}^2}}$	$dz_z = \dfrac{dz_z}{\sqrt{dx_z{}^2 + dy_z{}^2 + dz_z{}^2}}$

If dz_z is zero, then the division by zero causes problem when determining the other two axes. To avoid this, dy_x instead of dz_x should be determined first, as shown below.
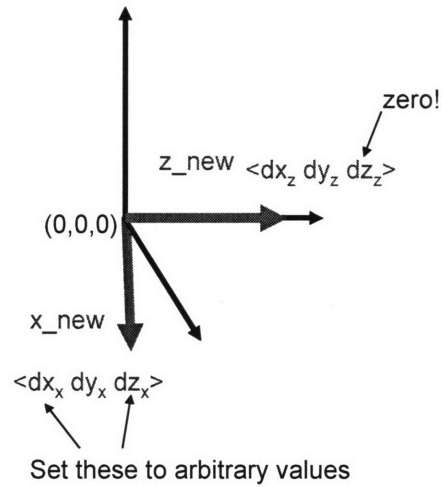
188

$$dz_x = \frac{-(dx_z dx_x + dy_z dy_x)}{dz_z}$$

Division by zero

So instead of setting dx_x and dy_x, set dx_x and dz_x to arbitrary values

$$dy_x = \frac{-(dx_z dx_x + dz_z dz_x)}{dy_z}$$

If dy_z is also zero, set dy_x and dz_x.

zero!

z_new $<dx_z\ dy_z\ dz_z>$

(0,0,0)

x_new

$<dx_x\ dy_x\ dz_x>$

Set these to arbitrary values

The position vector in the original coordinate can be transformed to the new coordinate system by determining the dot product of each vector of axis and the position vector in the original coordinate.
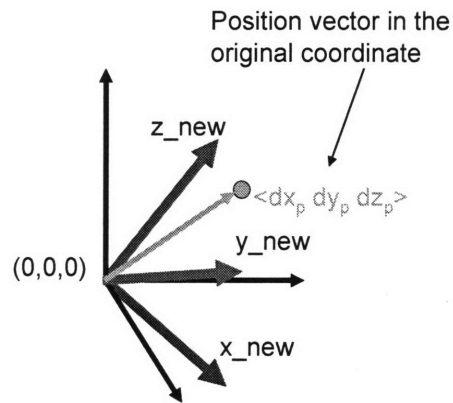
Project one vector on another

$x_p = <dx_x\ dy_x\ dz_x>*<dx_p\ dy_p\ dz_p>$

$y_p = <dx_y\ dy_y\ dz_y>*<dx_p\ dy_p\ dz_p>$

$z_p = <dx_z\ dy_z\ dz_z>*<dx_p\ dy_p\ dz_p>$

(x_p, y_p, z_p) = position in the new coordinate

Position vector in the original coordinate

z_new

$<dx_p\ dy_p\ dz_p>$

y_new

(0,0,0)

x_new

Each surface point in the local range (±3 cells) is transformed using the method described above, and the polynomial surface is fitted to these points in the transformed coordinate. This allows for an accurate representation of the surface for any surface conformation.

6.2. Determining the curvature along the ion trajectory

As described in section 3.4, only the curvature along the ion trajectory is important in the sputtering with off-normal ion incidence. However, the projection of ion trajectory is not necessarily aligned with x- or y-axis used in the polynomial fitting. Therefore, the coordinate must be rotated to define the projection of ion trajectory as either new x or y axis.

ion trajectory = $<t_x, t_y, t_z>$

$z = f(x, y)$
$= b_1 x^2 + b_2 y^2 + b_3 xy + b_4 x + b_5 y + b_6$

Rotate the axis about z-axis so that the trajectory is aligned with x-axis

$x = x' \cos\theta + y' \sin\theta$
$y = y' \cos\theta - x' \sin\theta$

$\cos\theta = \dfrac{t_x}{\sqrt{t_x^2 + t_y^2}}$

$\sin\theta = \dfrac{t_y}{\sqrt{t_x^2 + t_y^2}}$
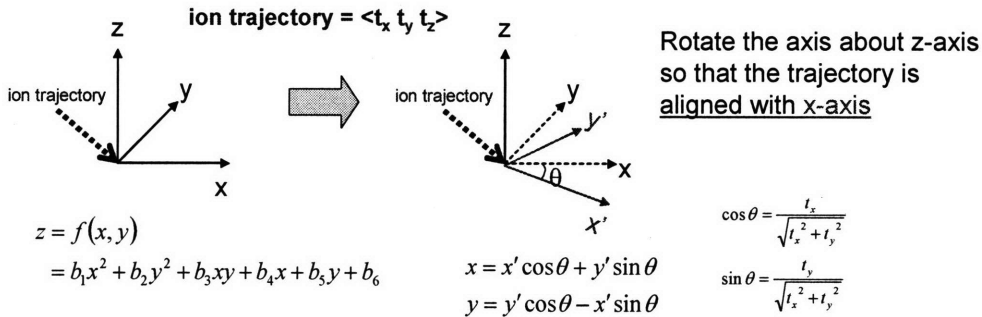
We want the equation with this form:
$z = f(x', y')$
$= \beta_1 x'^2 + \beta_2 y'^2 + \beta_3 x'y' + \beta_4 x' + \beta_5 y' + \beta_6$

$z = f(x, y)$
$= b_1 x^2 + b_2 y^2 + b_3 xy + b_4 x + b_5 y + b_6$

substitute in
$x = x' \cos\theta + y' \sin\theta$
$y = y' \cos\theta - x' \sin\theta$

$z = f(x, y)$
$= b_1 x^2 + b_2 y^2 + b_3 xy + b_4 x + b_5 y + b_6$
$= b_1 (x' \cos\theta + y' \sin\theta)^2 + b_2 (y' \cos\theta - x' \sin\theta)^2 + b_3 (x' \cos\theta + y' \sin\theta)(y' \cos\theta - x' \sin\theta) + b_4 (x' \cos\theta + y' \sin\theta) + b_5 (y' \cos\theta - x' \sin\theta) + b_6$
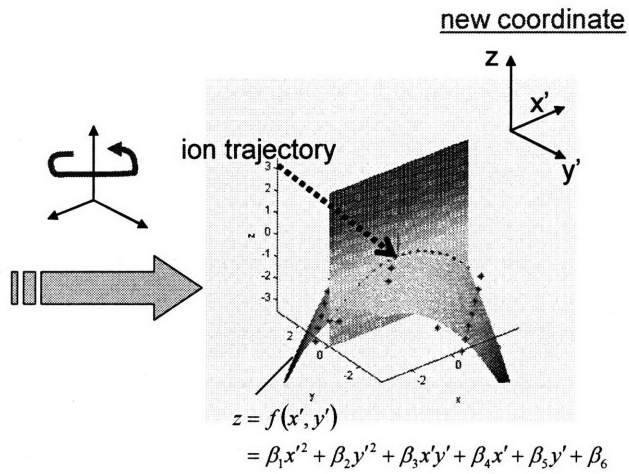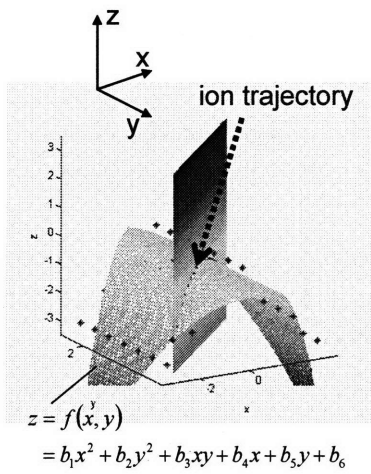
After doing some algebra, the new coefficients can be defined as following:

$$\beta_1 = b_1 \cos^2\theta + b_2 \sin^2\theta - b_3 \cos\theta \sin\theta$$

$$\beta_2 = b_1 \sin^2\theta + b_2 \cos^2\theta + b_3 \sin\theta \cos\theta$$

$$\beta_3 = 2(b_1 - b_2)\cos\theta \sin\theta + b_3(\cos^2\theta - \sin^2\theta)$$

$$\beta_4 = b_4 \cos\theta - b_5 \sin\theta$$

$$\beta_5 = b_4 \sin\theta + b_5 \cos\theta$$

$$\beta_6 = b_6$$

where

$$\cos\theta = \frac{t_x}{\sqrt{t_x^2 + t_y^2}}$$

$$\sin\theta = \frac{t_y}{\sqrt{t_x^2 + t_y^2}}$$

After substituting $\cos\theta$ and $\sin\theta$ with the expression shown above, the new coefficients can be defined as a function of ion trajectory vector $<t_x\ t_y\ t_z>$.

$$\beta_1 = \frac{b_1 t_x^2 + b_2 t_y^2 - b_3 t_x t_y}{t_x^2 + t_y^2}$$

$$\beta_2 = \frac{b_1 t_y^2 + b_2 t_x^2 + b_3 t_x t_y}{t_x^2 + t_y^2}$$

$$\beta_3 = \frac{2(b_1 - b_2)t_x t_y + b_3\left(t_x^2 - t_y^2\right)}{t_x^2 + t_y^2}$$

$$\beta_4 = \frac{b_4 t_x - b_5 t_y}{\sqrt{t_x^2 + t_y^2}}$$

$$\beta_5 = \frac{b_4 t_y + b_5 t_x}{\sqrt{t_x^2 + t_y^2}}$$

$$\beta_5 = b_6$$

β_1 and β_2 are the curvature in x and y directions, respectively. One example is shown below.

$$z = f(x, y)$$
$$= b_1 x^2 + b_2 y^2 + b_3 xy + b_4 x + b_5 y + b_6$$

$$z = f(x', y')$$
$$= \beta_1 x'^2 + \beta_2 y'^2 + \beta_3 x'y' + \beta_4 x' + \beta_5 y' + \beta_6$$

- Now, the ion trajectory is parallel to the new x-axis, towards +x' direction
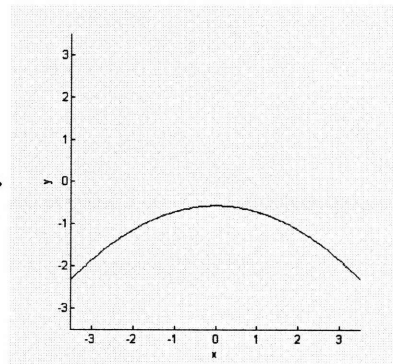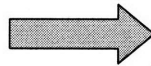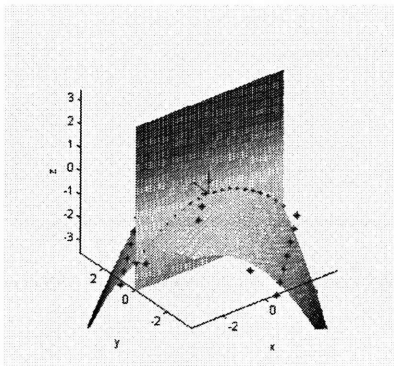
At y' = 0,

$$z = f(x', y')$$
$$= \beta_1 x'^2 + \beta_2 y'^2 + \beta_3 x'y' + \beta_4 x' + \beta_5 y' + \beta_6$$
$$= \beta_1 x'^2 + \beta_4 x' + \beta_6$$

192